SANDIA REPORT
SAND2018-5726
Unlimited Release
Printed May 2018

Particle Mass Flow Control for High-Temperature Concentrating Solar Receivers

Clifford K. Ho, Gregory Peacock, Brantley Mills, Joshua M. Christian, Kevin Albrecht,
Julius E. Yellowhair, and Daniel Ray

Prepared by
Sandia National Laboratories
Albuquerque, New Mexico 87185 and Livermore, California 94550

Sandia National Laboratories is a multimission laboratory managed and operated
by National Technology and Engineering Solutions of Sandia, LLC, a wholly owned
subsidiary of Honeywell International, Inc., for the U.S. Department of Energy's
National Nuclear Security Administration under contract DE-NA0003525.

Sandia National Laboratories

Issued by Sandia National Laboratories, operated for the United States Department of Energy by National Technology and Engineering Solutions of Sandia, LLC.

Available to DOE and DOE contractors from
U.S. Department of Energy
Office of Scientific and Technical Information
P.O. Box 62
Oak Ridge, TN 37831

Telephone: (865) 576-8401
Facsimile: (865) 576-5728
E-Mail: reports@osti.gov
Online ordering: http://www.osti.gov/scitech

Available to the public from
U.S. Department of Commerce
National Technical Information Service
5301 Shawnee Rd
Alexandria, VA 22312

Telephone: (800) 553-6847
Facsimile: (703) 605-6900
E-Mail: orders@ntis.gov
Online order: http://www.ntis.gov/search

SAND2018-5726
Printed May 2018
Unlimited Release

Particle Mass Flow Control for High-Temperature Concentrating Solar Receivers

Clifford K. Ho,[1] Gregory Peacock,[1] Brantley Mills,[2] Joshua M. Christian,[1] Kevin Albrecht,[1] and Daniel Ray[1]
[1]Org. 08823 Concentrating Solar Technologies
[2]Org. 1514 Thermal Sciences & Engineering
Sandia National Laboratories
P. O. Box 5800
Albuquerque, New Mexico 87185-1127

Abstract

This report summarizes the results of a two-year project funded by the U.S. Department of Energy's Solar Energy Technologies Office (SuNLaMP 1506) to evaluate the performance of high-temperature (>700 °C) particle receivers for concentrating solar power (see Appendix A for project information). In the first year, novel particle release patterns were designed and tested to increase the effective solar absorptance of the particle curtain. Modeling results showed that increasing the magnitude and frequency of different wave-like patterns increased the effective absorptance and thermal efficiency by several percentage points, depending on the mass flow rate. Tests showed that triangular-wave, square-wave, and parallel-curtain particle release patterns could be implemented and maintained at flow rates of ~10 kg/s/m. The second year of the project focused on the development and testing of particle mass-flow control and measurement methods. An automated slide gate controlled by the outlet temperature of the particles was designed and tested. Testing demonstrated that the resolution accuracy of the slide-gate positioning was less than ~1 mm, and the speed of the slide gate enabled rapid adjustments to accommodate changes in the irradiance to maintain a desired outlet temperature range. Different in-situ particle mass-flow measurement techniques were investigated, and two were tested. The in-situ microwave sensor was found to be unreliable and sensitive to variations in particle flow patterns. However, the in-situ weigh hopper using load cells was found to provide reliable and repeatable measurements of real-time in-situ particle mass flow. On-sun tests were performed to determine the thermal efficiency of the receiver as a function of mass flow rate, particle temperature, and irradiance. Models of the tests were also developed and compared to the tests.

ACKNOWLEDGMENTS

This work was funded by the U.S. Department of Energy's Solar Energy Technologies Office (SuNLaMP project 1506). Sandia National Laboratories is a multimission laboratory managed and operated by National Technology and Engineering Solutions of Sandia, LLC., a wholly owned subsidiary of Honeywell International, Inc., for the U.S. Department of Energy's National Nuclear Security Administration under contract DE-NA0003525.

TABLE OF CONTENTS

FIGURES

TABLES

1. INTRODUCTION

1.1. Background and Problem Statement

Falling particle receivers are being studied as a means to enable higher operating temperatures (above 700 C), direct thermal storage, and higher receiver efficiencies for concentrating solar power technologies [1]. Unlike conventional receivers that employ fluid flowing through tubular receivers, falling particle receivers use solid particles that are heated directly as they fall through a beam of concentrated sunlight for direct heat absorption. Once heated, the particles may be stored in an insulated tank and used to heat a secondary working fluid for the power cycle.

Current falling particle receiver designs employ a linear particle release, resulting in the particles falling along a planar curtain through the solar flux (Figure 1, Left). Incident light that is reflected off of the planar particle curtain back toward the aperture is lost. The current work describes alternative zig-zag particle release configurations to take advantage of volumetric heating and potential light-trapping behavior (Figure 1, Right) [2]. The zig-zag release patterns allows light to be trapped between particle curtain sections, increasing the overall effective solar absorptance of the particles. Thermal losses from the hottest particles furthest from aperture are also reduced due to reduced radiative view factors and blocking from particles nearest the aperture, which reduces both radiative and convective heat losses. A multi-drop configuration with parallel particle curtains can also be employed to increase the volumetric effect and heating of the particles [2].

Figure 1. Left: particles dropped through a straight slot creating a planar "curtain" of falling particles. Right: Zig-zag particle release pattern for increased light trapping.

In addition, previous studies have employed slotted discharge plates with a prescribed aperture to control the mass flow of particles entering the receiver from a top hopper. However, on-sun tests have shown that thermal expansion of the plates can cause changes to the aperture and plastic deformation to the plate, causing uncertain mass flow rates and overheating [3]. This work investigates the use of a linear slide gate that can automatically control the aperture setting through which particles flow based on a desired particle outlet temperature. If the particle outlet temperature is too low, the slide gate will close the aperture to reduce the mass flow rate and increase the particle temperatures. If the particle outlet temperature is too high, the slide gate will open to increase the mass flow rate and reduce the particle temperatures. In addition, reliable methods to measure the in-situ particle mass flow are required to accurately determine the thermal efficiency of the receiver.

1.2. Objectives

The objectives of this work were as follows:

- Design and evaluate alternative particle release patterns to increase the light trapping and thermal efficiency of the receiver
- Design and test a particle mass-flow control system that accommodates changes in irradiance to maintain a desired particle outlet temperature
- Evaluate particle mass-flow measurement systems that can accurately and reliably record the particle mass flow rate during an on-sun test
- Determine the particle temperature rise and thermal efficiency during on-sun tests of the prototype particle receiver and compare to modeled results

2. NOVEL PARTICLE RELEASE PATTERNS

Previous studies of free-falling particle receivers have employed a straight, planar particle curtain [3-8]. Particles were released from a straight slot with a machined aperture width to provide a desired mass flow rate. In this work, alternative particle release patterns were investigated both numerically and experimentally to determine the impact on effective solar absorptance and thermal efficiency of the receiver. Several papers have been published that detail these analyses [9-11].

2.1. Modeling

In Phase 1 (Year 1), alternative particle release patterns were modeled to determine the potential increase in thermal efficiency over a baseline planar release pattern (Figure 2). Parametric studies were conducted to determine important features and processes of the falling particle curtains that impacted the thermal efficiency. The overall strategy followed in this parametric study has been defined in a flow chart shown in Figure 3. This chart outlines all the avenues that were explored in this parametric study and provides a brief explanation for each study.

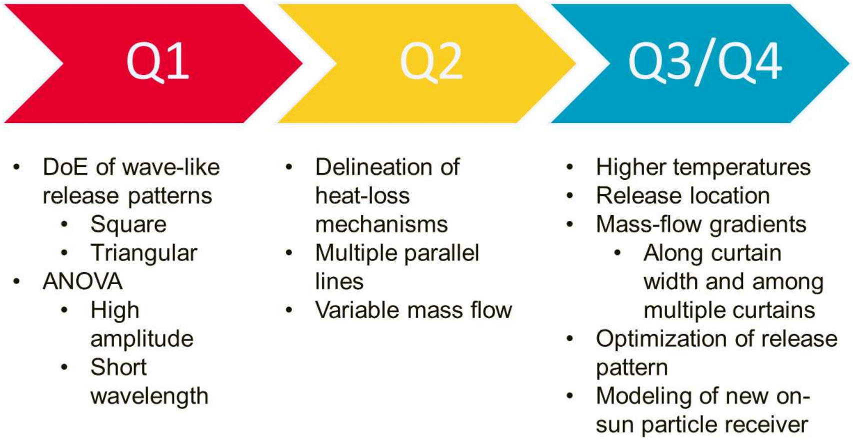

Figure 2. Timeline of modeling activities during Phase 1 (Year 1).

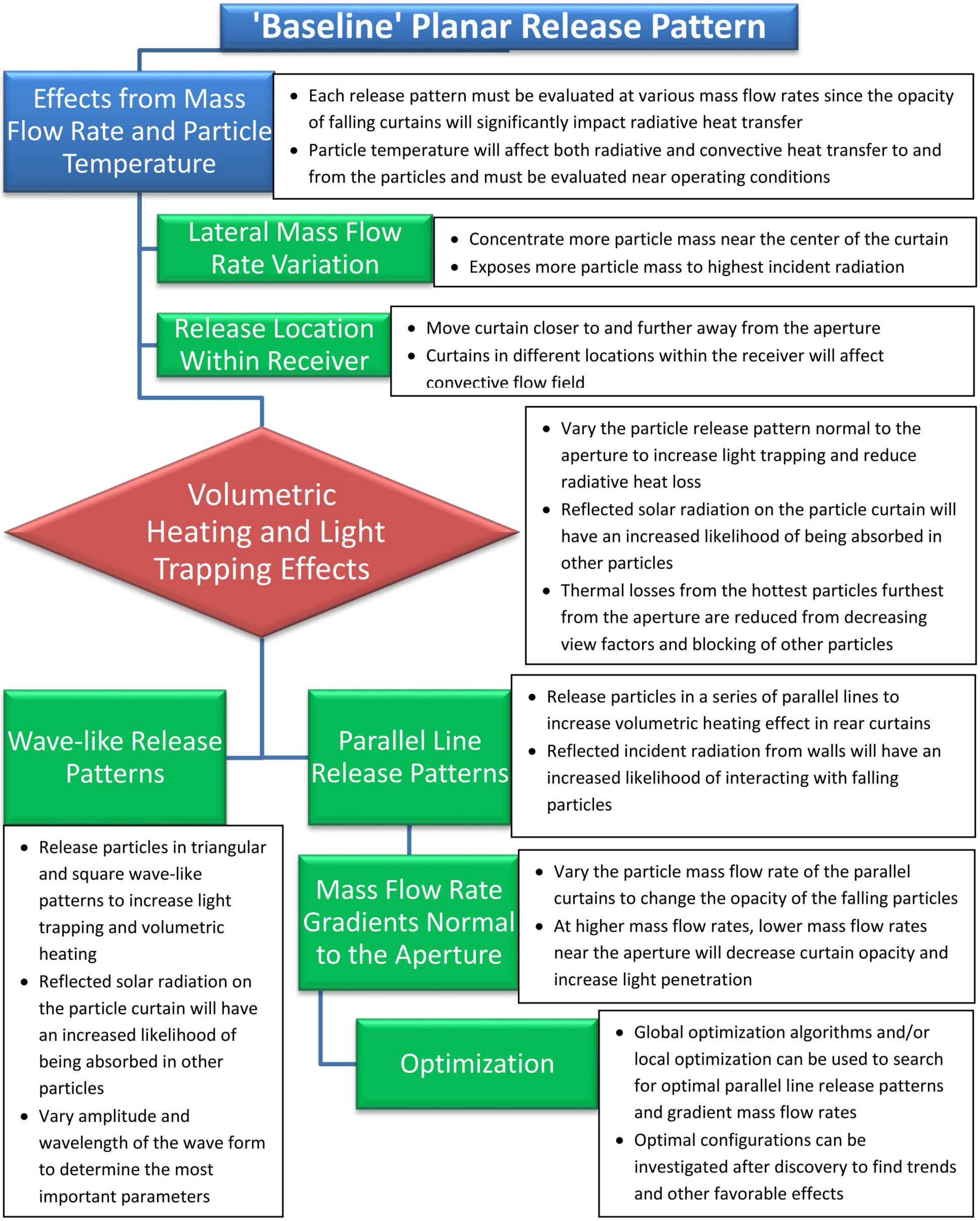

'Baseline' Planar Release Pattern

Effects from Mass Flow Rate and Particle Temperature

- Each release pattern must be evaluated at various mass flow rates since the opacity of falling curtains will significantly impact radiative heat transfer
- Particle temperature will affect both radiative and convective heat transfer to and from the particles and must be evaluated near operating conditions

Lateral Mass Flow Rate Variation

- Concentrate more particle mass near the center of the curtain
- Exposes more particle mass to highest incident radiation

Release Location Within Receiver

- Move curtain closer to and further away from the aperture
- Curtains in different locations within the receiver will affect convective flow field

Volumetric Heating and Light Trapping Effects

- Vary the particle release pattern normal to the aperture to increase light trapping and reduce radiative heat loss
- Reflected solar radiation on the particle curtain will have an increased likelihood of being absorbed in other particles
- Thermal losses from the hottest particles furthest from the aperture are reduced from decreasing view factors and blocking of other particles

Wave-like Release Patterns

- Release particles in triangular and square wave-like patterns to increase light trapping and volumetric heating
- Reflected solar radiation on the particle curtain will have an increased likelihood of being absorbed in other particles
- Vary amplitude and wavelength of the wave form to determine the most important parameters

Parallel Line Release Patterns

- Release particles in a series of parallel lines to increase volumetric heating effect in rear curtains
- Reflected incident radiation from walls will have an increased likelihood of interacting with falling particles

Mass Flow Rate Gradients Normal to the Aperture

- Vary the particle mass flow rate of the parallel curtains to change the opacity of the falling particles
- At higher mass flow rates, lower mass flow rates near the aperture will decrease curtain opacity and increase light penetration

Optimization

- Global optimization algorithms and/or local optimization can be used to search for optimal parallel line release patterns and gradient mass flow rates
- Optimal configurations can be investigated after discovery to find trends and other favorable effects

Figure 3. Flow chart of the parametric study strategy used in this study

In Q1, wave-like particle release patterns were investigated using a systematic design of experiments to elucidate important features of each release pattern (i.e., amplitude, wavelength, and waveform). In Q2, additional release patterns were investigated, including multiple parallel lines and variable mass flow rates. In Q3 and Q4, we investigated the effects of particle release location, spatial mass flow gradients, the use of an optimization strategy to reveal favorable particle release patterns that may not have been explored otherwise, and increased particle inlet temperatures to achieve particle outlet temperatures of >720 °C. Finally, a new model of the existing falling particle receiver at the National Solar Thermal Test Facility (NSTTF) at Sandia National Laboratories was also developed to evaluate the most promising particle release patterns and more accurately characterize convective losses within the receiver to be tested.

2.1.1. Particle Receiver Model

Alternative particle release patterns were modeled and compared to a baseline planar particle release pattern using an existing, validated model [12] of a solid particle receiver previously tested at the NSTTF at Sandia using ANSYS Fluent. A drawing of the solid particle receiver and the subsequent Fluent model used in the parametric study is shown in Figure 4.

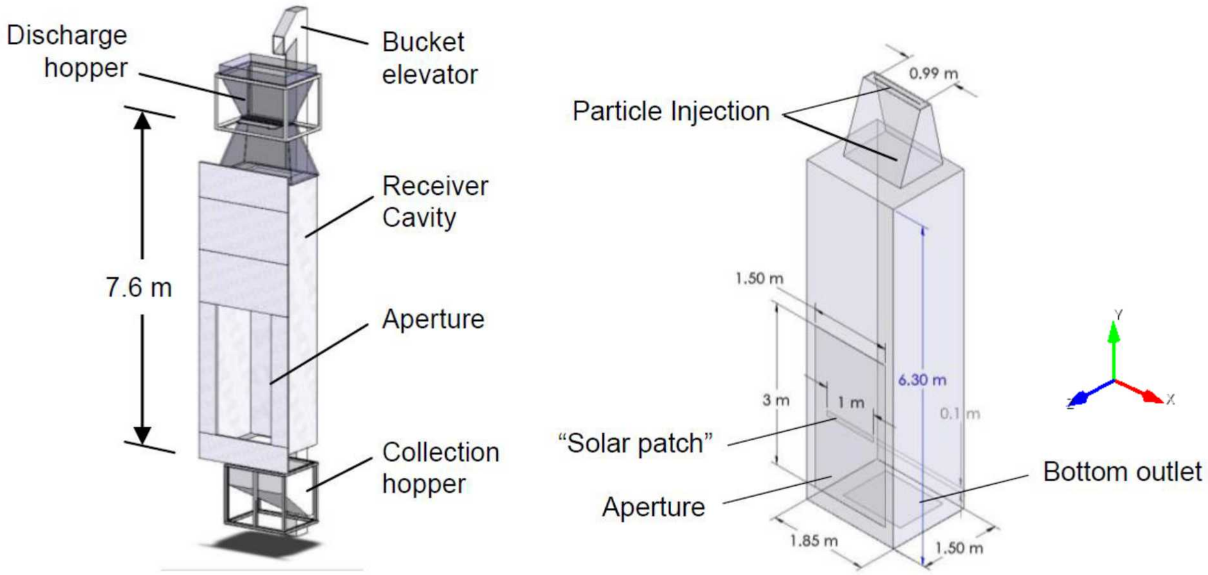

Figure 4. Drawing of the solid particle receiver (left) tested on-sun at low temperatures (~250 °C) and the Fluent model used in the parametric study (right) [12].

The Fluent model was comprised of 169,200 hexahedral cells, which was found to be sufficient to yield convergence in the solutions. An air volume was modeled inside the receiver cavity. Cool air entered the domain through the aperture and was circulated through the cavity from interaction with the falling particles or from buoyancy-driven flow resulting from temperature gradients within the air. Turbulent flow was modeled using the realizable k-ε turbulence model and Fluent's standard wall functions. Air left the domain through recirculation out of the aperture or through the bottom outlet, both defined as fixed pressure boundary conditions. The receiver walls were comprised entirely of an alumina silica ceramic fiberboard.

Particles were released from ~300 injection sites defined near the top of the receiver cavity and tracked through the domain before exiting out the bottom outlet. Each particle's motion was coupled with the air through drag forces acting on the particles. Particle to particle interaction was not included under the assumption that the volume fraction of particles in the air volume was sufficiently small. This assumption was valid for volume fractions less than 10%. Previous tests on falling particle receivers have indicated that the volume fraction of particles was less than several percent [4]. Radiative and convective heat transfer to and from the particles was also included in the model. In the previous work on this parametric study, particle inlet temperature has been set to a constant 23 °C (300 K). However, to be more applicable to actual conditions within a particle receiver, particle inlet temperatures were set to 600 °C (873 K) in all further analysis.

A non-grey discrete-ordinates radiation model was used to simulate radiation heat transfer inside the domain. Both angular dimensions were discretized into seven divisions. The wavelength spectrum was divided into two spectral bands: 0.1 – 4.5 μm and 4.5 – 100 μm to represent the spectral properties of the receiver walls. All incident solar radiation was defined to enter the domain entirely in the smaller wavelength band (0.1 – 4.5 μm). The second, higher wavelength band was used to define the emission of thermal radiation from the walls and particles. Incident solar radiation to the domain was applied on a small solar patch within the aperture. For the previous work on this parametric study, a fixed an incident power of 1.52×10^6 W was used. However, to be more relevant to conditions within a particle receiver, the incident power was varied with the particle mass flow rate such that the average particle outlet temperature reached ~720 °C (993 K). An incident beam shape was used with a 30 degree angular range vertically and a 60 degree angular range horizontally that was consistent with the validated model [12].

Conduction through the walls of the receiver was also included in the model in addition to convection on the exterior walls to the surrounding environment. A heat transfer coefficient of 5 W/m^2K was applied on the exterior of the domain with a reference temperature of 300 K. Air entering the domain though the aperture also entered at 300 K.

2.1.2. Modeling Results

In Q1, the model described in the previous section was used to demonstrate that various "wave-like" volumetric particle release patterns increased the thermal efficiency of the receiver over a planar release by up to ~7% (Figure 5). An assessment of the heat-loss mechanisms revealed that the wave-like patterns increase light trapping and reduced solar reflective losses. Convective losses were increased due to the increased exposed surface area of the wave-like particle curtains relative to the planar curtain, but the reduction in radiative losses outweighed the convective losses.

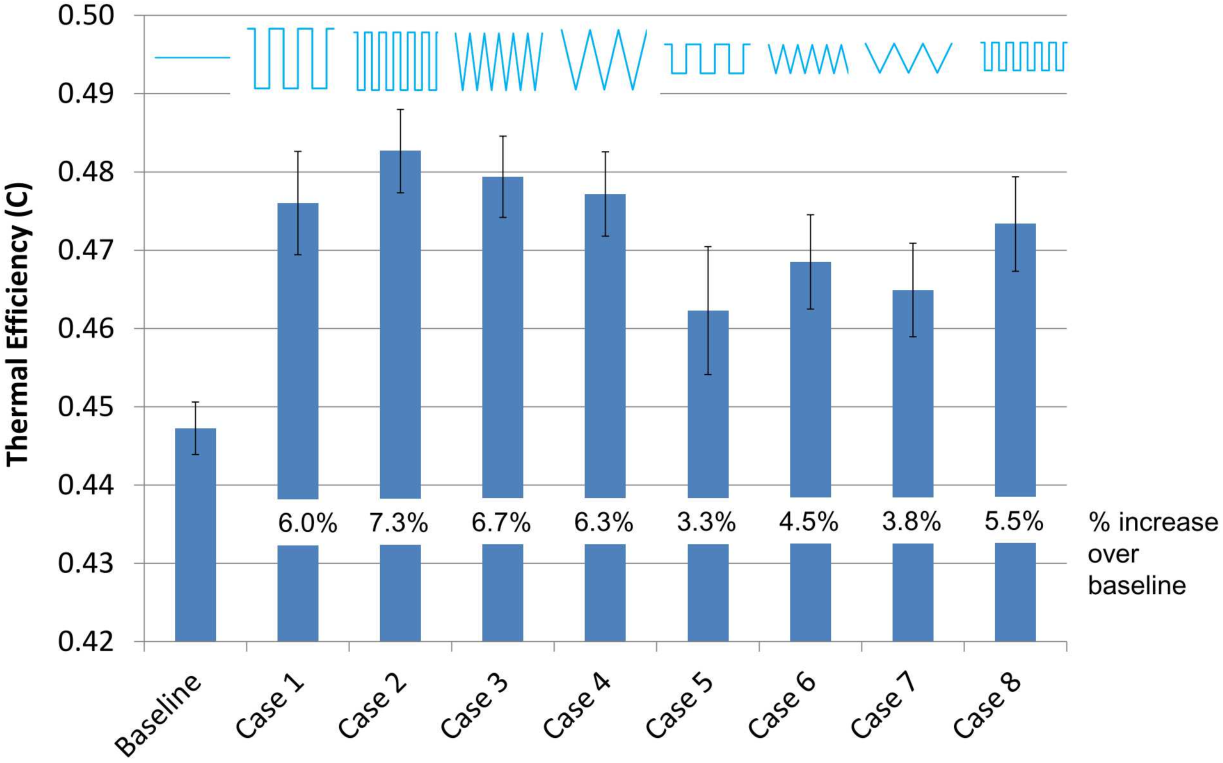

Figure 5. Simulated thermal efficiency of wave-like particle release patterns relative to baseline case that was tested on-sun at temperatures up to ~250 °C.

In Q2, the analysis was extended to include: five additional volumetric release patterns consisting of parallel straight-line particle release patterns, the effect of mass flow rate on the thermal efficiency, and more details into the radiative and convective losses from the model. Ultimately, all volumetric release patterns showed higher thermal efficiencies when compared to the baseline planar particle release pattern with the exception of a few patterns at the highest mass flow rates. Higher thermal efficiencies were associated with lower radiative losses in the volumetric release patterns consistent with improved performance as a result of increased light-trapping effects. The mass flow rate was also shown to be the most significant factor in the thermal efficiency irrespective of the release pattern.

In Q3, we extended the parametric study of different novel particle release patterns for a high-temperature falling particle receiver that has been performed in Q2 and Q1. Alternative particle release patterns that differed from a conventional planar curtain of falling particles offered the possibility of more thermally efficient receivers from reduced convective losses or light-trapping in volumetric particle releases. The remainder of this section focuses on the analyses performed in Q3 and Q4.

In addition to the thirteen volumetric release patterns explored in Q2 summarized in Table 1, an additional eight patterns were explored in this study and are summarized separately in Table 2. All volumetric release patterns were evaluated against a conventional planar release (labeled as ‘Baseline’ in Table 1). Particles from each pattern fell from a 1 m by 0.6 m area near the top of the receiver. The patterns are all 1 m wide, but the depth of each pattern varied and is provided in the table. Approximately 300 injection sites were evenly distributed over the desired pattern, although in Case 16 the number of injection sites was increased to 2100 as a check to confirm 300 injection sites were sufficient. Previous analysis of this model has demonstrated that the number of injection sites does not significantly affect the solution as long as the number of injection sites exceeded 100 [12].

In Table 2, Cases 14 and 15 investigated the effect of release location within the receiver by moving the Baseline curtain to the rear and front of the 0.6 m deep release area, respectively. Case 17 was a parallel-line optimized release pattern created from lessons learned in the optimization routine where the numbers in the illustration indicated the percentage of total mass flow rate in each line. Case 18-21 were cases that varied the mass flow rate laterally across the Baseline curtain. The top numbers in the illustration indicated the percentage of mass flow rate in that segment of the curtain, and the bottom numbers indicated the length of that respective segment.

In addition to exploring different types of particle release patterns defined in Table 1 and Table 2, each configuration was also simulated at mass flow rates of 3.0, 5.0, 7.0, 10.0, and 12.5 kg/s bounding the capabilities of existing solid particle receivers currently tested at the NSTTF. Each release pattern explored here was also 1 m in length (linear width), so the mass flow rate can also be expressed per unit length (*i.e.* 12.5 kg/s or 12.5 kg/m·s). By varying the mass flow rate, the thermal performance of each volumetric release pattern relative to the baseline configuration was evaluated as the mass flow rate changed. As shown in Q2, increasing the mass flow rate was the most significant factor in the thermal efficiency regardless of the release pattern. Radiative and convective losses from the model were also computed and summarized for each case. Note that in addition to the cases presented in Table 1, Case 10, consisting of five parallel lines, was also explored by varying the mass flow rate in each release line normal to the aperture. Four distinct gradients were explored at each mass flow rate. Each gradient is defined here as a constant value G equal to the mass flow rate of the rear curtain relative to the front curtain with a linear transition across the interior curtains. That is, $G = 3$ indicated the rear curtain has a mass flow rate three times that of the front curtain (*i.e.* the particle mass flow rate and curtain opacity increased moving away from the aperture).

Table 1. Original fourteen particle-release patterns explored in Q2

Case	Depth (m)	Scaled Illustration
Baseline	N/A	
Case 1	0.4	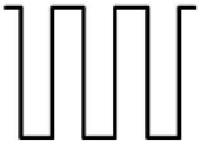
Case 2	0.4	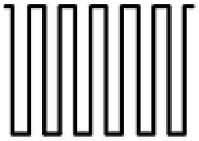
Case 3	0.4	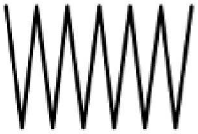
Case 4	0.4	
Case 5	0.2	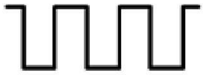
Case 6	0.2	
Case 7	0.2	
Case 8	0.2	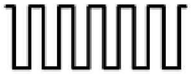
Case 9	0.2	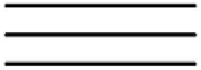
Case 10	0.4	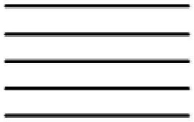
Case 11	0.6	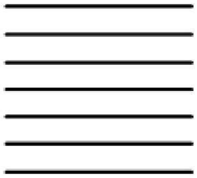
Case 12	0.4	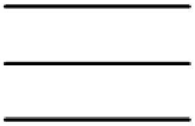
Case 13	0.6	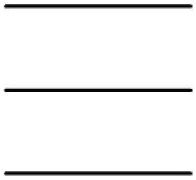

Table 2. Eight additional particle-release patterns explored in Q3 and Q4. Red arrow denotes direction of incident solar radiation. Top numbers in Cases 18 – 21 indicate percentage of mass flow in a segment, while bottom numbers indicate length of segment.

Case	Depth (m)	Scaled Illustration	Case	Depth (m)	Scaled Illustration
Case 14	N/A	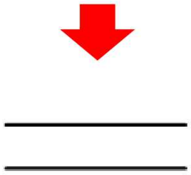	Case 18	N/A	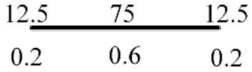
Case 15	N/A	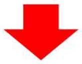	Case 19	N/A	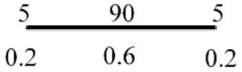
Case 16	0.6	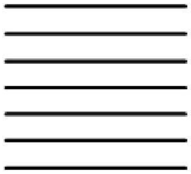	Case 20	N/A	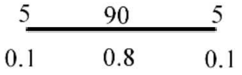
Case 17	0.3	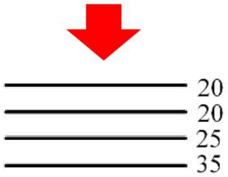	Case 21	N/A	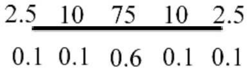

2.1.3. Parametric Study Results

The parametric study performed up to this point had evaluated release patterns with particle inlet temperatures of 23 °C (to match the validated model and previous on-sun tests). However, to more appropriately evaluate particle release patterns at high-temperature conditions, all further analysis was performed using particle inlet temperatures of 600 °C. This ensured that thermal properties and heat transfer could be evaluated more accurately at elevated temperatures. Note that the use of higher particle inlet temperatures increased the convective losses from the particles, and convective losses have shown in the previous results reported in Q2 to be higher for volumetric release patterns. That is, convective losses tended to counteract gains in thermal efficiency created by light trapping and volumetric heating.

Convective losses from the model depend strongly on the convective flow within the receiver. A previous numerical study of larger 100 MW_{th} particle receivers using similar models and physics to those applied in this work have demonstrated that convective losses can be significantly reduced with the appropriate receiver geometry [13]. One explanation for the significant reduction in convective losses observed in some of the models was the trapping and recirculation of hot air within the receiver. In such geometries, cold air recirculating into the receiver cavity was heavily reduced. The geometry used in the present parametric study was not optimized to reduce convective losses from the receiver. In fact, air entrained by falling particles was simulated to immediately exit out of the bottom of the receiver thereby increasing the flow of cold air entering through the aperture. Typically, in an actual particle receiver, air will be obstructed at some point below the collection hopper and prevented from leaving the domain. Therefore, in this present geometry convective losses from the model were found to be greatly increased. Despite this, using this model for a parametric study of volumetric particle release patterns provided a very conservative estimate of the gains in thermal efficiency created by a volumetric pattern release by overestimating convective losses in the model. This provided additional confidence that patterns producing increases in thermal efficiency over a traditional baseline release would continue to do so in other geometries. It also helped narrow down the most promising candidates of volumetric release patterns.

In order to more accurately evaluate the thermal efficiency numerically of a particular volumetric release pattern, the pattern must be evaluated in the receiver geometry to be used. Therefore, a separate model of the existing particle receiver installed at the NSTTF was developed to evaluate the volumetric release patterns in an actual test environment. Ultimately, the release patterns that have demonstrated the best performance with the current model will be run on this new model of the existing particle receiver to find the most efficient design. A description of this model with preliminary results is provided later in this report.

As defined in the previous reports, the thermal efficiency η_{th} for each release pattern is calculated as follows:

$$\eta_{th} = \frac{Q_{abs}}{Q_{in}} = \frac{\dot{m}\left(h_{out} - h_{in}\right)}{Q_{in}} = \frac{\int_{T_{in}}^{T_{out}} c_P(T)dT}{Q_{in}} \tag{1}$$

where Q_{abs} is the absorbed thermal power in the particles, Q_{in} is the incident thermal radiative power, $\dot{m}$ is the total particle mass flow rate (kg/s), h is the enthalpy of the particles (J/kg), and $c_P(T)$ is the specific heat of the particles (J/kg·K) as a function of temperature T defined as:

$$c_P(T)=365 \cdot T^{0.18} \tag{2}$$

where T is the mean particle temperature (ºC). The thermal efficiency was effectively the fraction of incident radiative power that was removed from the receiver by the particles.

The thermal efficiency for each of the wave-like volumetric release patterns reported in Q1 and Q2 is plotted in Figure 6 with its respective radiative losses for wavelengths < 4.5 μm for 10.0 kg/m·s. The results presented here plot the thermal efficiency and radiative losses for particle inlet temperatures at 600 °C and outlet temperatures approximately equal to 720 °C. Recall that the incident flux was varied to give the appropriate outlet temperature and temperature distribution in the particle curtain. Radiative losses at this wavelength would be suggestive of incident solar radiation (all incident solar radiation in this problem was modeled in the spectral band with wavelengths < 4.5 μm) that was reflected from the domain and not absorbed in the walls or particles. Therefore, for volumetric release patterns with lower radiative losses in this spectral band would be indicative of increased light-trapping effects. However, as opposed to previous results at lower particle inlet temperatures, lower thermal efficiencies were observed in all wave-like patterns at all mass flow rates compared to the Baseline release pattern. This was in spite of lower radiative losses indicating increased light-trapping effects. Note that larger amplitudes and shorter wave-lengths (Case 2 and Case 3) still showed the smallest radiative losses. An explanation for the lower reported thermal efficiencies despite decreased radiative losses was found by computing the total losses from the model by each mechanism.

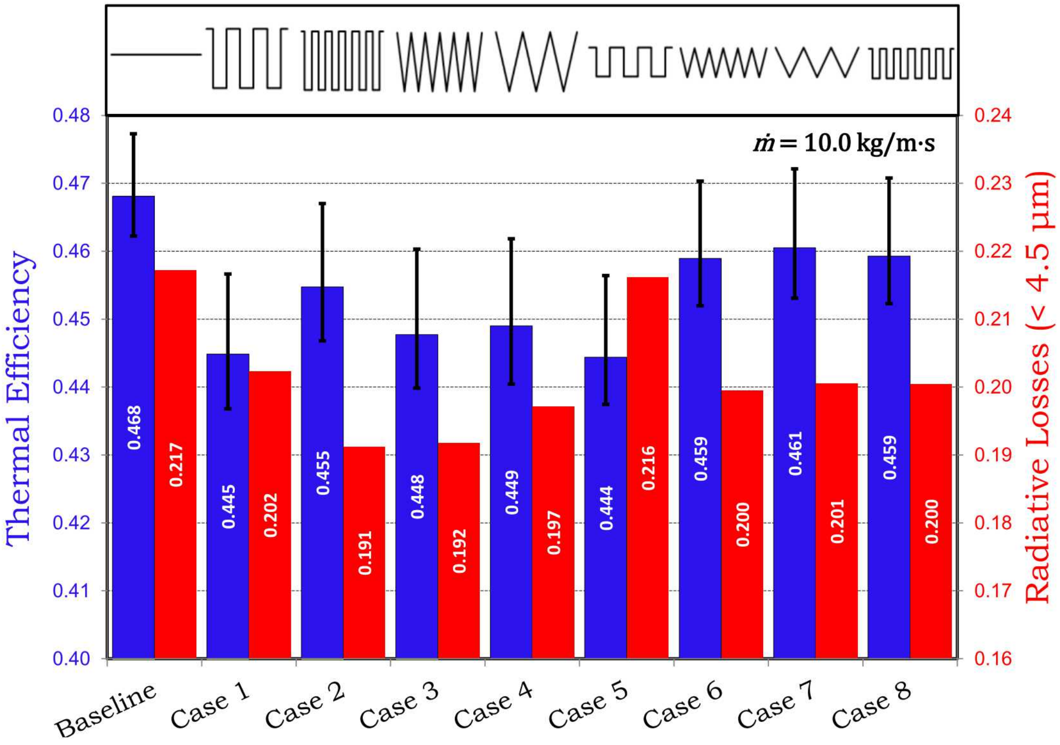

Figure 6. Simulated thermal efficiency and normalized radiative losses (< 4.5 µm) for cases 1-8 at high temperatures (600 – 720 °C).

The total radiative and convective losses from the wave-like release patterns explored in this study were calculated. The power output from each mechanism was normalized by the total incident radiative power to yield the percent of total incident power lost. The percent of incident power lost from the model that was not removed by the particles is presented in Figure 7 for cases 1-8 at 10.0 kg/m·s summarized by mechanism. The most striking difference in the results reported for here versus those reported for lower particle inlet temperatures was the significantly larger fraction of incident heat being removed by convection. Despite still observing lower total radiative losses in the volumetric release patterns, convective losses overwhelmed any gains from light trapping and volumetric heating. Radiative losses were again highest in the baseline case. It should be reemphasized that this model was expected to exaggerate convective losses, and the improving the geometry to minimize these losses may significantly improve the thermal efficiency. Other losses from the model including convective losses to the environment from the exterior walls still proved negligible.

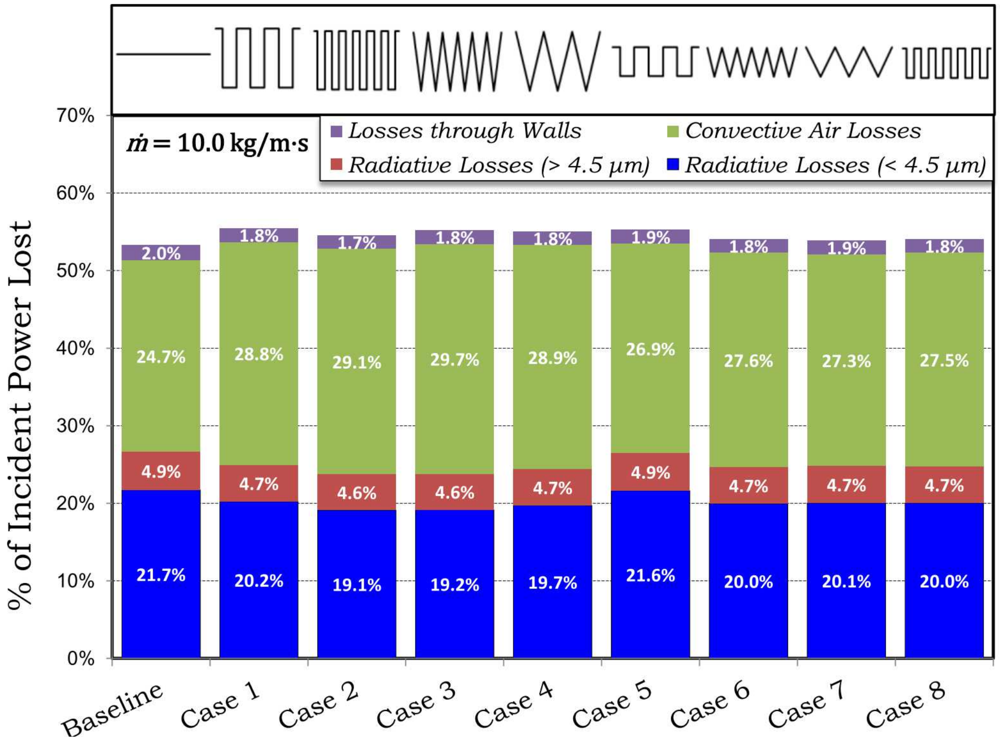

Figure 7. Percent of total incident power lost from each mechanism for simulated cases 1-8 at high temperatures (600 – 720 °C).

The parallel-line particle release patterns (Case 9-13 and 16) were explored along with the Case 14 and Case 15 which look at the effect of the release curtain within the receiver. The thermal efficiency for each of the volumetric release patterns is plotted in Figure 8 with its respective radiative losses for wavelengths < 4.5 μm for 10.0 kg/m·s. The percent of incident power lost from the model that was not removed by the particles is also presented in Figure 9 summarized by mechanism for 10.0 kg/m·s. As with the wave-like release patterns, most parallel-line release patterns also showed a lower thermal efficiency when compared with the Baseline configuration. Only Case 9, with three parallel lines showed improved thermal efficiency over the Baseline case, which suggested it was a very good candidate for improving the thermal efficiency. All volumetric release patterns explored indicated that light-trapping and volumetric heating effects were occurring, but were again overwhelmed by convective losses in the model. A surprising observation was that moving the Baseline release to the rear of the receiver significantly reduced the convective losses and increased the thermal efficiency. However, the gains in thermal efficiency from moving the curtain to the rear of the receiver may not extend to other receivers and was primarily an artifact of how air was allowed to enter and leave the domain in this model. Particle curtains at the rear of the receiver induced flow such that more cool air entering the domain through the aperture immediately left the domain with less interaction with the particles or receiver. The differences in the flow patterns between the Baseline case and Case 14 can be observed in Figure 10. Finally, Case 11 produced approximately the same result as Case 16 despite 1800 fewer injection sites confirming 300 injection sites was sufficient.

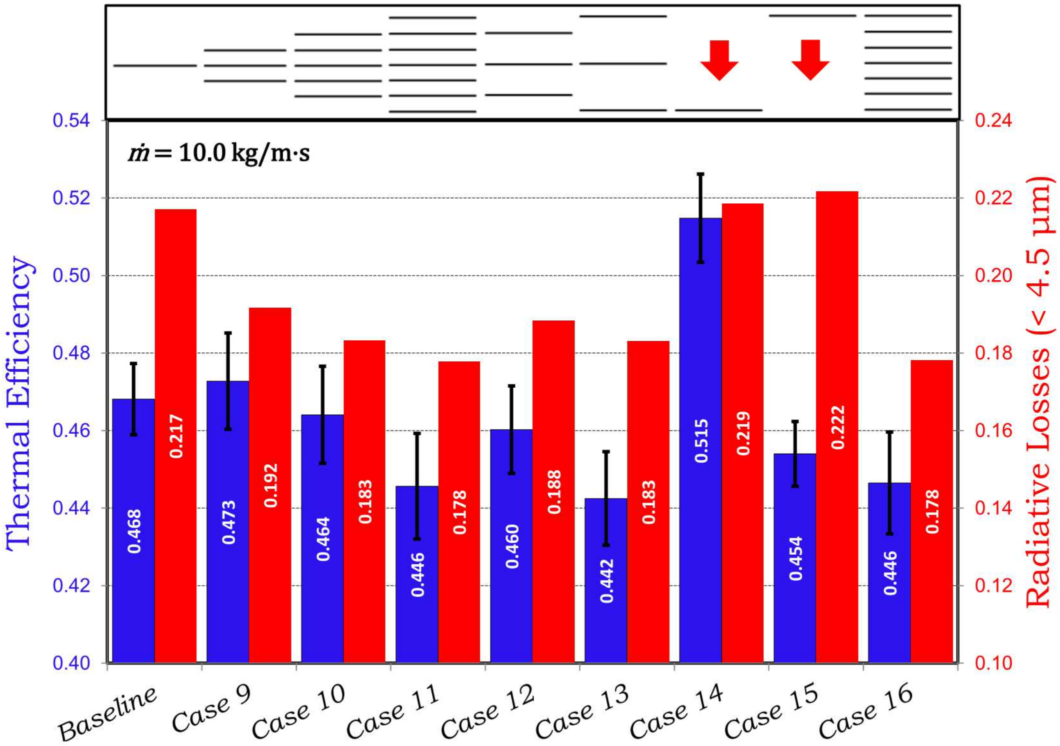

Figure 8. Simulated thermal efficiency and normalized radiative losses (< 4.5 μm) for cases 9-16 at high temperatures (600 – 720 °C).

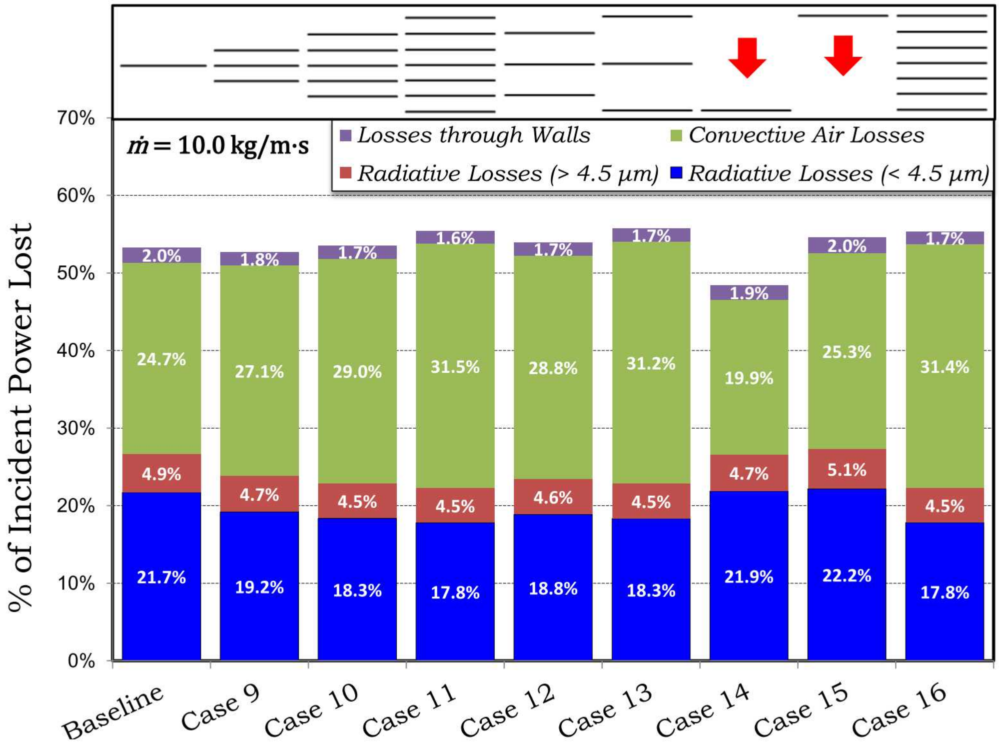

Figure 9. Percent of total incident power lost from each mechanism for simulated cases 9-16 at high temperatures (600 – 720 °C).

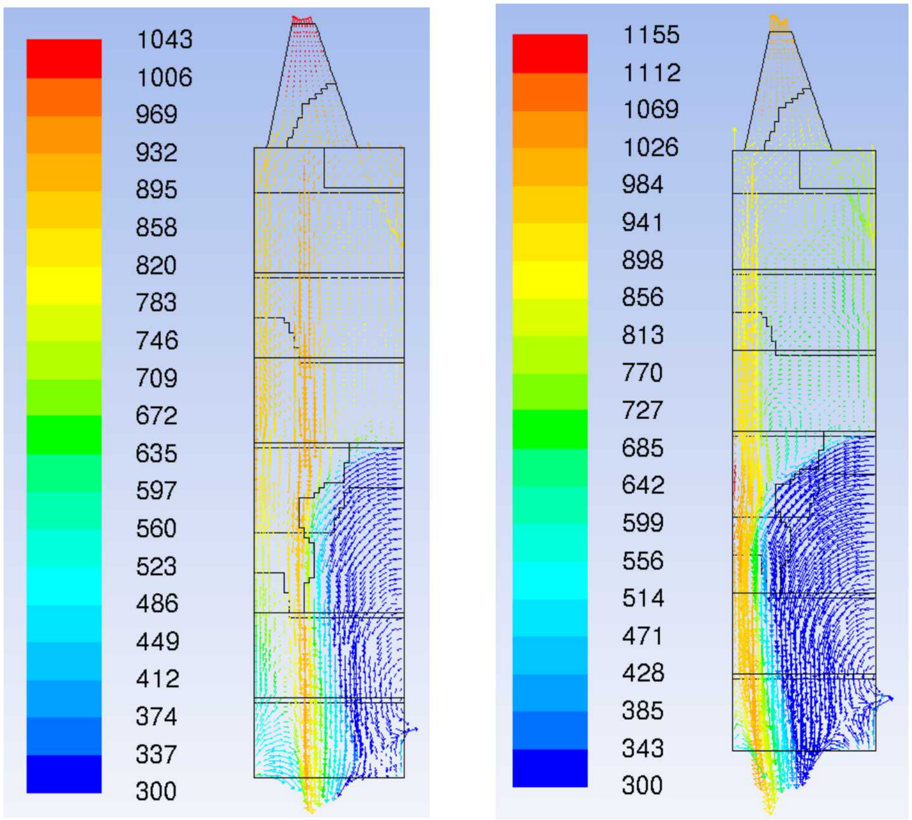

Figure 10. Simulated velocity vectors colored by temperature on the midplane for the Baseline case (left) and Case 14 (right). Temperature in K.

Gradients in the mass flow rate normal to the aperture were also considered for Case 10 with five parallel particle release lines. Distributing the mass flow rate such that the opacity of the curtain changed for each parallel line altered the distribution of temperatures in the particle curtains. Higher temperatures in curtains with higher mass flow rates may ultimately lead to higher thermal efficiencies but still retain the positive benefits from light-trapping and volumetric heating. As stated above, each mass flow rate gradient case was defined as a constant value *G* equal to the mass flow rate of the rear curtain divided to the front curtain with a linear transition across the inner curtains. That is, $G = 3$ indicates the rear curtain has a mass flow rate three times that of the front curtain (*i.e.* the curtain opacity increases moving away from the aperture). The thermal efficiency of each case at each mass flow rate was normalized to the thermal efficiency of the nominal Case 10 with a uniform mass flow rate distribution and plotted in Figure 11 for each gradient explored. Gradients with curtain opacity increasing moving further into the receiver ($G > 1$) showed increased thermal efficiency for all mass flow rates though diminishing returns were observed as mass flow rate increased. However, an asymptotic behavior was observed suggesting the gains were leveling off at the highest mass flow rates. Ultimately, larger values of G provided improved thermal efficiency, and at the highest mass flow rates, even higher values of G may further improve the gains in thermal efficiency.

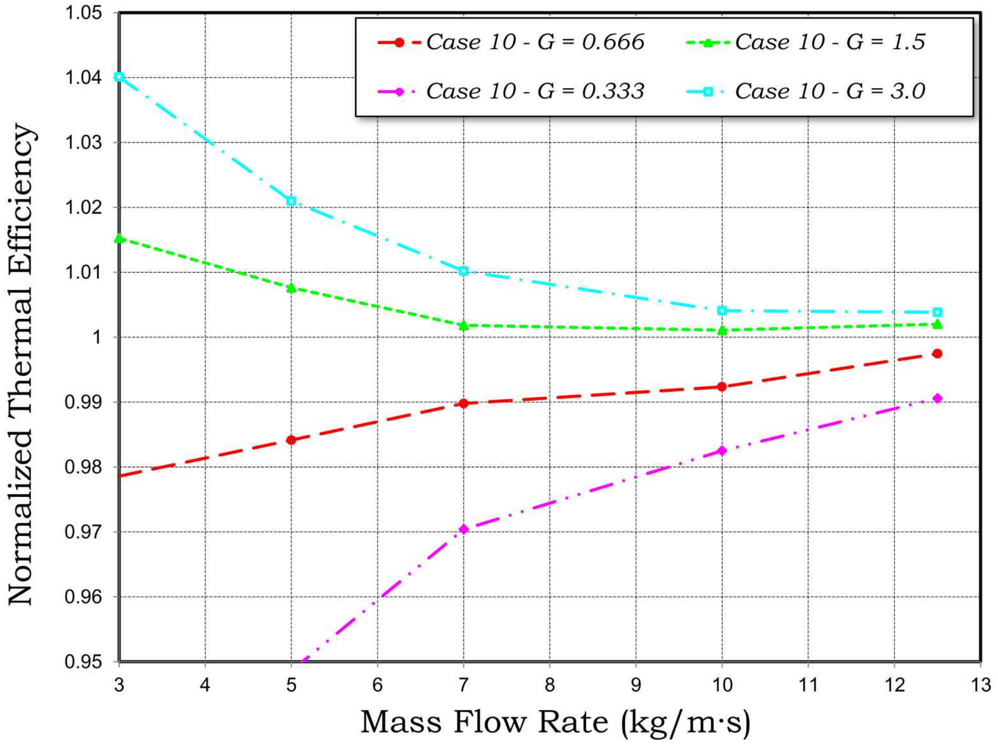

Figure 11. Simulated thermal efficiency normalized to Case 10 for each mass flow rate gradient at high temperatures (600 – 720 °C).

Cases 18-21 explored four mass flow rate gradients that varied laterally across the Baseline curtain. Radiative heat flux from the solar field created an approximately Gaussian distribution laterally across the curtain and concentrating more of the mass flow rate near the maximum heat flux increased heat transfer to the particles. A concise illustration of the cases explored is provided in Table 2. To reiterate, the top numbers in the scaled illustrations indicated the fraction of mass flow rate on that segment of the curtain and the bottom numbers indicated the length of that segment of the curtain. The thermal efficiency of Cases 18-21 at each mass flow rate are normalized to the thermal efficiency of the Baseline case in Figure 12. All lateral mass flow gradients explored showed equal or increased thermal efficiency relative to the Baseline case with the exception of Case 19 at the highest mass flow rate. However, as with the previous mass flow previous mass flow rate gradients, diminishing returns were observed as the mass flow rate increased. At the highest mass flow rates, little to no gains were observed in the cases explored.

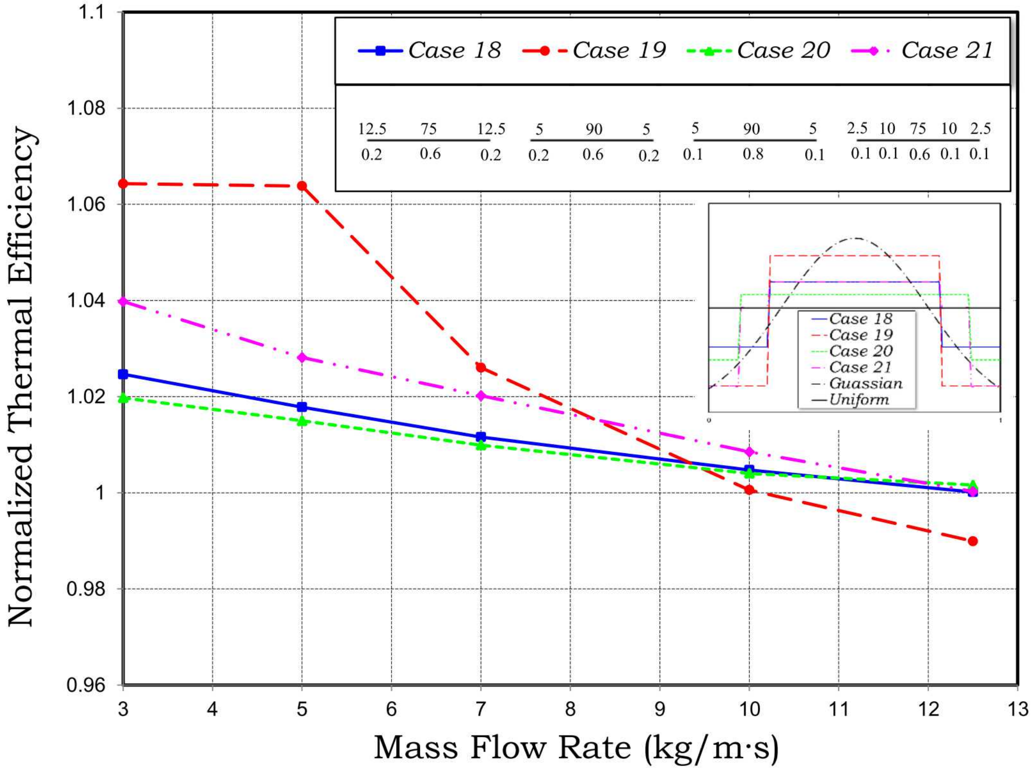

Figure 12. Simulated thermal efficiency normalized to the Baseline case for each lateral mass flow rate gradient at high temperatures (600 – 720 °C).

2.1.4. Optimization Study

An optimization strategy was also pursued to reveal favorable particle release patterns related to the parallel-line release patterns. The optimization strategy used a simulated annealing probabilistic approach where the thermal efficiency of the receiver was maximized. Ultimately, the goal of the optimization was not only to reveal a global minimum (if it could be found), but to explore several local minima in the process that may reveal insights into release patterns not presently investigated.

All parallel-line release patterns explored thus far (including mass flow rate gradients and Baseline configuration) were subsets of Case 11 where the mass flow rate of each release line was varied from 0 to 100% of the total mass flow rate under the constraint that the sum of release lines equaled the total mass flow rate. Using this framework to define the available parameter space to explore, the optimization strategy is described as follows. Starting with Case 11 as an initial point, each successive iteration of the optimization subtracted a random fraction of the existing mass flow rate from two release lines and distributed that mass flow rate to four other random lines. Thus, a new release pattern was created, but the total mass flow rate was preserved. Then, the model evaluated the thermal efficiency of that release pattern. If the thermal efficiency had increased from the previous iteration, then that release pattern was selected for the next iteration of the optimization. Otherwise, the previous release pattern was kept. However, to prevent the optimization from getting stuck in a local minimum, there is some probability that a release pattern was accepted with a lower thermal efficiency than the previous best iteration. The likelihood of this occurring increased the closer the thermal efficiency was to the previous best thermal efficiency and decreased as the optimization progresses.

Typically a simulated anneal approach as described above requires a very large number of samples to converge on a global minimum and there is no guarantee that it will. Due to the computational expense of running the model at each sample, it was unlikely that enough samples would be performed for the optimization to converge on the true global minimum. However, as mentioned before, a secondary goal was to explore other local minima that may reveal insights into favorable release patterns not presently explored. For this study, a total of 626 samples were performed.

Notable release patterns with their respective thermal efficiency explored in the optimization are included in Table 3. In the table, $\dot{m}_n$ provided the fraction of total mass flow rate in that line where n = 1 was the release line furthest from the aperture. As expected from the results of Case 14, release patterns that concentrated the mass flow rate near the rear of the receiver resulted in the highest thermal efficiencies. In fact, Case 14 (labeled as #1 in Table 3) was the most optimal release pattern found in the optimization process with a significantly higher thermal efficiency than all other cases. Though, it should be reemphasized (as depicted in Figure 10) that this was mostly an artifact of the outlet boundary condition and may not hold for other receivers optimized to minimize convective losses. Case 11 is labeled as #7 in Table 3 and its thermal efficiency was not significantly higher than the worst case found in the optimization labeled as #8.

Table 3. Notable particle release patterns found in the optimization.

#	$\dot{m}_1$	$\dot{m}_2$	$\dot{m}_3$	$\dot{m}_4$	$\dot{m}_5$	$\dot{m}_6$	$\dot{m}_7$	η_{th}
1	1.000	-	-	-	-	-	-	0.518
2	-	0.570	0.430	-	-	-	-	0.498
3	0.351	0.228	0.192	0.228	-	-	-	0.497
4	-	1.000	-	-	-	-	-	0.496
5	-	0.505	0.495	-	-	-	-	0.496
6	0.312	0.146	0.222	0.320	-	-	-	0.492
7	0.143	0.143	0.143	0.143	0.143	0.143	0.143	0.446
8	0.166	-	0.266	-	-	0.402	0.166	0.436

Case 17 was defined based on #3 labeled in Table 3 since it resulted in a very high thermal efficiency. Although it did not have the highest thermal efficiency, its high value suggested it might also have favorable light-trapping and volumetric heating effects. The mass flow rate gradient was also consistent with the results from Figure 11. The thermal efficiency was normalized to the Baseline case and showed significantly higher thermal efficiencies as illustrated in Figure 13. Furthermore, the thermal efficiency of Case 17, the Baseline case and four other significant particle release patterns for reference along with its respective radiative losses for wavelengths < 4.5 µm is plotted in Figure 14 for 10.0 kg/m·s. As depicted, Case 17 showed very low radiative losses for wavelengths < 4.5 µm lower than all other cases except those with significantly more parallel release lines. However, the largest part of its increase in thermal efficiency was still directly related to shifting the curtains deeper into the receiver.

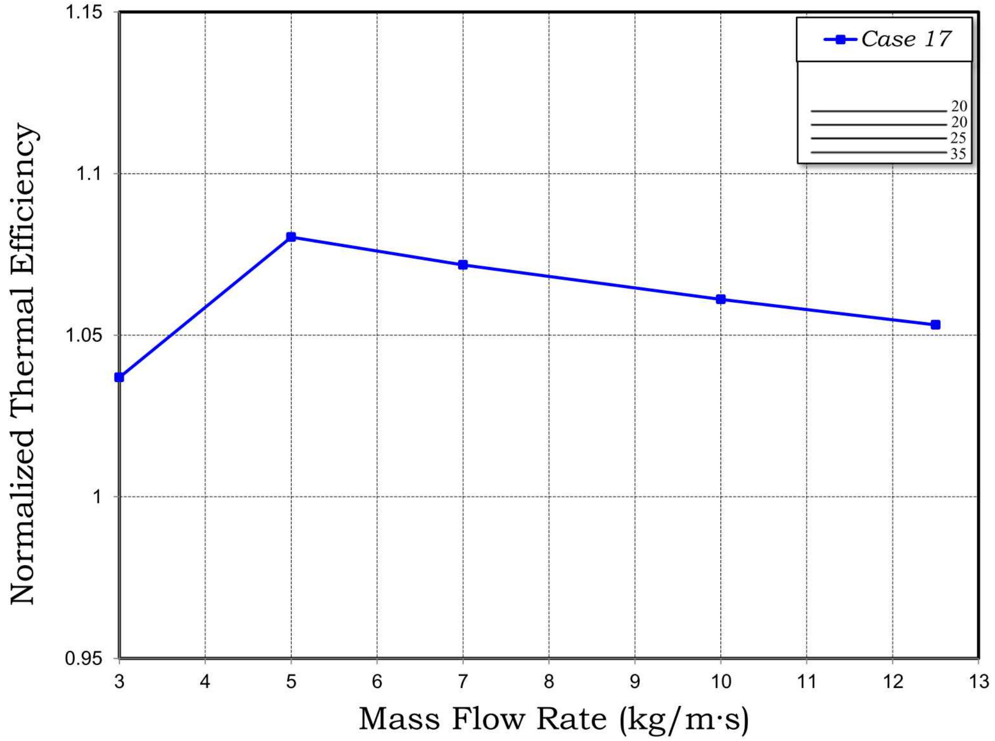

Figure 13. Simulated thermal efficiency of Case 17 normalized to the Baseline case.

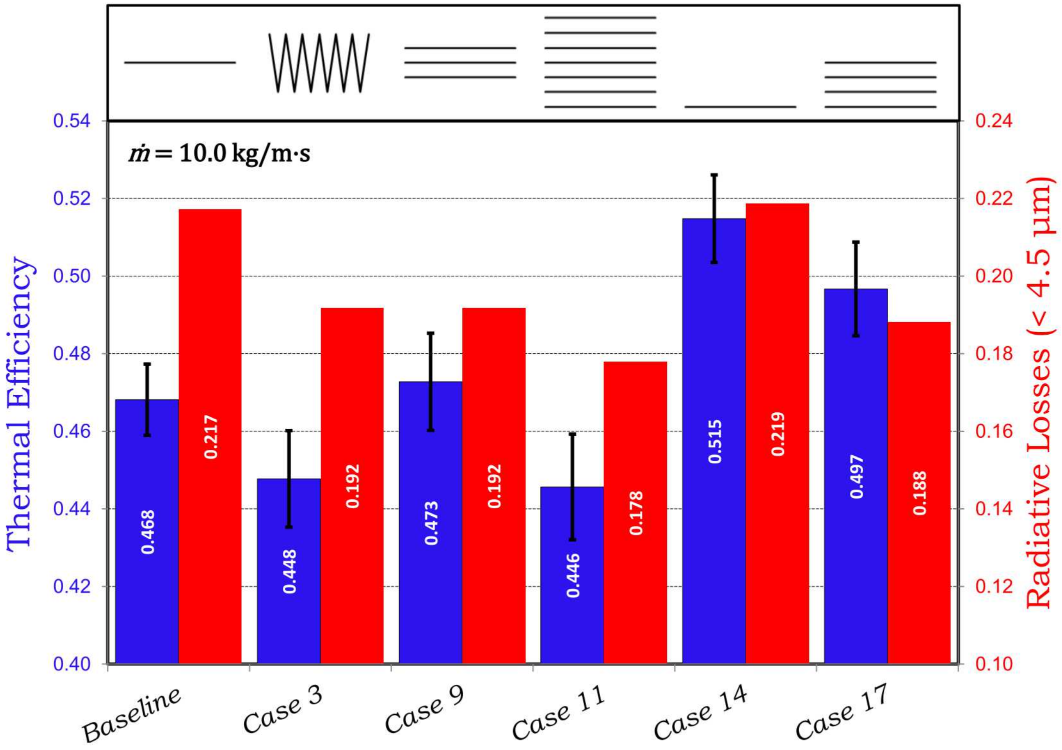

Figure 14. Simulated thermal efficiency and normalized radiative losses (< 4.5 μm) for cases 3, 9, 11, 14 and 17

To ultimately determine the best particle release pattern inside a particle receiver, the model must reflect actual receiver volume to capture the true convective flow within the receiver. Therefore, the model was modified to use the geometry of the existing particle receiver at the NSTTF at SNL. A solid model of the receiver along with the Fluent model is depicted in Figure 15.

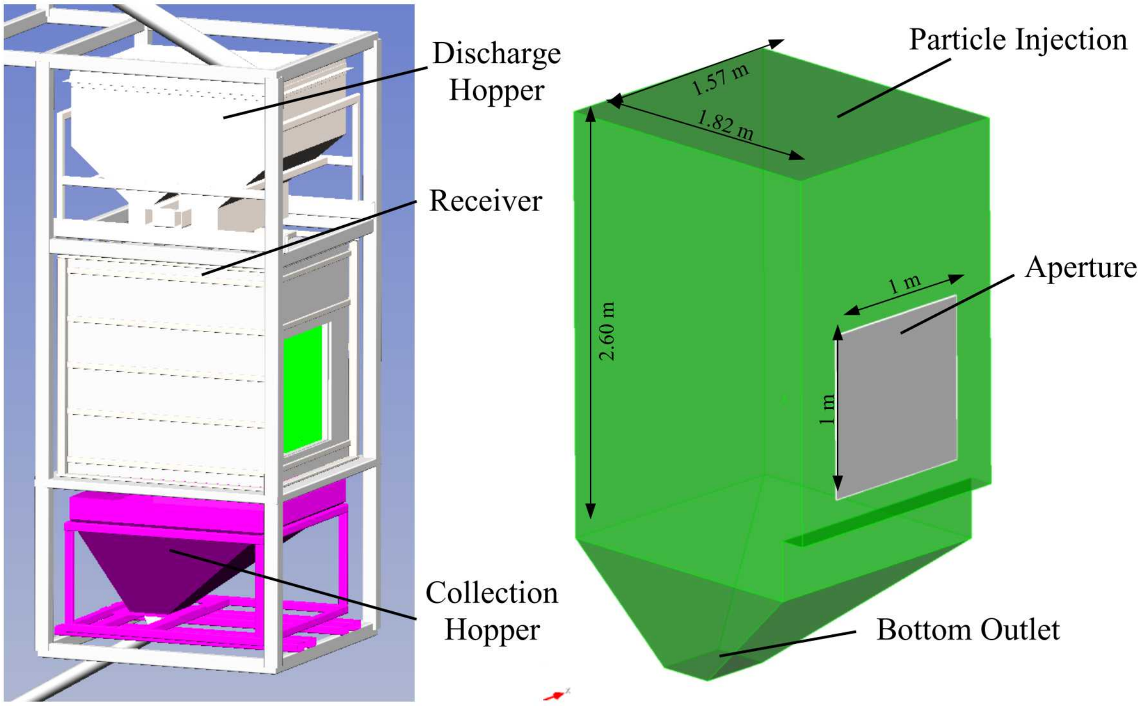

Figure 15. Solid model of the existing particle receiver at NSTTF (left) and the subsequent Fluent model (right)

The same physics used in the previous validated model were applied in this model to add confidence in the model's predictive capability. However, one primary difference between the two models was the use of the different solar patch technique described in Khalsa and Ho [14] as opposed to the fixed solar patch used previously. This solar patch technique has been specified to more accurately characterize heat transfer in and out of the aperture without the need to have a fixed 'solar patch' wall to obstruct the flow. Secondly, the hopper itself was defined to be a wall that only the particles can leave the domain whereas the previous model allowed air to leave out the bottom of the receiver. This will promote recirculation of the air within the receiver and be more consistent with the actual boundary conditions of a particle receiver.

As a preliminary test of the model, two volumetric particle release patterns from the wave-type and parallel-line release patterns, Case 3 and Case 9, respectively, were run and compared to a 'Baseline' planar release pattern for 10.0 kg/m·s. The velocity vectors along the midplane of the receiver were plotted for the Baseline case and colored according to the air temperature in Figure 16 to demonstrate the significant difference in the flow field and air temperature inside the receiver compared to Figure 10. The thermal efficiency from each release pattern was computed and summarized in Table 4. The thermal efficiency of both volumetric particle release patterns was also normalized to the Baseline case to demonstrate relative improvement. Both volumetric release patterns showed equivalent or improved thermal efficiency relative to the Baseline planar release.

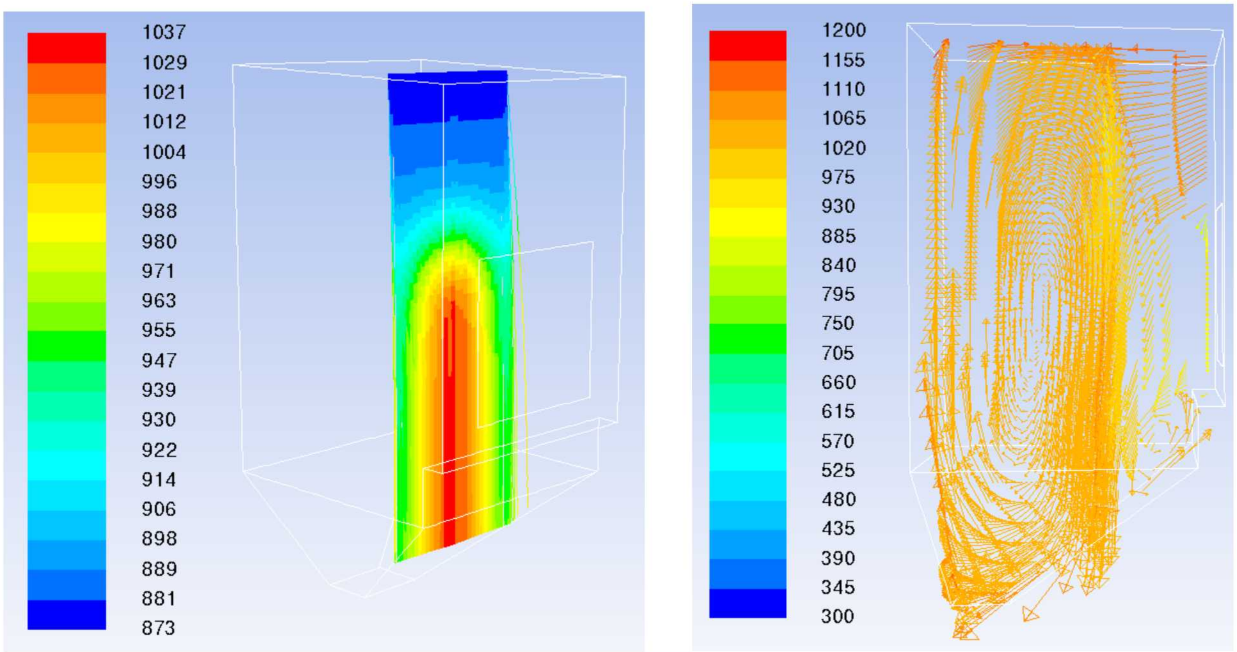

Figure 16. Simulated particle temperatures (left) and midplane velocity vectors colored by temperature (right) for the Baseline case using the new as-built model. Temperature in K.

Table 4. Simulated thermal efficiencies in the new particle receiver model

	η_{th}	$\eta_{th} / \eta_{th,\ baseline}$
Baseline	0.843	1.000
Case 3	0.846	1.004
Case 9	0.865	1.025

Future work for this model includes running a mesh convergence study to demonstrate solution converge in the latest particle receiver model as has been done in the previous model. Then, the model will be extended to test the most promising volumetric release patterns over the same range of flow rates before settling on a final particle release pattern that yields the most significant increase in thermal efficiency.

2.1.5. Summary of Computational Modeling in Q3 and Q4

In Q3, the work focused on investigating the effect of particle inlet temperature, investigating the effect of the particle release location within the receiver, investigating spatial mass flow rate gradients in the particle release patterns, and using an optimization strategy to explore unknown novel particle release patterns. It was found that increasing the particle inlet temperature greatly increased convective losses from the model and suppressed most gains in thermal efficiency from light-trapping and volumetric heating. However, the outlet flow boundary condition of existing model was found to overestimate convective losses by forcing cold inlet air to be introduced into the domain. A new model of the existing particle receiver that more accurately characterized the convective flow in the receiver was created to test the best designs identified in this parametric study.

Moving the particle deeper into the receiver was found to significantly increase the thermal efficiency; however, it was determined that this may simply be an artifact of the outlet boundary condition and may not extend to other receivers. Lateral and normal spatial mass flow rate gradients were found to increase thermal efficiency in the particle release patterns, but diminishing returns were found as the mass flow rate increased. Finally, a simulated annealing probabilistic approach was used to identify favorable particle release patterns. A release pattern was identified and modified based on the results of this parametric study to reveal a very favorable thermal efficiency compared to the baseline case at all mass flow rates.

Table 5 summarizes the performance evaluation criteria for the modeling of alternative particle release patterns. For the validated model of the previous on-sun tests, the wave-like particle release patterns produced efficiencies that were up to ~7% greater than the baseline planar curtain. At higher temperatures, recent models employing the as-built geometry of the current on-sun particle receiver system shows that alternative release patterns may increase the efficiency by several percentage points. Modified receiver designs can further reduce convective heat loss through trapping of hot air and minimizing entrainment of cold ambient air into the aperture. Conductive heat losses through the walls of the receiver were also found to be significant (see Section 4.1).

Table 5. Performance evaluation criteria for modeling novel release patterns.

	Metric Definition (From Measurement)	***Success Value***	***Assessment Tool (Quality Assurance)***	***Goal Met (Y/N)***	***Supporting Data***
Project Evaluation Criteria 1.1.1	Modeled increase in thermal efficiency relative to baseline $FOM = \frac{\eta - \eta_b}{\eta_b} x100$ where $\eta = \frac{Q_{absorbed} - Q_{heat\ loss}}{Q_{incident}}$	> 5% (for $\eta_b \geq 90\%$, percentage increase may be 2%) Constraint: $T_{p,outlet} \geq 720°C$	Parametric analysis evaluating alternative wave designs; ANOVA analysis determining most effective parameters; evaluate main effects and interactions	Yes, FOM up to ~7% for T_{out}<300°C FOM up to ~2 - 3% for T_{out}>700°C and η_b ~ 84%	Figure 5, Table 4

Overall, the parametric study revealed that both wave-like and parallel curtain particle release patterns could increase the thermal efficiency of the receiver at elevated temperatures over a conventional planar release. For particle mass flow rates of 5 and 10 kg/ m·s, the thermal efficiency could be increased up to 4.6% and 2.5%, respectively. Increasing the number of parallel curtains, increasing the spacing between curtains, and shifting the release pattern deeper in the receiver cavity was all found to increase the thermal efficiency. These effects became less significant as the particle mass flow rate increased.

2.2. Testing

2.2.1. Testing Approach

Discharge plates with different slot patterns were machined to characterize the particle flow stability and mass flux of 16 different particle release patterns (Figure 17). These designs were based on the numerical studies that evaluated linear curtain patterns, triangular wave patterns, square wave patterns, and parallel curtain wave patterns. Each design has a low/high value for wavelength, amplitude, slot aperture, and/or spacing between multiple parallel curtains. The parallel curtain slots were spaced equally, and the amplitude for these cases is defined as the distance between each slot.

Figure 17. Different wave-like and parallel-line slot patterns machined into steel plates to evaluate alternative particle release patterns.

The "cold flow" particle receiver test apparatus described in Ho et al. [15, 16] was used in the current particle flow tests to evaluate particle stability. Digital imaging methods similar to those described in Ho et al. [15, 16] to characterize the particle stability were used. A camera was mounted on the side of the test apparatus that can be adjusted to achieve a perpendicular view of the falling particle curtain. A 2.54 cm x 2.54 cm square partitioning grid can be maneuvered across the particle curtain to localize particle flow along the drop length for thickness measurements. Fluorescent lights were installed on either side of the particle curtain to adequately light the grid pattern with uniform, diffuse lighting. Figure 18 shows photos of the digital imaging system. A

Matlab model was developed to process digital images and track curtain stability (particle curtain thickness and offset from the release location) as a function of drop height. The software analyzes both the average and standard deviation of the curtain thickness and offset for a prescribed set of digital images along the drop length.

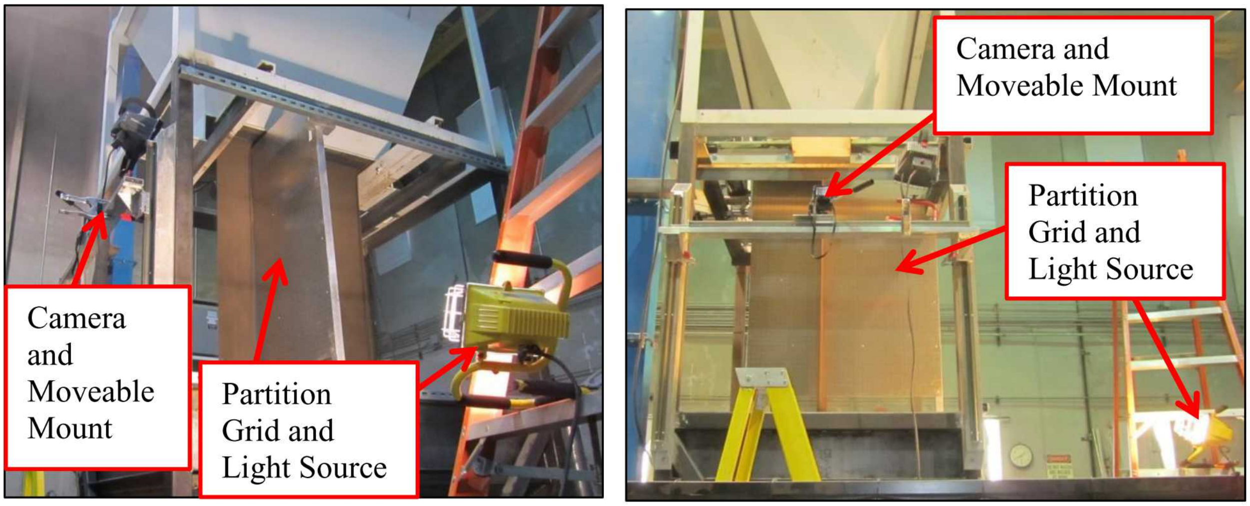

Figure 18. Left: Front-Side looking view of the particle curtain image system. Right: Side looking view of the particle curtain image system.

Table 6 shows representative images of parallel, triangular, and square-wave particle release patterns produced by the discharge plates. In general, the machined slot patterns produced fairly stable particle flows and features that matched the slot pattern. The parallel slot cases with close spacing (slots separated by less than several centimeters) produced coalescing particle curtains after ~1 – 2 meters of drop length.

Table 6. Representative Images of the Parallel, Triangular, and Square wave patterns

Parallel Slots (2 slots) – side view	Parallel Slots (5 slots) – side view	Triangular Wave – front view	Square Wave – front view
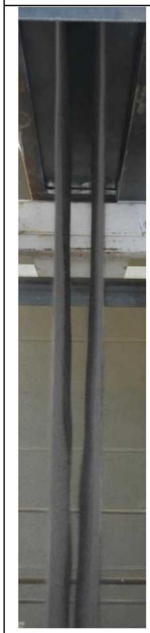			

2.2.2. Testing Results

To illustrate the particle curtain thickness variation as a function of drop distance, a 5-slot parallel curtain design is shown in Figure 19. Each curtain is spaced 4.4 cm apart, and each slot aperture is 6.35 mm. The parallel curtains appear stable over the first meter of drop, and the average curtain thickness is measured to be ~1 cm. The decrease in curtain thickness in the first 0.5 m of drop is caused by vena contracta (convergence of streamlines exiting a small opening) and/or pressure differentials between the inner and outer regions of the particle curtain as the air is entrained by the falling particles (Bernoulli effect). In the Bernoulli effect, the higher velocity in the interior of the curtain causes lower pressure, which causes the particles to converge. However, as the particles accelerate and separate, additional drag causes dispersion and increasing particle curtain thickness.

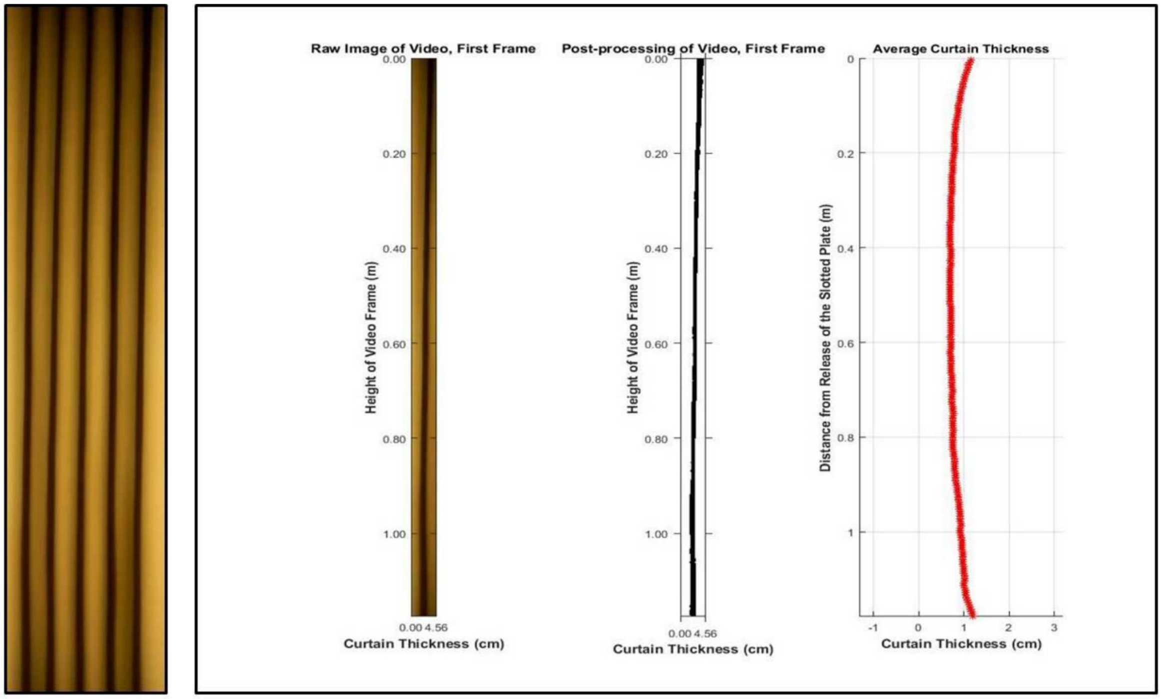

Figure 19. Image of 5 parallel curtains (left) and Matlab analysis of a single curtain from the video (right).

Table 7 summarizes the release patterns for the sixteen plates evaluated during the cold flow testing, along with results for the particle mass flow. Three mass flow measurements were made for each of the release patterns using a hopper that was placed beneath the particle flow for a prescribed period of time and subsequently weighed. Performance evaluation criterion (PEC) 1.2.2 provides a minimum mass flux of particles (>400 kg/m^2-s) to be commensurate with anticipated commercial-scale systems. Table 7 shows that the lower-bound mass flux using a *t*-test with 3 mass-flow measurements and a 95% confidence interval meets the desired metric in all of the cases.

Table 7. Sixteen particle drop patterns evaluated for flow stability under ambient conditions; Amplitude for the parallel slots is defined as the outer edge-to-edge distance of the outer-most slots.

Plate Number	Pattern Type	Number of Slots	Slot Aperture Thickness (cm)	Amplitude=Distance Between Slots (cm)	Wavelength (cm)	Total Slot Length (m)	Average Mass Flow Rate (kg/s/m)	Average Mass Flux (kg/s/m2)	Lower-bound mass flow (95% CI) (kg/s/m)	Lower bound mass flux (95% CI) (kg/s/m^2	Maximum Drop Distance for Scaled Receiver (m)
1	Parallel Slots	2	0.64	6.35	n/a	1.50	2.91	458.09	2.85	448.53	2.11
2	Parallel Slots	2	0.64	16.51	n/a	1.50	3.19	501.73	3.18	500.79	4.22
3	Parallel Slots	2	1.11	5.38	n/a	1.50	6.68	600.70	6.43	578.84	2.34
4	Parallel Slots	2	1.11	15.54	n/a	1.50	6.76	608.00	6.74	606.25	4.12
5	Parallel Slots	5	0.64	1.12	n/a	1.50	2.67	419.97	2.64	415.01	0.08
6	Parallel Slots	5	0.64	3.63	n/a	1.50	2.57	405.34	2.57	404.51	1.68
7	Parallel Slots	5	1.11	0.51	n/a	1.50	7.64	687.83	7.28	654.99	0.03
8	Parallel Slots	5	1.11	3.05	n/a	1.50	6.08	547.54	6.03	542.95	1.32
9	Square Wave	1	1.11	7.62	7.62	0.58	6.73	605.85	6.71	604.16	4.25
10	Square Wave	1	1.11	7.62	25.40	1.03	7.10	638.60	6.74	606.59	5.46
11	Square Wave	1	1.11	17.78	7.62	1.19	6.31	567.51	6.27	564.34	Not Distinguishable
12	Square Wave	1	1.11	17.78	25.40	1.64	6.79	610.68	6.74	606.91	8.89
13	Triangular Wave	1	1.11	7.62	7.62	0.41	7.39	665.13	7.32	658.59	5.41
14	Triangular Wave	1	1.11	7.62	25.40	0.85	7.00	629.56	6.93	623.42	2.66
15	Triangular Wave	1	1.11	17.78	25.40	1.23	7.06	635.59	6.89	619.82	4.03
16	Triangular Wave	1	1.11	17.78	7.62	0.85	7.08	637.21	6.68	601.14	10.94

PEC 1.2.1 evaluates the thickness of the particle curtain, t_1, during free-fall through the receiver and the associated maximum drop distance, d_2, of the curtain before the volumetric features become indiscernible. This relationship is described by the following expression assuming a linear growth of the particle curtain thickness [17]:

$$t_1 \le \frac{d_1}{d_2}\frac{A}{2} \quad or \quad d_2 \le \frac{d_1}{t_1}\frac{A}{2} \tag{3}$$

where d_1 is the drop distance at the location of the measured curtain thickness in the tests (~1 m), and A is the amplitude of the wave form. Eq. (3) provides a design standard that ensures that the particle curtain thickness at a larger-scale drop distance of d_2 does not exceed half the amplitude of the release pattern. The average particle curtain thickness, t_{avg}, in the cold-flow tests is obtained from digital video images, and the 95% confidence interval is calculated using a t-distribution. The upper bound of the particle curtain thickness, t_1, is calculated as follows and used in Eq. (3):

$$t_1 = t_{avg} + t_{\alpha/2,n-1}\frac{\sigma}{\sqrt{n}} \tag{4}$$

where σ is the standard deviation of the particle curtain thicknesses, n is the number of samples, and $t_{\alpha/2,n-1}$ is the critical t-statistic for a (1-α)*100 confidence interval with n-1 degrees of freedom. Note that the t-statistic is unrelated to the nomenclature used for the particle curtain thickness, t.

Figure 20 shows the maximum allowable drop distance according to Eqs. (3) and (4) for each of the 16 different release patterns tested. A clear trend in the features that led to more persistent features (less spreading) relative to the given amplitude of each pattern was not observed. However, the results illustrate that Eqs. (3) and (4) can be used to determine a maximum drop distance for a given amplitude, or, conversely, the required amplitude necessary to maintain the shape of a desired release pattern for a prescribed drop distance. It should be noted that although the offset of the particle curtains has been measured, only the particle curtain thickness and spreading have been used to determine the maximum drop distance thus far. Both the spreading of the curtain thickness and the relative offset of the curtains, especially for parallel curtains, will impact the persistence of the release pattern.

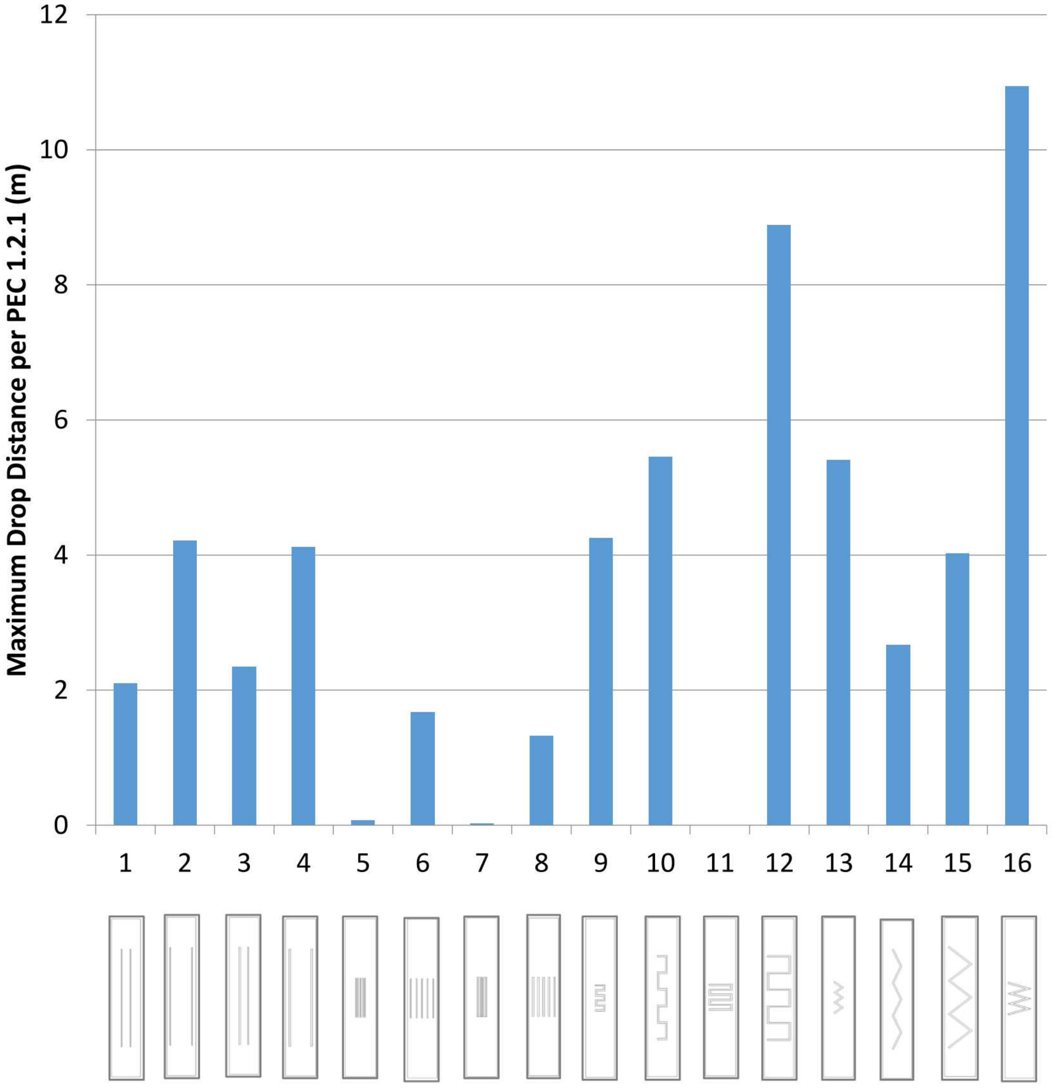

Figure 20. Maximum allowable drop distance per Eq. (3) under ambient conditions.

2.2.3. Summary of Particle Flow Testing

Table 8 summarizes the performance evaluation criteria for the particle flow tests in Task 1.2. The measurement of the particle curtain spread was used in a relationship to determine either the maximum drop distance or minimum amplitude (or separation distance for parallel lines) required to maintain a distinguishable pattern. Mass flow measurements were performed for each of the alternative release patterns, and the measured mass flux (lower bound of the 95% confidence interval using a student t-test) exceeded the metric of 400 kg/m^2-s.

Table 8. Performance evaluation criteria for testing novel particle release patterns.

	Metric Definition (From Measurement)	***Success Value***	***Assessment Tool (Quality Assurance)***	***Goal Met (Y/N)***	***Supporting Data***
Project Evaluation Criteria 1.2.1	Maximum change in average particle curtain thickness, t_1, along small-scale particle drop distance, d_1, of 1 m	$t_1 < \frac{d_1}{d_2}\frac{A}{2}$ where d_2 is the hypothetical drop distance of a larger-scale receiver, and A is the amplitude of the wave form	Student's t-test using 95% confidence interval	Yes	Eqs. (3) and (4); Figure 20
Project Evaluation Criteria 1.2.2	Measured mass flux of particles	>~400 kg/m^2-s (where area is based on discharge slot area) Constraint: Must be able to operate at temperatures up to 750°C	Student's t-test using 95% confidence interval	Yes	Table 7

2.3. Summary of Novel Particle Release Patterns

Computational models of "fractal-like" or volumetric particle release patterns were developed to evaluate the impact of various features summarized in Figure 3 and Table 6. Initial wave-like release patterns (triangular and square) were explored in Q1 and showed that the thermal efficiency could be increased by ~7% due to increased light trapping and reduced radiative losses, despite increased convective losses from the increased surface area of the exposed particle curtain. A larger amplitude and shorter wavelength of the wave-like patterns was found to increase the light trapping. Hence, in Q2, we investigated additional parallel-line release patterns with varying separation distances and numbers of lines as a function of particle mass flow rate. In Q3 and Q4, we investigated higher temperatures, mass flow gradients both normal and perpendicular to the incident radiation, release location, and more realistic convective boundary conditions. Results show that volumetric particle release patterns can increase the thermal efficiency by reducing radiative heat losses, in particular reflective losses. At higher temperatures > 700 °C, convective losses were found to be significant due to the higher exposed surface area and must be controlled.

Table 9. Summary of particle release patterns and features explored in computational parametric study

Feature	Result
Increased Particle Inlet Temperature	• Significantly increased convective losses for volumetric particle release patterns • Most patterns showed lower thermal efficiencies relative to a planar release, but convective losses were likely overestimated
Lateral Mass Flow Rate Variation	• Increased thermal efficiency, but diminishing returns were observed as mass flow rate increased
Release Location Within Receiver	• Moving particle release to the rear of the receiver significantly decreased convective losses • Gains in thermal efficiency may not be consistent across all receiver geometries
Wave-Like Particle Releases	• Small wavelengths and large amplitudes showed the lowest radiative losses; light-trapping effects observed • Thermal efficiency gains were reduced as particle inlet temperature increased due to increased convective losses
Parallel-line Particle Releases	• More lines decreased radiative losses, but increased convective losses; light-trapping effects observed • Thermal efficiency gains were reduced as particle inlet temperature increased with exception of Case 9
Normal Mass Flow Rate Gradients	• Gradients with increasing opacity moving away from the aperture showed higher thermal efficiencies in parallel-line releases • Diminishing returns were observed as mass flow rate increased

Particle-flow testing revealed that machined slots in the discharge plates could be used to implement the alternative particle release patterns. In general, the features of the alternative patterns were retained over the small-scale drop distance (1 – 2 m). In the parallel line cases, short distances between the parallel lines (< 3 – 4 cm) resulted in coalescing particle curtains. A relation between the curtain spread, drop length, and amplitude (or separation distance between parallel lines) was developed to predict the maximum drop distance for a given amplitude (or separation distance) or a minimum amplitude (or separation distance) for a prescribed drop distance. The impact of wind and air currents within a heated cavity receiver was not investigated and may pose challenges to maintaining the geometry of these novel release patterns during actual operation.

3. PARTICLE MASS-FLOW CONTROL AND MEASUREMENT

3.1. Particle Mass-Flow Control

The goal of particle mass-flow control is to regulate the particle flow into the receiver to accommodate changes in the irradiance and environmental conditions while maintaining a constant particle outlet temperature. Higher particle mass flow rates will reduce the particle temperature rise for a given irradiance on the particles due to increased shading, and vice-versa. Thus, if the irradiance reduces (e.g., due to clouds) or if the wind increases (increasing the heat loss), the particle mass flow rate can be reduced to maintain the desired particle outlet temperature. If the irradiance increases, the particle mass flow rate can be increased to maintain the outlet temperature. This section describes the design, testing, and evaluation of an automated particle mass-flow control system.

3.1.1. Design

Two designs were initially considered to control the mass flow of particles from the top hopper into the receiver: a slide-gate design and a hinged-gate design. The slide gate was determined to be the most feasible alternative. It was the easiest to construct, required the fewest modifications to the existing on-sun receiver structure, and provided the most direct control of the particle stream. Other designs that were initially screened out included ball joints and rotary valves due to sticking and binding (from the particles) that was been observed in previous tests.

The slide-gate mechanism has a horizontal plate of stainless steel actuated by a single linear drive table (Figure 21). The gate is supported on the sides by rails to prevent cantilever bending. The linear drive table has a bidirectional precision of 3 microns and a screw lead of 10 mm. When coupled with a MPP100 motor and a 3:1 gearbox, the movement precision of the setup is less than 1 mm. The slider gate design allows for direct mass flow control with a minimum of moving parts.

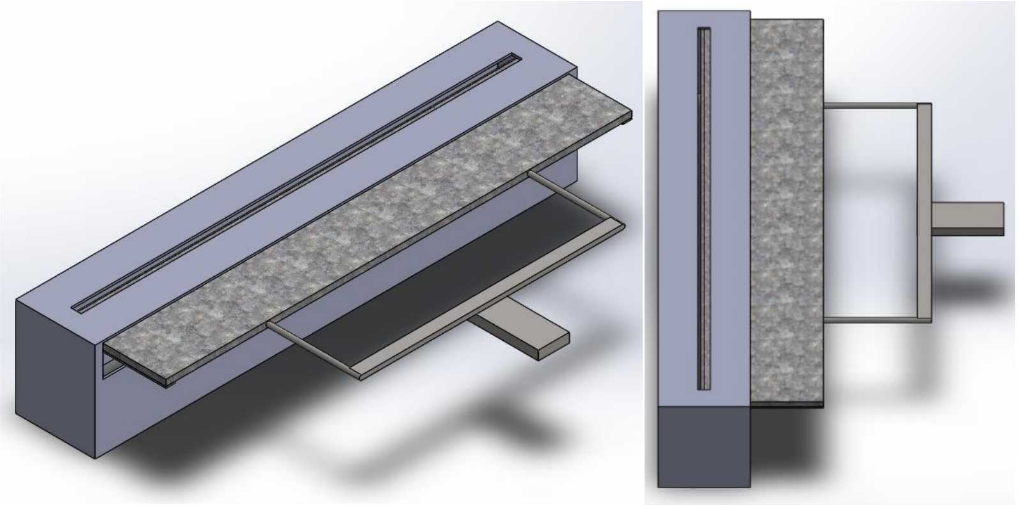

Figure 21. Two views of slide-gate design.

Ceramics and other high temperature alloys with very low thermal expansion coefficients (such as Kovar, Invar, Silicon Carbide, Alumina, etc.) were considered to serve as the gate component. Following careful consideration, a material with very low thermal expansion was determined to be unnecessary for our application. Therefore, 304 stainless steel was determined to be suitable for this project as it is relatively cheap, has an acceptable thermal expansion coefficient, and can be easily machined.

Three actuation mechanisms were considered for this project: hydraulics, pneumatics, and electrical motors. Hydraulic systems can easily provide sufficient force. However, to get the accuracy required the system would need servo-hydraulic components such as a servo controller, electrohydraulic servo valve, and a linear transducer. In addition, hydraulic systems require continuous inspection and maintenance to ensure the seals have not failed and the movement of the system is repeatable and accurate. Temperature also alters the working fluid's properties, adding to the difficulty of repeatable and reliable motion. Pneumatic actuators were also considered for this application, but the available space for the on-sun receiver did not allow for the size of the pneumatic actuator and air compressor that would be required to exert the force required.

Thus, an electromechanical system was chosen for our prototype design. Electrical servo-motors, combined with a lead screw and gearbox, are able to exert the required force and minimum movement that this application requires. In addition, they are able to be reliably programmed such that movements are repeatable and human interaction is minimal. There is minimal maintenance, minimal footprint, and minimal structure addition to support the motor and linear actuator.

3.1.1.1. Thermal and Structural Modeling

The slide gate was modeled and simulated in Solidworks Simulation. Steady state thermal, static, and buckling analyses were performed. All components of the slide gate were made from 304 stainless steel. This material was chosen due to its relatively low cost and availability. The coefficient of thermal expansion of 304 stainless steel is $1.8e^{-5}$/K, low enough to be able to reasonably accommodate the material's expansion. Figure 22 shows the slide gate design. The arms are 0.0508 x 0.0508 x 0.00635 m (2 x 2 x 0.25 in) square tube. The plate that will interact with the particle stream is 0.203 x 1.492 x 0.0254 m (8 x 58.75 x 1 in). Underneath the plate to help prevent vertical deflection are two square tubes, each 0.0254 x 0.0254 x 0.003175 m (1 x 1 x 0.125 in).

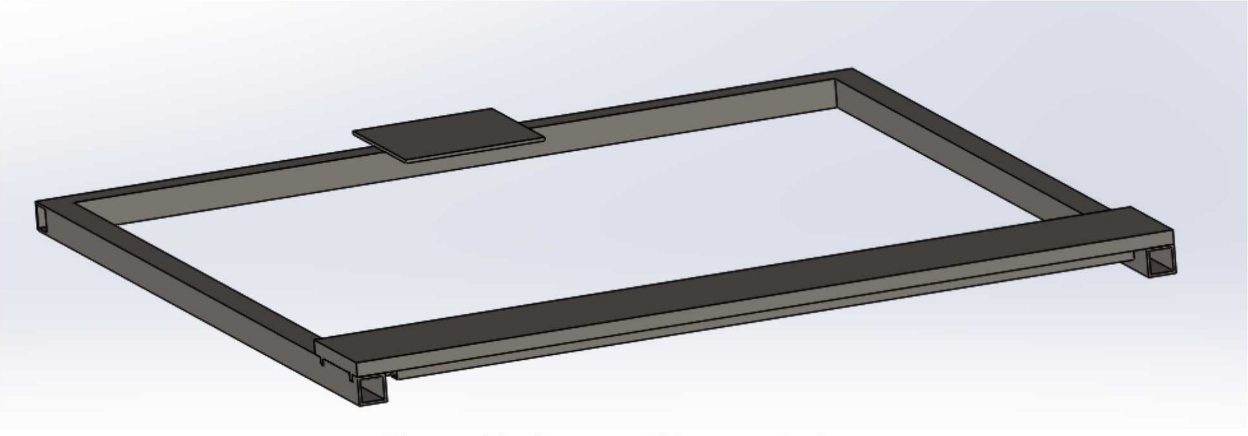

Figure 22. On-sun slide gate design.

Figure 23 shows the steady state temperatures with a 600°C load applied to the surface of the plate and a convection coefficient of 5 $W/m^2/K$ applied to the exposed faces of the square tubes. Results show that the high-temperatures are confined near the plate that will be in contact with the particles. Particle temperatures are expected to reach 750°C after being irradiated as they fall through the receiver. However, particles will only be moved to the top hopper and released from it once their energy has been transferred to another medium or dissipated to the ambient. Therefore, the slide gate is expected to be subjected to temperatures below 600°C.

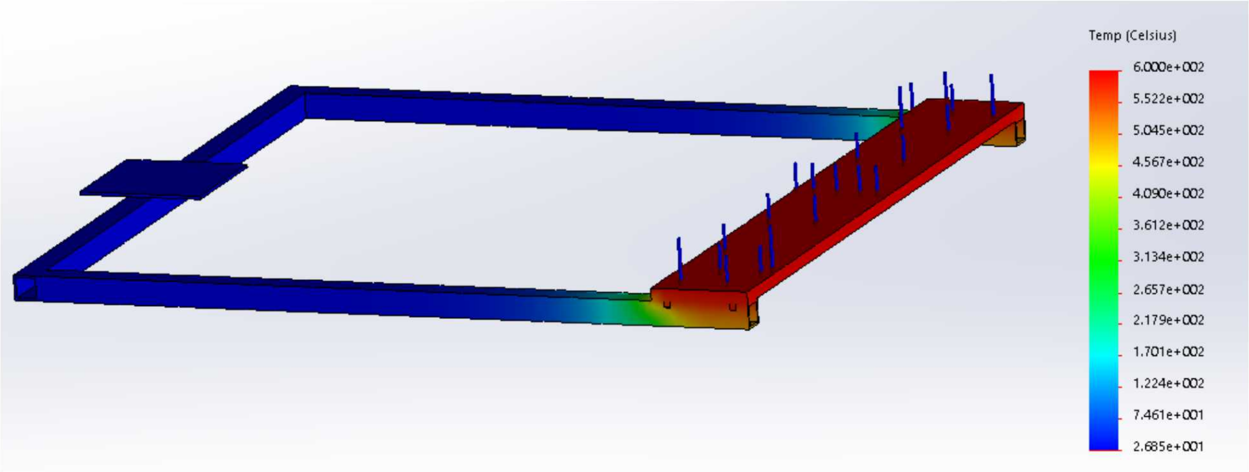

Figure 23. Simulated steady-state temperature response for the on-sun slide gate design. Applied thermal load of 600°C is to the top of the plate.

Figure 24 shows the stresses induced in the system from the steady-state temperature profile shown in Figure 23. A load of 2,030 N (corresponding to a FOS = 3) is also applied vertically to the plate. This force is representative of the weight of a column of particles extending from the top hopper's 1-inch slot to the top of the hopper. A horizontal force of 4,080 N (corresponding to a FOS = 1) is applied horizontally to the arms of the slide gate design. This force represents the maximum axial force the linear actuator component can withstand, and therefore will be allowed to exert. This maximum horizontal force will only be manifested if the slide gate becomes stuck due to friction or some unforeseen reason. Results show that the maximum predicted thermal stresses are less than the yield stress.

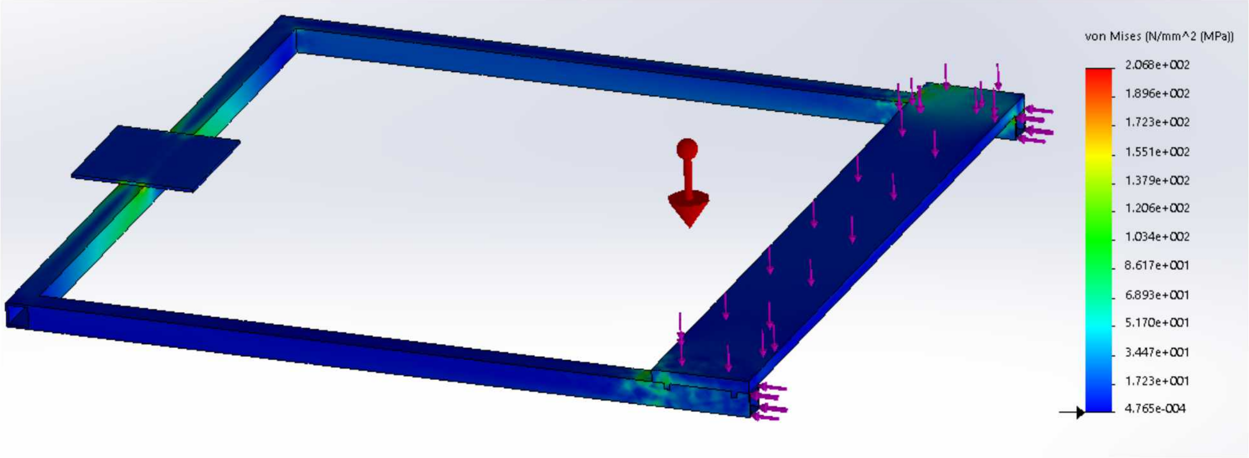

Figure 24. Simulated stresses due to the particle weight and maximum axial force the linear actuator will be allowed to exert.

Maximum deflection was estimated to be 1.5 cm along the long axis of the gate due primarily to the thermal expansion of the steel. The maximum vertical deflection due to the vertical forces was 1.68 mm in the middle of the plate as shown in Figure 25. These deflections were deemed acceptable for our application.

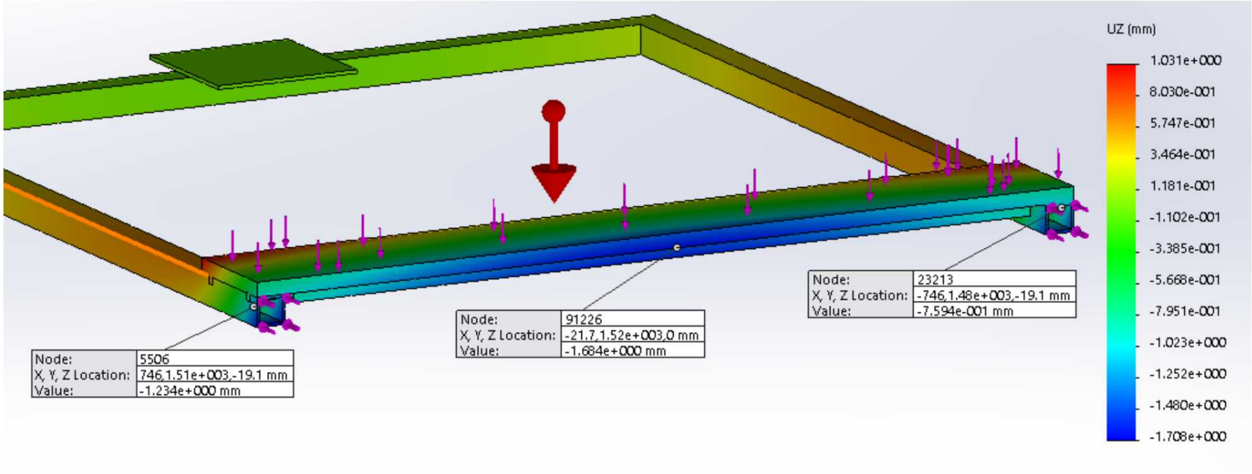

Figure 25. Simulated vertical displacement of the plate's leading edge. Maximum is 1.68 mm in the center.

3.1.1.2. Slide Gate Force Estimation and Minimum Vertical Clearance Required

The force required to move the slide gate using the electromechanical motor was determined by using an existing hydraulic slide gate. A pressure gauge attached to the hydraulic line was used to determine the force required to move the gate into and out of the particle flow. Two hydraulic rams were used to operate the gate; therefore, the force determined to be exerted from the gauge was multiplied by two.

The plate was positioned flush to the top hopper and the bolts re-tightened to ensure no change in position during testing. The gate was opened and closed five times to determine the average hydraulic pressure during operation. The results of the testing with the gate set flush and at 0.254 mm, 0.508 mm, 1.016 mm, and 2.032 mm away from the bottom slot of the top hopper are shown in Figure 26. Since the maximum force that the servo motor can provide is 4 kN, these results show that a separation distance between the slide gate and top hopper of > ~1 mm should yield an acceptable required closing force.

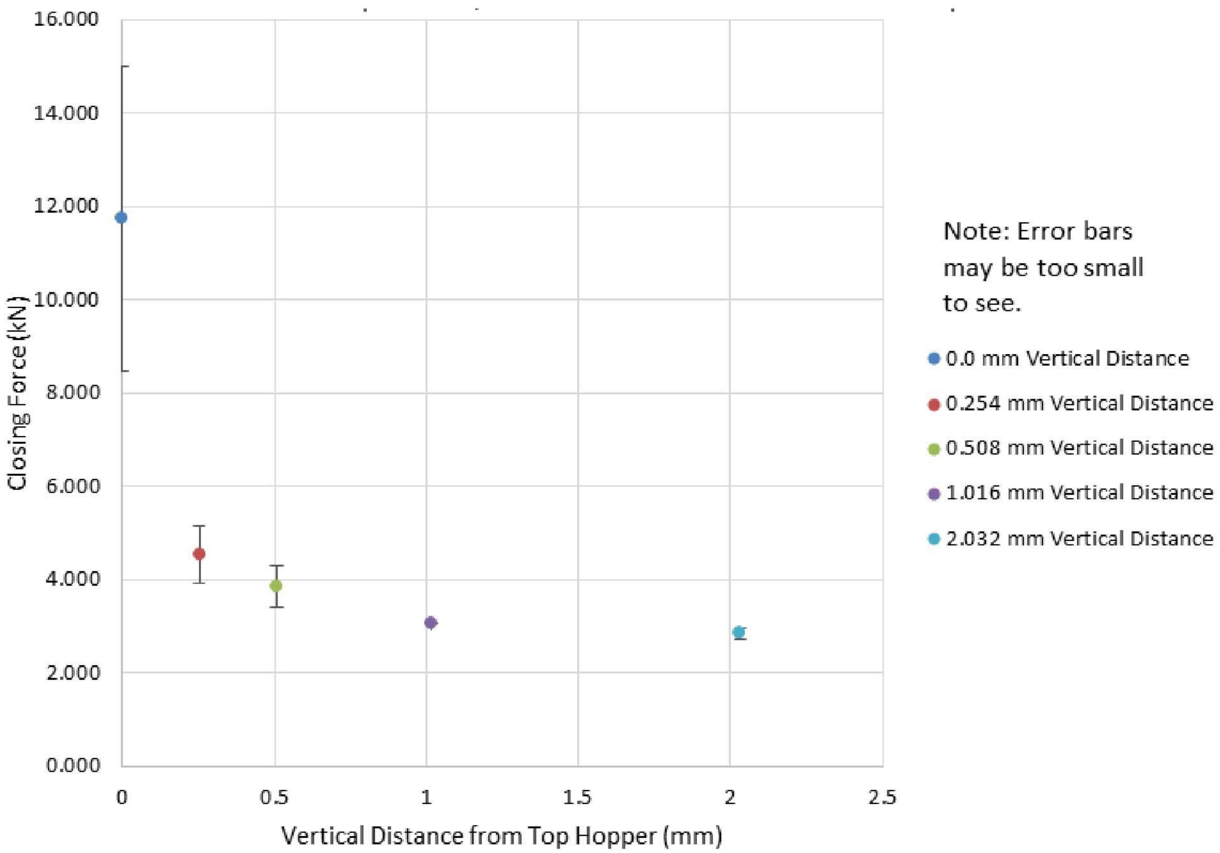

Figure 26. Measured hydraulic closing force vs slide gate vertical distance from top hopper.

Figure 27 shows the gate set at 2.032 mm (~7.3 average particle diameters) from the top hopper. Particles are visible between the gate and the top hopper. Particles were never seen to be spilling out of the sides of the gate assembly at this distance.

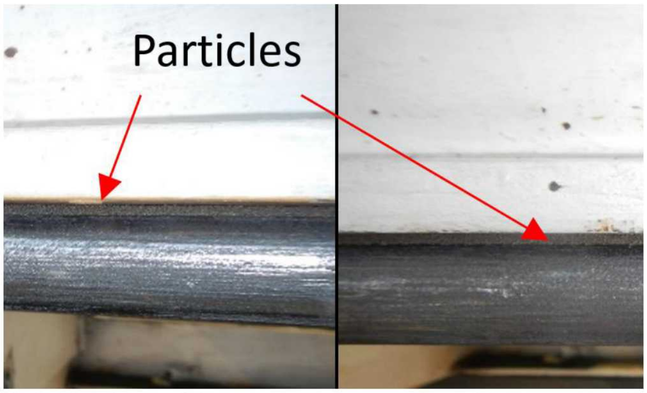

Figure 27. Close up view of particle layer above the slide gate at 2.032 mm separation distance.

3.1.1.3. Required Plate Location to Stop Particle Flow

The previous section determined that a minimum separation distance of 1 mm between the slide gate and top hopper was required due to force limitations. Fortunately, particles do not behave like liquids and will not necessarily flow through a vertical opening depending on the angle of repose. The particles have been shown to have an angle of repose of ~30°; below this, they will not flow solely under gravitational force. To ensure there is no unintended spillage of the particles, the gate edge must be placed a distance sufficiently beyond the aperture of the top hopper such that the resting angle of the particles is 30° or less. Figure 28 shows the variables used to determine this location. As long as the plate extends beyond ~1.7*h* from the edge of the aperture, the particles should not spill over the edge. A general rule of thumb would be to position the plate at least several times the height, *h*, past the edge of the aperture.

$$x \geq \frac{h}{\tan(\theta)} \geq 1.7h \tag{5}$$

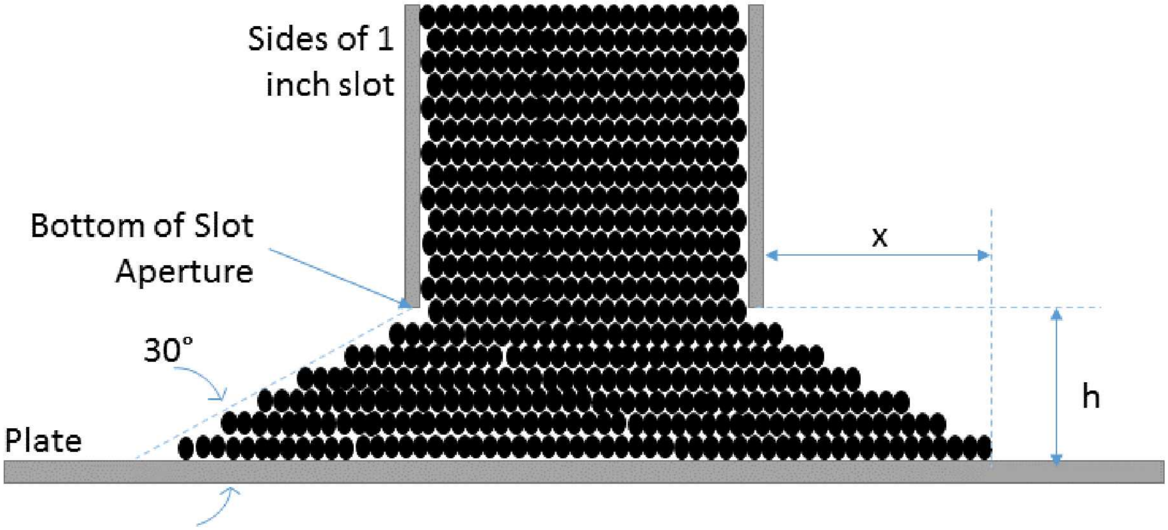

Figure 28. Diagram of slide gate dimensions.

3.1.1.4. System Description and Assembly

A slide gate was built to operate at 750°C using primarily 304 stainless steel. The slide gate was mounted below the top hopper using fixed supports. The aperture in the top hopper was a rectangular slot 1” x 44” cut into RSLE board; this slot size correlates with the maximum mass flow rate of ~10 kg/s. Rulon 641 (a high-temperature PTFE material similar to Teflon) was used to reduce friction between the fixed supports and the slide gate. The slide gate is actuated using an electromechanical system with a movement resolution less than 0.5 mm.

The mass flow control system for falling particle receivers must be capable of sub-millimeter movement to be able to incrementally adjust the mass flow rate, as well as fast movement to be able to quickly shut off flow if needed. The control system needed to have a resolution less than 1 mm and be able to move the slide gate 25.4 mm within 1 second (from rest). An incremental change in slot aperture width of 1 mm will change the particle mass flow rate by 1 – 2 kg/s per meter of slot length according to the modified Beverloo eq (validated by tests by Ho et al. 2017 [8]) at total desired particle mass flow rates of 10 – 20 kg/s/m, which will be necessary for a ~10 MW_e system with 6 m aperture and a 10 m long particle release length. Controlling the particle flow rate to within 1 – 2 kg/s per meter of slot length (or 10 – 20 kg/s for a 10 m wide particle release length) would enable a particle-outlet temperature control to within ~20 – 25 °C, which is within our desired particle outlet temperature range of 750 – 775 °C for supercritical carbon-dioxide Brayton cycles.

To meet these requirements, the control system used a single 304 stainless steel slide gate actuated by a Parker-Hannifin HMRS-18 screw-driven, rodless linear actuator with home and limit sensors. The motor for the actuator table is a Parker-Hannifin MPP1003 servo motor producing 17.16 N-m peak torque. Connected to the motor is a PS90 3:1 gear box. The motor is connected to the computer via an IPA 15 servo drive controller. The system components must be kept below 75°C to prevent failure; therefore, the actuator system must be kept a safe distance from the heated particles. The system has a theoretical translational resolution of 1.25 µm and fits the design criteria of a linear displacement of 25.4 mm within 1 second (from rest). Table 10 shows the electromechanical system components.

Table 10. Components of the slide gate control system [18].

Part Number	Image	Description
HMRS18S100-0250-0D100G1M2		Linear Actuator with cover • 10 mm screw lead • 250 mm stroke • Home and Limit Sensors
MPP1003D1E		Servo Motor • 17.16 N-m peak torque • Minimum output movement to linear actuator of 1.25 microns
PS90 3:1		Gearbox • 76 N-m nominal output • Backlash < 0.0192 mm

Part Number	Image	Description
IPA 15-HC		Servo Drive Controller • Ethernet TCP/IP • 6.3 A output • 120 VAC input
LabVIEW Program	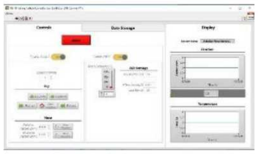	• Simulated Temperature or Thermocouple input response • Manual control

The actuator is connected to the slide gate using a set of "extender arms." These arms rest on pieces of Rulon 641which are on a system of overlapping angle irons. The angle irons are bolted to fixed supports that are connected to the top hopper. The bolts can be removed to slide the angle iron out and replace the Rulon 641, as needed. This system design has a minimum of moving parts and a low clearance to fit into the existing on-sun particle receiver at the NSTTF. Figure 29 shows the actuator and support system, and Figure 30 shows the assembled system that was commissioned off-sun in the high bay at the NSTTF.

Control of the actuator was accomplished using a custom built LabView program. The actuator's acceleration, deceleration, max velocity, jerk, maximum torque, data readout rate, actuator position soft limits, relative motion, and absolute motion could be set within the program. Position, actual torque, actual velocity, and actual acceleration were read out from the servo motor using command lines. Temperatures were read into the control system via thermocouples or were simulated within the program to easily model changes to the incoming flux. Position and temperature data were recorded and read out to a .csv file.

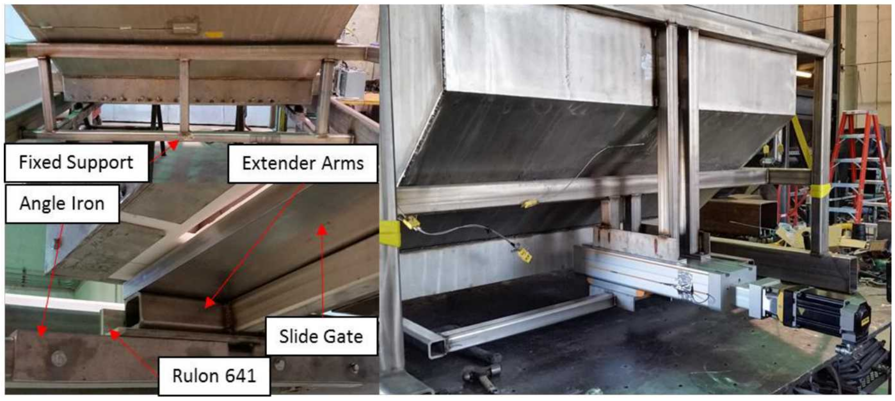

Figure 29. The electromechanical actuator attached to the slide gate. Left Top: Fixed supports on which carry the extender arms and slide gate. Left Bottom: Slide gate resting on the Rulon 641 which is bolted to the overlapping angle irons. Right: Linear actuator connected to the top hopper and extender arms.


Figure 30. Control system and top hopper being tested under ambient conditions.

The LabVIEW control program responds to both manual inputs and a simulated or real temperature signal. Movement inputs can be as low as 0.001 mm, though the minimum theoretical resolution of the system is 0.00125 mm. Friction and material strain make the resolvable movement larger.

When the system is set to respond to a temperature signal, the user must prescribe a desired setpoint for the particle outlet temperature. Additionally, the user may change the distance the gate is moved per iteration (speed). At prescribed sampling rates, the program reads the particle temperature and moves the gate the distance prescribed by Eq. (6). The direct proportional control C can be any value set by the user; initial tests have used a value of 0.01 mm/°C.

$$D = \left(T_{setpoint} - T_{particle}\right) * C \tag{6}$$

$Where:$
$D = Slide\ Gate\ Movement\ (mm)$
$T_{setpoint} = Desired\ Particle\ Temperature\ (°C)$
$T_{particle} = Particle\ Temperature\ (°C)$
$C = Direct\ Proportional\ Control\ \left(\frac{mm}{°C}\right)$

The value of C can be estimated using an energy balance for particle heating that correlates particle temperature rise with particle mass flow rate. Calibrated equations for particle mass flow as a function of aperture (e.g., modified Beverloo equation) can be used to correlate the required mass flow rate with aperture opening. Thus, the relative aperture opening (displacement) can be correlated to the desired temperature change for more advanced PID methods of particle mass flow control.

3.1.2. Commissioning and Evaluation

A laser-based method was developed to determine the gate's leading edge movement and positioning during operation. A Leica Disto D8 (laser-based distance measuring device) was mounted onto a track system (Figure 31) to accurately determine the relative position of the slide gate. The red laser light focused on the leading edge of the slide gate as shown in Figure 31. The accuracy of the Disto was within 0.1 mm.

Figure 31. Measurement of the plate's leading edge using the Disto under ambient conditions. The red laser dot is visible on the leading edge of the plate.

Data was collected at each of the plate's endpoints and 4 other interior points that were 0.214 m apart. For comparison with tests performed with particles, only the data collected at the plate's endpoints were used for reporting. Tests were performed to validate the control system's repeatability at both millimeter and sub-millimeter scales with and without particles flowing.

Figure 32 shows the plate's measured displacement (via the Disto) versus the programmed displacement, without particles. The measured data without particles have a linear fit slope of 0.9996. Similarly, Figure 33 shows the plate edge displacement as measured by the Disto D8 against the programmed plate movement with particles. The measured data with particles have a linear fit slope of 1.0537.

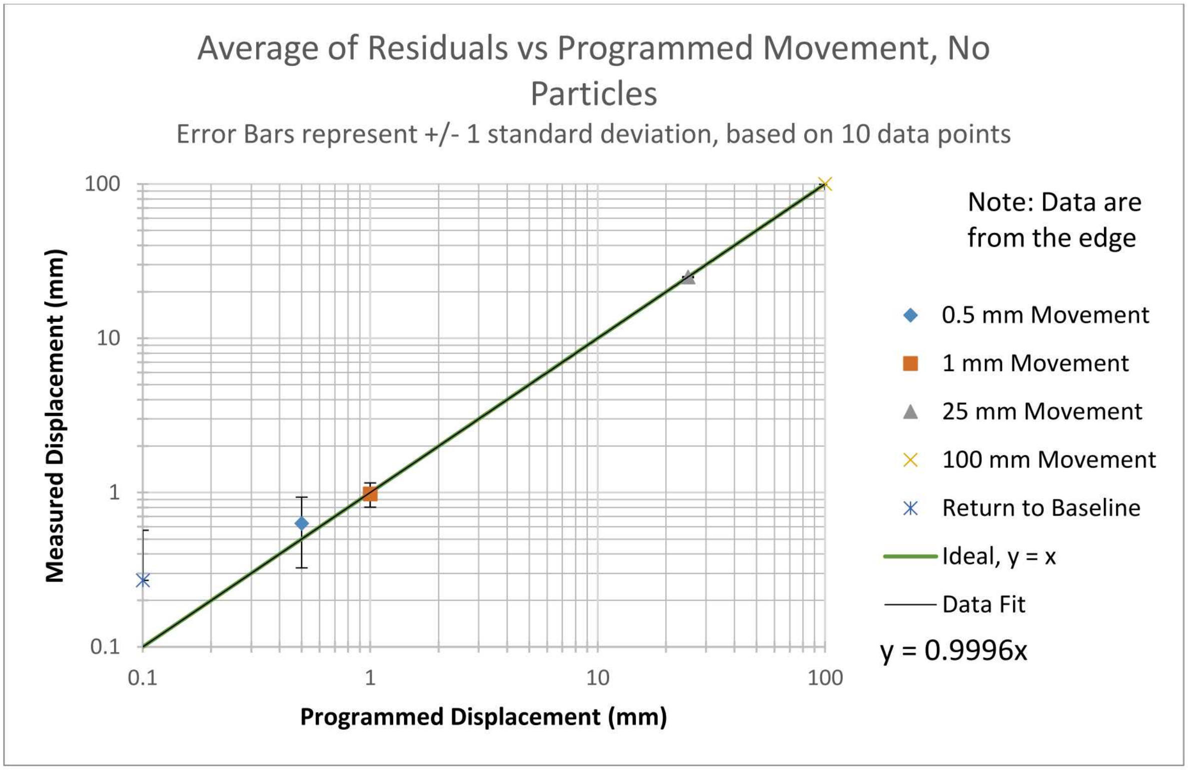

Figure 32. Measured vs. programmed displacements of the slide gate under ambient conditions, without particles.

A student's t-test was performed to determine the 95% confidence of the sample mean for each programmed displacement. The upper and lower bounds of the sample mean were compared to each of the prescribed (programmed) displacements. Results are shown in Table 11 for four prescribed displacements. Results show that the maximum difference between the measured and prescribed displacement was less than 1 mm in all cases and meets the performance evaluation criterion in Table 12.

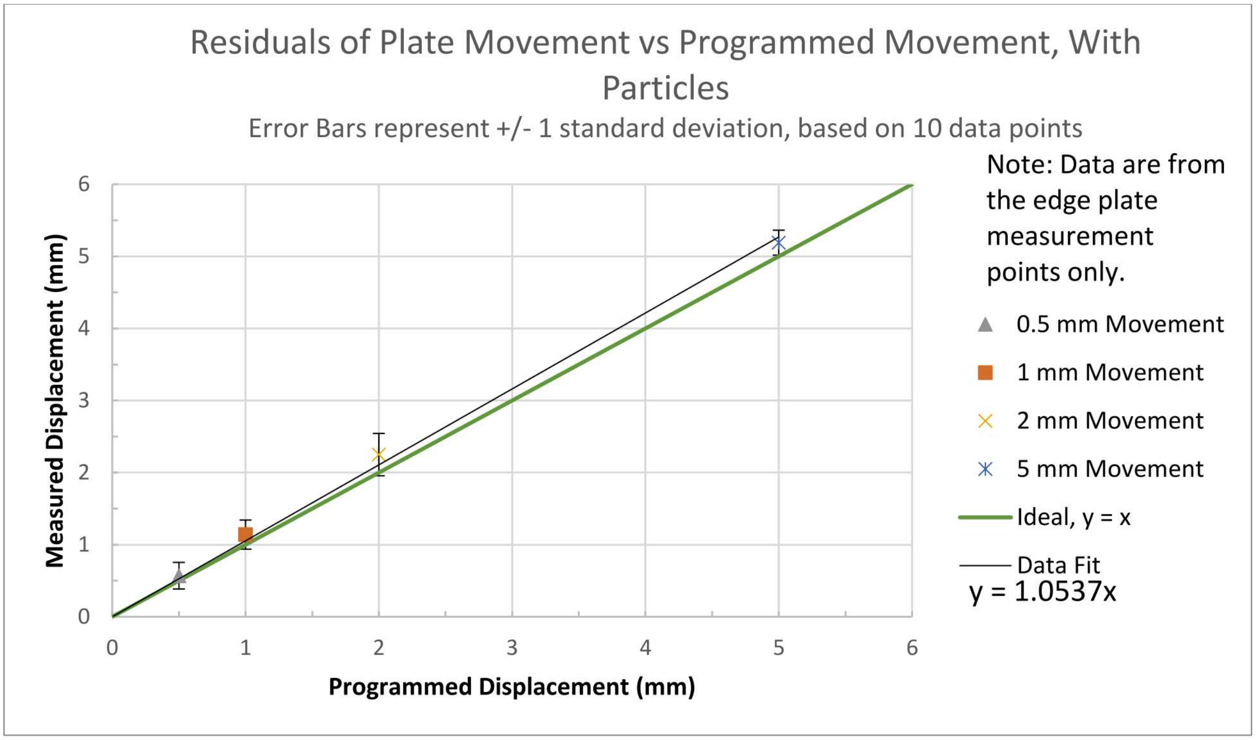

Figure 33. Measured vs. programmed displacements of the slide gate under ambient conditions, with particles.

Table 11. Difference in measured and prescribed displacements for different displacement values.

With Particles				
Programmed Displacement (mm)	**0.5**	**1**	**2**	**5**
$\lvert \mu_{max} - x_p \rvert$ (mm)	0.210	0.284	0.460	0.314
$\lvert \mu_{min} - x_p \rvert$ (mm)	0.0495	4.48E-03	4.48E-03	0.0659
Without Particles				
Programmed Displacement (mm)	**0.5**	**1.0**	**25**	**100**
$\lvert \mu_{max} - x_p \rvert$ (mm)	0.368	0.152	0.0459	0.183
$\lvert \mu_{min} - x_p \rvert$ (mm)	0.128	0.212	0.226	0.223

Table 12. Performance evaluation criterion for slide-gate resolution.

	Metric Definition (From Measurement)	*Success Value*	*Assessment Tool (Quality Assurance)*	*Goal Met (Y/N)*	*Supporting Data*
Project Evaluation Criteria 2.1.1	Incremental change in slot aperture width that can be resolved by control system	≤ 1 mm Constraint: With and without particle flow	Student's t-test using 95% confidence interval	Y	Table 11

3.1.3. Upscaling and Commercial Application

The slide-gate system developed in this work can be applied to large-scale systems by aligning multiple slide gates along the width of the discharge slot. For example, if the receiver aperture and particle curtain is ~10 m, then ten 1 m slide gates could be placed along the 10 m discharge slot. Each slide gate could be independently controlled to accommodate non-uniform irradiance patterns. In regions where the irradiance is higher, the particle mass flow rate can also be higher to more efficiently capture the incident radiation and better maintain a constant bulk particle outlet temperature. In regions where the irradiance is lower, the particle mass flow rate can be reduced. This is illustrated in Figure 34, which shows an example of a non-uniform irradiance distribution within a cavity receiver, and the corresponding slide gate openings to either increase or decrease the particle mass flow rate to maintain a consistent particle outlet temperature in each region. Non-uniform irradiance distributions occur due to spatial variations in heliostat field optical efficiency at different times of the day (e.g., in the morning, the heliostats to the west of the receiver will have greater optical efficiency than the heliostats to the east, yielding greater irradiance on the east side of an internal cavity receiver), different aiming strategies, sun shape, scattering, and concentrating optics.

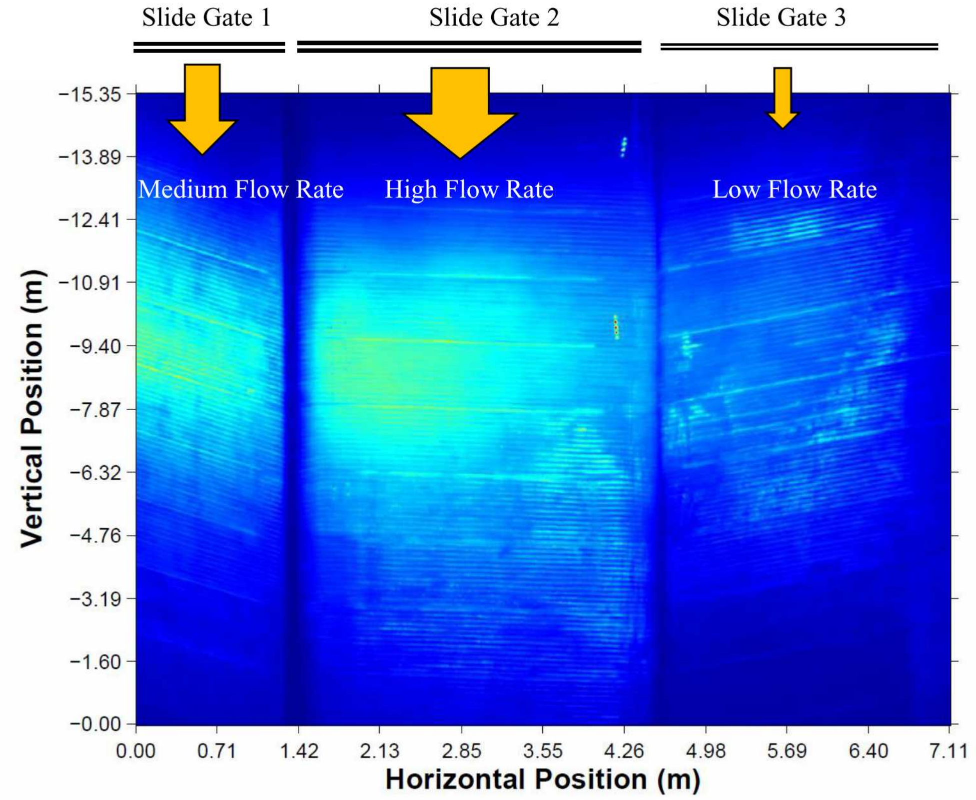

Figure 34. Illustration of non-uniform irradiance within a cavity receiver and the use of multiple slide gates to independently control the particle mass flow rates to yield consistent particle outlet temperatures in each region.

3.2. Particle Mass-Flow Measurement

The objective of the particle mass-flow measurement task is to develop a method to accurately measure the particle mass flow during system operation. Previous studies showed that the particle mass flow from pre-machined plates with a prescribed slot aperture was uncertain due to thermal expansion and plastic deformation of the plates (and resulting aperture size). Although the measurement of particle mass flow rate is not necessary to maintain a desired particle outlet temperature when an automated mass-flow control system is employed, the ability to measure the particle mass flow rate during on-sun operation will enable more accurate estimates of the receiver thermal efficiency.

3.2.1. Methods

A survey of particle mass-flow measurement methods was performed for this project. Particulate measurement devices that are commercially available fall into four broad categories: (1) impact plates, (2) centripetal force, (3) gravimetric, and (4) microwave sensors.

3.2.1.1. Impact plates

Impact plates determine the particulate mass flow rate by measuring the horizontal component of the impact force imparted to a plate using a load cell placed behind the plate. The flow rate is determined through calibrations at various known flow rates. Figure 35 shows an example of an impact plate.

Pros

- Simple mechanism
- Relatively inexpensive
- ± 0.5% to 5% full scale accuracy (depending on cost) when supplied with a consistent flowrate
- High flow rate capability

Cons

- Requires a large amount of space
- Accuracy decreases if the mass flow rate is not consistent over short time intervals
- Temperature ratings are less than $300°C$ after the addition of cooling systems

3.2.1.2. Centripetal force

Particulate flows vertically onto the curved chute. The force imparted to the chute as the mass flow changes direction from vertical to horizontal is measured using load cells and is then equated to a mass flow rate. Figure 35 shows an example of a centripetal flow device.

Pros

- Simple mechanism
- Relatively inexpensive
- ± 0.25% to 2% full scale accuracy (depending on cost) when supplied with a consistent flowrate
- High flow rate capability

Cons

- Requires a large amount of space
- The mass must be placed onto the correct portion of the chute to make the product slide on the surface rather than impact on it
- Temperature ratings are less than $300°C$ after the addition of cooling systems

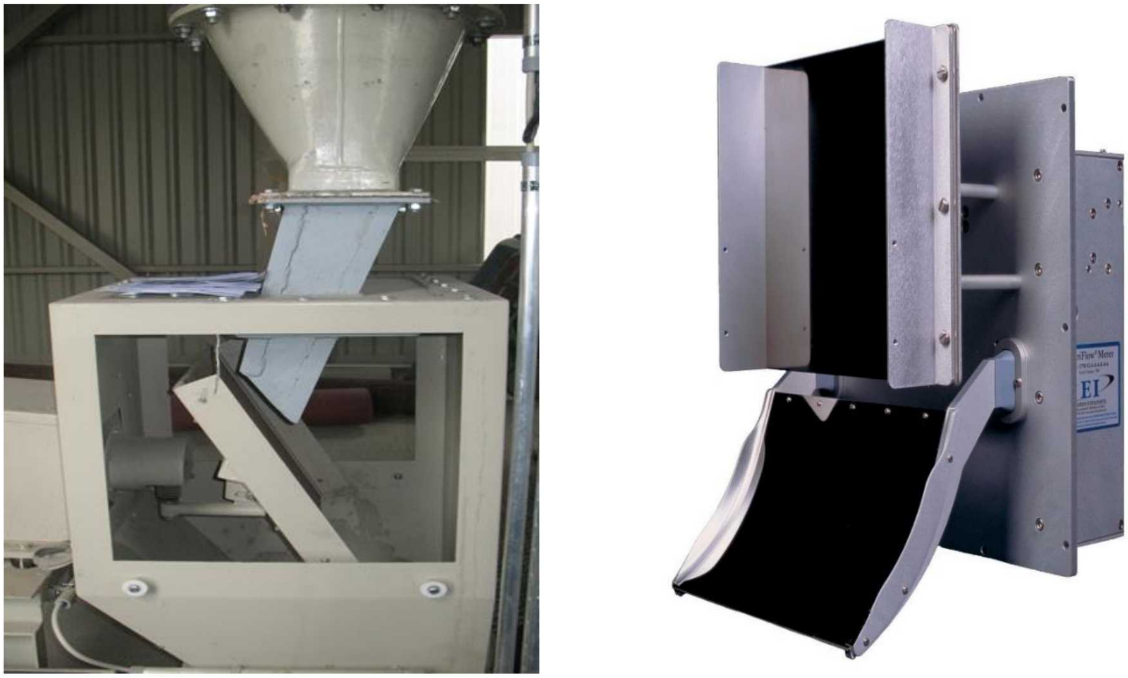

Figure 35. Examples of an impact plate (left) and centripetal force (right) measurement devices.

3.2.1.3. Gravimetric

Particulate flows into a catchment basin where it is weighed over a prescribed time interval. The mass accumulated divided by the time interval yields the mass flow rate. The basin is supported from below by three or four load cells that are summed together to provide a single weight output. The mass flow rate of the particulate is determined in post-processing by dividing the change in weight by the accumulation time. Figure 36 shows an example of a strain gage load cell.

Pros

- Simple mechanism
- Relatively inexpensive
- ± 0.03% to 0.25% full scale accuracy (depending on cost)
- The load cells can be positioned arbitrarily far from the heat source and/or insulated

Cons

- Requires a large amount of space for the catchment basin
- Measurements can only be taken in batches so real-time flow rates are not possible
- The entirety of the particulate flow must be diverted to the catchment basin and returned to the main particulate loop after measurement

3.2.1.4. Microwave Sensor

The sensor emits microwaves at a known amplitude and frequency. The microwave characteristics are altered by their interaction with the moving mass. The change in the wave amplitude and frequency is detected by the sensor and equated to a mass flow rate after calibrations at known flow rates. Figure 36 shows an example of a microwave sensor.

Pros

- Does not directly interact with the mass flow
- Able to fit within tight spaces
- Capable of 1000°C with cooling accessory
- ±2% accuracy
- Multiple calibration points reduce the error
- Static particulates are ignored

Cons

- High cost
- Single source manufacturer for a sensor with a cooling system
- Extremely sensitive to changes in the mass flow's streamlines

Figure 36. Example of a strain-gage load cell (left) and microwave sensor (right).

The selected measurement device had to operate with a product temperature of nearly 800 °C. In addition, the device had to provide real-time mass flow rate measurements. Due to these constraints, the microwave sensor with a cooling jacket was selected for use as an in-situ sensor, and the gravimetric method was selected as a reference.

3.2.2. Commissioning and Evaluation

3.2.2.1. In-Situ Weigh Hopper

An in-situ weigh hopper was used to evaluate the particle mass flow rate past the slide gate described in Section 3.1 for different aperture openings. In this method, the weigh hopper was placed below the top hopper, and the slide gate was opened a fixed distance allowing the particles to fall into the weigh hopper. The slide gate was closed, and the weigh hopper was removed and weighed using a suspended Dillon Dynamometer. From a reference zero point, fixed-aperture mass flow measurements were made for aperture openings of 5, 6, 7.5, 10, and 12 mm. All measurements were made for approximately 60 seconds. In addition, dynamic-aperture mass flow measurements were made for apertures of 5 mm for approximately 30 seconds followed by 5.5 mm for approximately 30 seconds. This was repeated for apertures of 5 mm and 6 mm, each for approximately 30 seconds. All measurements were repeated three times. Results of the fixed-aperture mass flow measurements are shown in Figure 37, together with predictions from the modified Beverloo model [8] using optimized fitting parameters of 38.8 and 8.9 for C_1 and C_2, respectively. The values for the fitting parameters changed from previous tests using a fixed slot (C_1=62 and C_2=1.4) since the flow pattern of particles flowing around the slide gate was different than particles falling straight through a slot aperture.

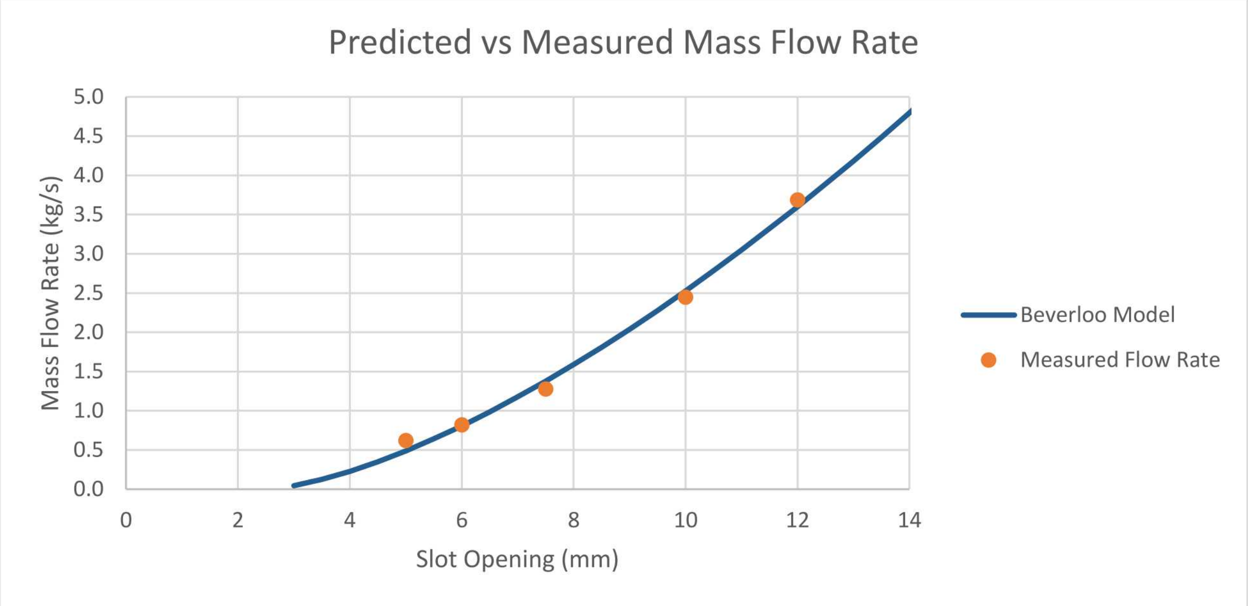

Figure 37. Measured and predicted mass flow rates as a function of slot opening created by the slide gate under ambient conditions..

The total mass flow of the dynamic-aperture tests was measured using the weigh hopper and compared to the predicted mass flow obtained from the fixed-aperture tests and the duration of the flow at each aperture. The purpose was to determine if the particle mass flow could be accurately controlled during dynamic movement of the slide gate (rather than at a fixed position). Results showed that the relative error between the measured dynamic-aperture mass flow and predicted mass flow using the fixed-aperture results was within the propagated measurement error (2 – 3%). The propagated error consisted of the relative error in both the mass flow rate (1 – 2%) and the duration of flow at each fixed aperture (1 – 2%). The mass flow measurements obtained using the weigh hopper show the electromechanical control system is accurate and repeatable at sub-millimeter resolutions.

This was repeated three times each for aperture openings of 5, 6, 7.5, 10, and 12 mm. Student's t-test with 95% confidence was applied to each sample set to ensure each aperture mass flow rate average was statistically distinct (see Table 13 and Figure 38). The difference between the particle mass flow rates of different successive aperture openings was calculated and shown in Table 14.

Table 13. Student's t-test of mass flow rates with 95% confidence.

Aperture (mm)	$\bar{\dot{m}}$ (kg/s)	t=0.025 (95% Confidence)	SE ($\bar{\dot{m}}$)	μ (kg/s)
5	0.618	4.303	5.74E-03	0.618±0.025
6	0.817	4.303	4.64E-03	0.817±0.020
7.5	1.275	4.303	4.64E-03	1.275±0.020
10	2.445	4.303	8.81E-03	2.445±0.038
12	3.684	4.303	3.47E-03	3.684±0.015

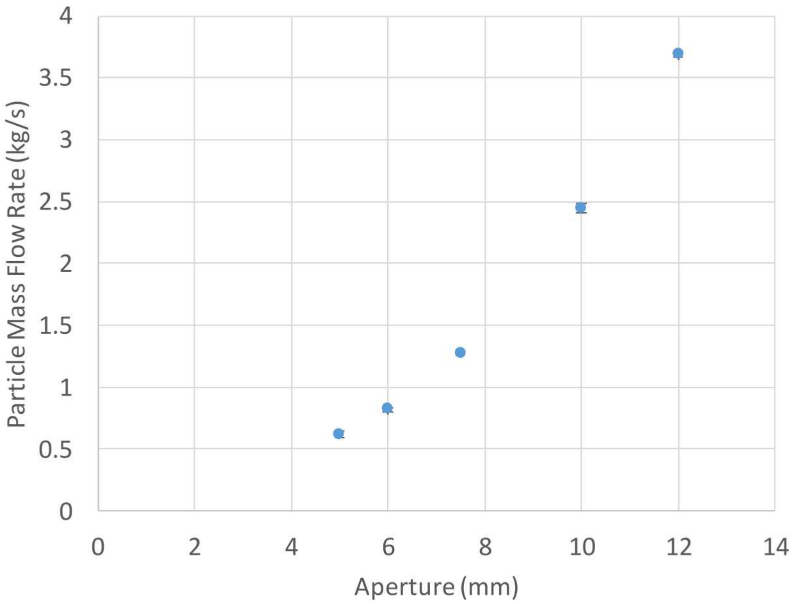

Figure 38. Measured particle mass flow rate vs. aperture under ambient conditions. Vertical error bars (difficult to see) represent 95% confidence interval about the mean using Student's t-test.

Table 14. Measured mass flow rate differences of two consecutive slide-gate movements.

Aperture Change	Mass Flow Rate Difference (kg/s)
5 mm – 6 mm	0.199
6 – 7.5 mm	0.458
7.5 – 10 mm	1.17
10 – 12 mm	1.239

The time required for the slide gate to traverse from one aperture value to another was also evaluated. Commercial implementation of falling particle technologies will need to cope with solar flux perturbations (i.e., cloud transients) while maintaining a constant particle outlet temperature. To account for this, the control system program was modified to respond to a simulated flux perturbation by increasing or decreasing the slot aperture as determined by a heat balance combined with the modified Beverloo model. The flux perturbation is accounted for as:

$$Q_{old} = \dot{m}_{old} c_p \Delta T$$
$$Q_{new} = (1 - Perturbation\ Percent) * Q_{old}$$

The mass flow rate as a function of the new flux with a constant temperature change is then:

$$\dot{m}_{new} = \frac{Q_{new}}{c_p \Delta T}$$

Using the modified Beverloo model, the new mass flow rate (as a function of the new flux) can be related to the slot aperture as:

$$\dot{m}_{new} = \frac{C_1 \rho \sqrt{g} (\mathrm{D} - C_2 d)^{\frac{3}{2}} L}{60}$$
$$\frac{Q_{new}}{c_p \Delta T} = \frac{C_1 \rho \sqrt{g} (\mathrm{D} - C_2 d)^{\frac{3}{2}} L}{60}$$

Rearranging and solving for the new slot aperture opening (D):

$$\mathrm{D} = \left(\frac{60 * Q_{new}}{C_1 \rho \sqrt{g} c_p \Delta T} \right)^{\frac{2}{3}} + C_2 d$$

Tests were run with simulated flux perturbations of 25, 50, and 75% of an initial flux of 1000 suns, as shown in Table 15. These tests show that the control system will be able to adjust the slot aperture to any desired position in less than ~1.0 seconds.

Table 15. Measured aperture recovery times to achieve a prescribed slide-gate position to account for simulated flux perturbations.

Test	Initial Flux (Suns)	New Flux (Suns)	Aperture Adjustment (mm)	Recovery Time(s)	Average (s)	Sample Standard Deviation (s)
1.1.1	1000	750	2.644	0.55	0.55	2.03E-02
1.1.2	750	1000	-2.642	0.51		
1.2.1	1000	750	2.643	0.55		
1.2.2	750	1000	-2.642	0.56		
1.3.1	1000	750	2.644	0.57		
1.3.2	750	1000	-2.643	0.54		
2.1.1	1000	500	5.806	0.80	0.79	2.44E-02
2.1.2	500	1000	-5.804	0.77		
2.2.1	1000	500	5.806	0.79		
2.2.2	500	1000	-5.806	0.83		
2.3.1	1000	500	5.806	0.76		
2.3.2	500	1000	-5.806	0.78		
3.1.1	1000	250	9.564	1.00	0.98	9.20E-03
3.1.2	250	1000	-9.563	0.99		
3.2.1	1000	250	9.565	0.97		
3.2.2	250	1000	-9.564	0.98		
3.3.1	1000	250	9.562	0.97		
3.3.2	250	1000	-9.562	0.99		

Table 16. Performance evaluation criteria for mass-flow control and recovery time.

	Metric Definition (From Measurement)	***Success Value***	***Assessment Tool (Quality Assurance)***	***Goal Met (Y/N)***	***Supporting Data***
P.E.C. 2.2.2	Mass flow rates of two consecutive aperture openings	$\lvert\dot{m}_n - \dot{m}_{n+1}\rvert < 2.0$ **kg/s** Sample means of mass flow rates at two consecutive apertures are statistically different	Student’s t-test with 95% confidence Prescribe sampling time (number of measurements) needed for statistically significant distinction	Y	Table 13

PEC 2.2.3	Recovery time (t) Time for aperture adjustment and measured mass flow steady state for a given set point temperature following simulated flux perturbation of 25-75%.	$t < 1$ minute Constraint: at least 3 repeat measurements at each of 3 simulated flux perturbations	Function: relationship describing recovery time with appropriate dependent variables and uncertainties	Y	Table 15

For on-sun operation, the weigh hopper could either be suspended and weighed using a dynamometer (as implemented for the slide gate characterization) or constructed to rest on load cells. It was determined that suspending the weigh hopper while on top of the solar tower presented challenges with weather proofing and preventing excessive movement during windy conditions. Therefore, a load cell system was purchased from Omega which includes four cantilever-type tank-weighing load cells.

The cells provide self-leveling and self-adjusting for thermal expansion and are composed of weather resistant materials such as nickel plated carbon steel and stainless steel. The mass weighing hopper is supported with a load cell at each of its four bottom corners (Figure 39). The four load cells are then connected to a summing box which takes the input from the four sensors and combines them into a single force signal. The sensor works by providing a change in voltage from a strain gauge which can then be correlated through a linear relationship with applied load. The system is capable of measuring a load of 3000 lb_f (~1,400 kg) over the four supported points and was designed to withstand wind loads up to 96 mph on top of the tower. This system was placed on a platform that is ~2.1 m above the deck, the same location where we anticipate a particle-to-supercritical CO_2 heat exchanger will be incorporated into the system. The overall dimensions of the heat exchanger are known such that the ductwork from the mass flow hopper can be used again with the heat exchanger. The ducting from the weigh hopper to the bucket elevator used slip-fit ducting joints to prevent the hopper from being artificially supported by the ducting or adjacent components, which would interfere with the load cell measurements.

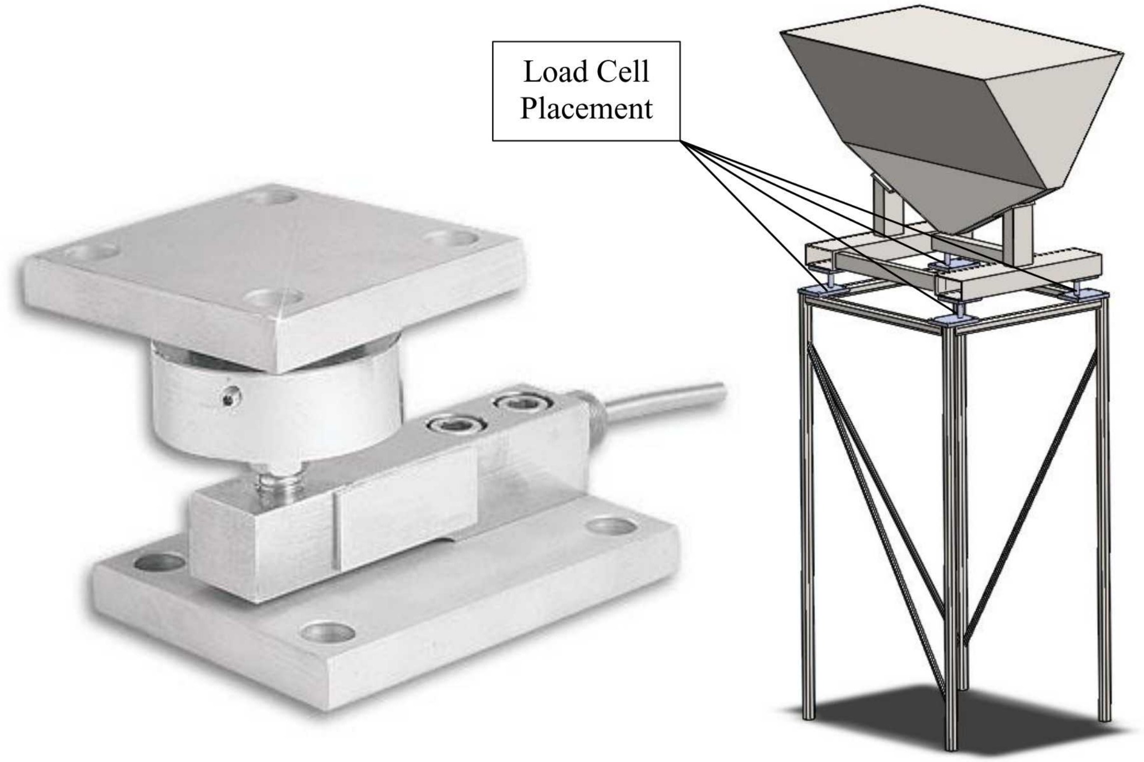

Figure 39. (Left) Cantilever load cell (Omega Engineering TWA5) for mass flow measurement; (Right) SolidWorks depiction of the mass flow rate sensors and hopper

3.2.2.2. In-Situ Microwave Sensor

The Solidflow 2.0 microwave sensor was used to measure the mass flow rate of particles flowing through the falling particle receiver. It was placed in the ducting between the diverter valve and the load cell assembly, allowing the Solidflow readings to take place concurrently with the load cell readings (see Figure 40)

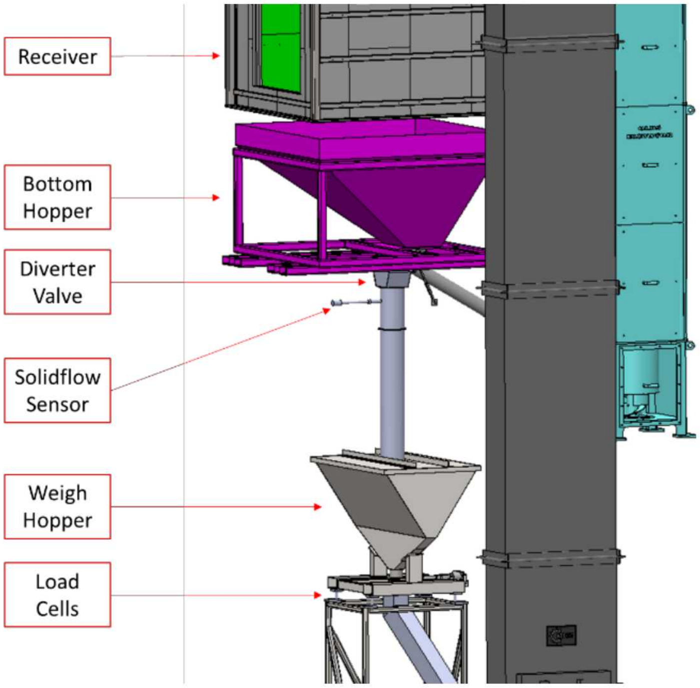

Figure 40. Placement of the Solidflow sensor in the falling particle system.

A representative of the sensor's distributer (GTS-SWR) was brought on site to assist in calibration of the system. The manufacturer's website claims the sensor can measure up to 5 kg/s, but the technician clarified that the maximum value is dependent on the density of the material being measured. With the high density of the particles, the technician was not confident the sensor would be able to measure accurately beyond 3 kg/s.

After examining the sensor's location in the falling particle receiver system, the technician advised adding baffles to help concentrate the particle flow as it fell past the sensor. One of these baffles is shown in Figure 41; a second baffle was added below the one shown but oriented in the opposite direction. This configuration shielded the sensor from direct contact with the particles but allowed it to still "see" the flow in a concentrated form.

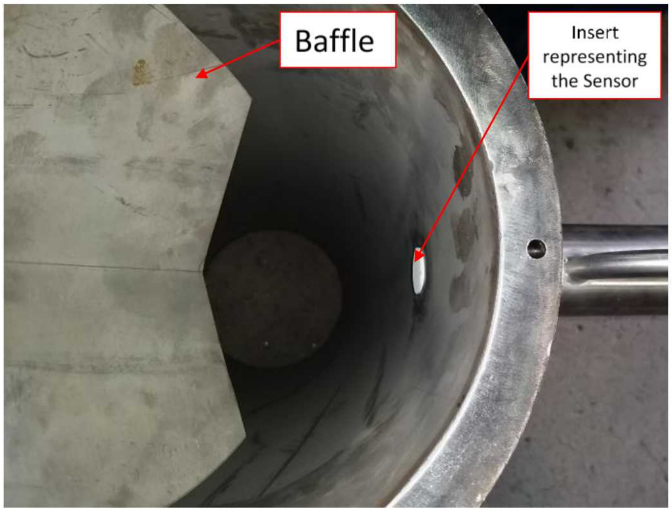

Figure 41. Baffle to concentrate particle flow past the sensor. Not shown is an additional baffle oriented in the opposite direction.

After adding the baffles, the sensor was tested at ambient temperature with known flow rates. The results of the testing were not immediately consistent; the sensor reading would stabilize around a value for a given flow rate, but would not be able to repeat that value after the flow rate was perturbed and then returned to the previous flow rate.

The pipe, sensor, and baffles were then rotated 120 degrees so that the sensor saw the particle flow from the side. This position yielded more consistent results than when the sensor was directly in-line with the particle flow. The sensor was calibrated at five points corresponding to known particle flow rates at ambient temperatures (see Table 17). These events took place on November 7-8, 2017.

Table 17. Calibration points and measured flow rates of the Solidflow Sensor.

Point	Mass Flow Rate $\left(\frac{kg}{s}\right)$
1	0
2	0.76
3	1.77
4	3.24
5	3.67

Figure 42 shows the results of testing the sensor at ambient and $300°C$ outlet temperatures. The Solidflow sensor was calibrated at ambient temperatures. Following calibration, the sensor was reading accurately at the values for which it was calibrated. When the receiver system was raised to the top of the tower and the sensor was tested at ambient and $300°C$, the sensor failed to read accurately at any flow rate or temperature. The results show that the sensor readings are inversely correlated to the mass flow readings from the load cells; if the sensor was reading accurately, it would be positively correlated (y = x) with the load cells.

The causes for the sensor's inaccurate readings during tower-top testing versus calibration are unknown. Potential causes are:

- Electromagnetic fields that are generated by the build-up of static electricity as the particles interact with metal surfaces near the sensor after prolonged particle mass flow
- Sensor damage due to radiative heat from surrounding hot bodies

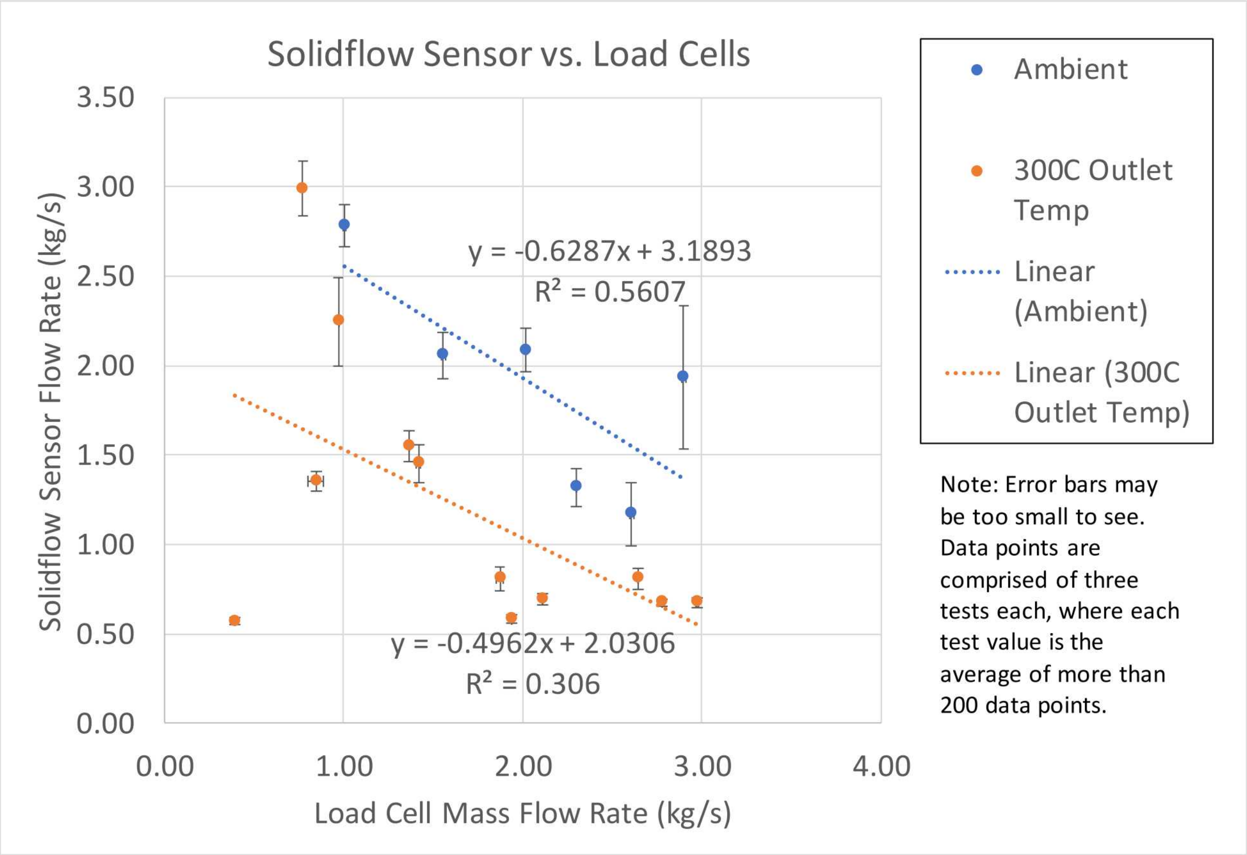

Figure 42. Measured mass flow rates at ambient and 300°C using the Solidflow sensor vs. load cells. Accurate readings by the Solidflow Sensor would be a linear line y = x.

PEC 2.2.1 (Table 18) required a linear fit line with an R^2 value greater than 0.95 and a slope between 0.975 and 1.025. Neither of these metrics was met by the Solidflow sensor, as displayed in Figure 42. Future testing with alternative in-situ mass flow measurement methods is required if a portable instrument is needed. Our recommendation is to use the more accurate and reliable weigh-hopper method in between key components of the particle receiver system, such as in between the receiver and the hot storage tank and in between the particle heat exchanger and the bottom storage tank.

Table 18. Performance Evaluation Criterion for mass flow sensor.

	Metric Definition (From Measurement)	*Success Value*	*Assessment Tool (Quality Assurance)*	*Goal Met (Y/N)*	*Supporting Data*
Project Evaluation Criteria 2.2.1	Measured particle mass flow rate, ṁ, using alternative *in situ* methods vs. weigh hopper method (most accurate but difficult to implement in situ) **AND** Measured *in-situ* particle mass flow rate vs predicted flow rate based on predictions as a function of aperture width	$R^2 > 0.95$ $0.975 \leq$ Slope ≤ 1.025 Standard deviation about the mean for each method is ≤ 1 kg/s Constraint: At least five different mass flow rates with at least three measurements at each rate	R^2 and slope of linear curve fit of in situ vs. weigh-hopper mass flow measurements	No	Figure 42

4. ON-SUN PERFORMANCE EVALUATION

4.1. System Modifications

On-sun tests of the particle receiver system with automated particle mass flow control and measurement were performed at the NSTTF in January and February of 2018. A significant number of modifications were made to the existing particle test loop to accommodate the mass flow control and measurement systems. Figure 43 shows a schematic of the modified particle test loop with the addition of a slide gate and linear actuator beneath the top hopper for particle mass-flow control, a weigh hopper to measure the particle mass flow in situ, and a bucket elevator capable of operating at 600 °C to carry particles from the exit of the weigh hopper to the base of the Olds (screw-type) elevator. In addition, ducting and a diverter valve were installed beneath the bottom hopper to enable particle flow to be diverted from the recirculation loop to the weigh hopper for mass flow measurements. At the base of the weigh hopper, a slide gate was installed to enable particles to be stored (for weighing) or diverted to the bucket elevator for recirculation. Additional details of the new components are provided below.

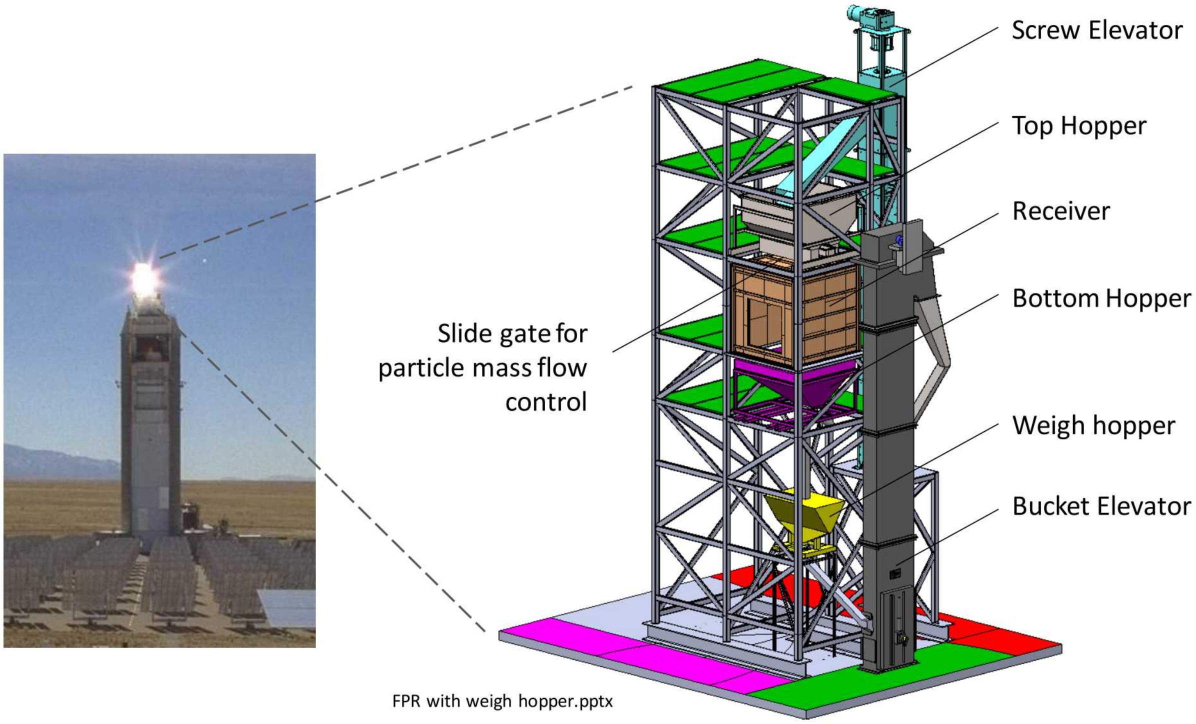

FPR with weigh hopper.pptx

Figure 43. Sandia's Particle Test Loop with modifications for on-sun testing with in-situ particle mass flow control and measurement capability.

4.1.1. Receiver Modifications

Figure 44 shows modifications to the top hopper. A liner with steep walls was inserted into the front section to ensure a more uniform mass flow of the particles. During previous tests, it was observed that the thermocouple readings along the height of the top hopper could be erratic, and we deduced that it was caused by "funnel flow" and periodic avalanching of stagnant particles along the sides of the shallow walls. The steeper walls produce a more uniform "mass flow" as the particles move downward through the top hopper [19], allowing for more consistent and stable thermocouple measurements. In addition, as described in Section 3.1, a slide gate and linear actuator were installed at the base of the top hopper to regulate the amount of particles flowing into the receiver. The position of the slide gate could be set to a prescribed aperture, or it could be automatically controlled using a closed-loop feedback system to maintain a prescribed setpoint particle-outlet temperature (see Section 4.3).

Figure 44. Left: Top hopper liner with steeper walls to enable more uniform particle mass flow along thermocouple tree. Right: Linear actuator mounted to the bottom of the top hopper to control the slide gate for particle mass flow control.

At the base of the receiver, the five thermocouple funnels were modified to enable faster throughput of the particles. The funnels were designed to have a large opening to catch particles in the presence of wind and air movement within the receiver, which could disrupt the particle curtain. The large opening of the funnel led to large transit times of the particles from the top of the funnel to the base of the funnel, which had a thermocouple in the middle of a small 1 cm x 1 cm opening that restricted the flow of particles. The restriction forced the particles to accumulate and immerse the thermocouple for accurate temperature measurements of the particles. However, with a large accumulation of particles in the funnel, it could take up to ~30 seconds for a particle at the top of the funnel to reach the thermocouple, allowing for potential cooling before the particle outlet temperatures was recorded. To remedy this, slots were cut into the vertical sides of the funnels just above the restriction to enable particles to be released. This design enabled particles to be captured from a large area (the top opening of the funnel) and accumulate around the thermocouple near the bottom restriction, but the transit time through the funnel was only a few seconds since most of the particles flowed out the sides above the restriction.

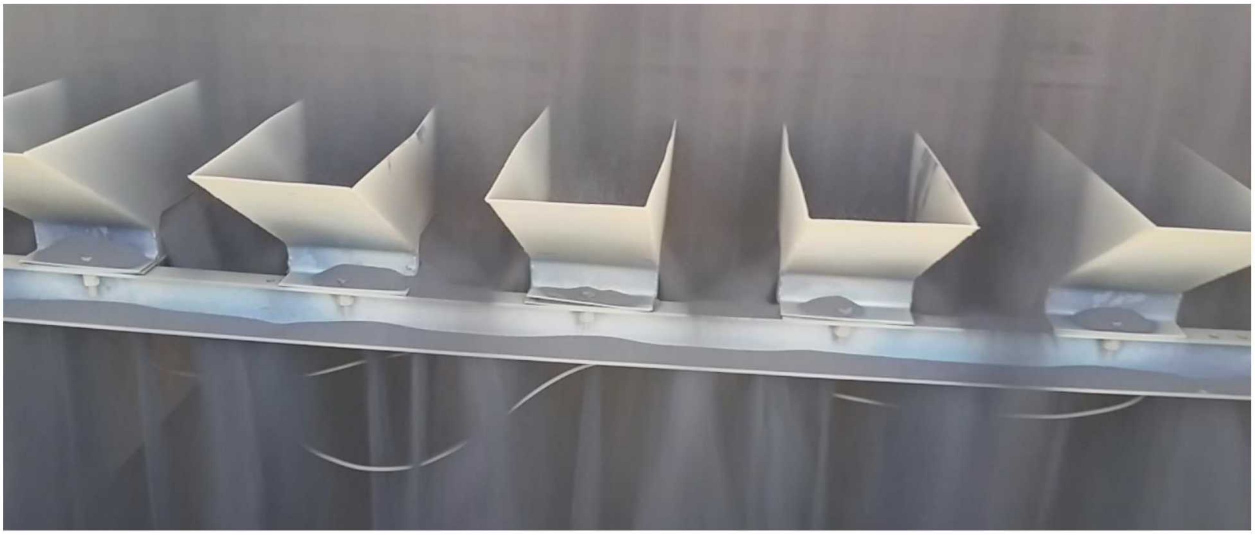

Figure 45. Thermocouple funnels at the base of the receiver to measure the particle outlet temperature.

4.1.2. Particle Mass-Flow Measurement System

Figure 46 shows the assembled particle mass-flow measurement system. A diverter valve was installed just beneath the bottom hopper to divert particles from the primary recirculation loop to the mass-flow measurement loop to obtain periodic mass-flow measurements. The mass-flow measurement loop consisted of the weigh hopper affixed to four load cells on a stand. A slide gate beneath the weigh hopper could be closed to accumulate particles in the weigh hopper for a prescribed duration (usually less than 30 seconds) to determine the particle mass flow rate. The mass accumulation in the weigh hopper was linear as a function time, leading to accurate and repeatable mass flow measurements. The slide gate was then opened to allow particles to flow into the new bucket elevator. The bucket elevator lifts the particles ~7 m (~23 feet) to the high-temperature Olds elevator with a particle mass flow capacity of up to ~6 kg/s at ~600 °C. The amount of particles flowing into the bucket elevator was restricted to less than 1 kg/s to reduce the heating of the ductwork to the bucket elevator. During several tests when the particles were hot (>600 °C), the duct between the weigh hopper and bucket elevator expanded and pushed up against the bottom of the slide gate and weigh hopper, causing negative mass readings. By reducing the mass flow, the thermal expansion of the duct was reduced and did not impede the weigh hopper measurements.

Another issue that was discovered at high particle mass flow rates (> ~10 kg/s). The Olds (screw) elevator in the primary recirculation loop has a maximum particle mass flow capacity of ~10 kg/s. When the slide gate was positioned to enable greater particle mass flow rates greater than ~10 kg/s, we observed that the weigh hopper would occasionally yield anomalously high particle mass flow rates (>25 kg/s). We postulated that at these high particle mass flow rates, particles were backing up from the duct to the Olds elevator and into the bottom hopper above the diverter valve. When the diverter valve was moved to allow particles to flow into the weight hopper, a slug of particles accumulated in the bottom hopper would flow into the weigh hopper, giving the anomalously high readings. To prevent this, we determined that mass flow readings using the weigh hopper should be performed immediately after the aperture is set to the high mass-flow rate position before any accumulation and back-up can occur.

Figure 46 also shows the location of the Solidflow microwave sensor. As particles were diverted to the weigh hopper, they passed by the Solidflow sensor for measurement. However, as described in Section 3.2.2.2, the Solidflow sensor yielded erratic and unreliable results after it was installed and calibrated. We are working with the distributor to diagnose the issues and possibly obtain a refund.

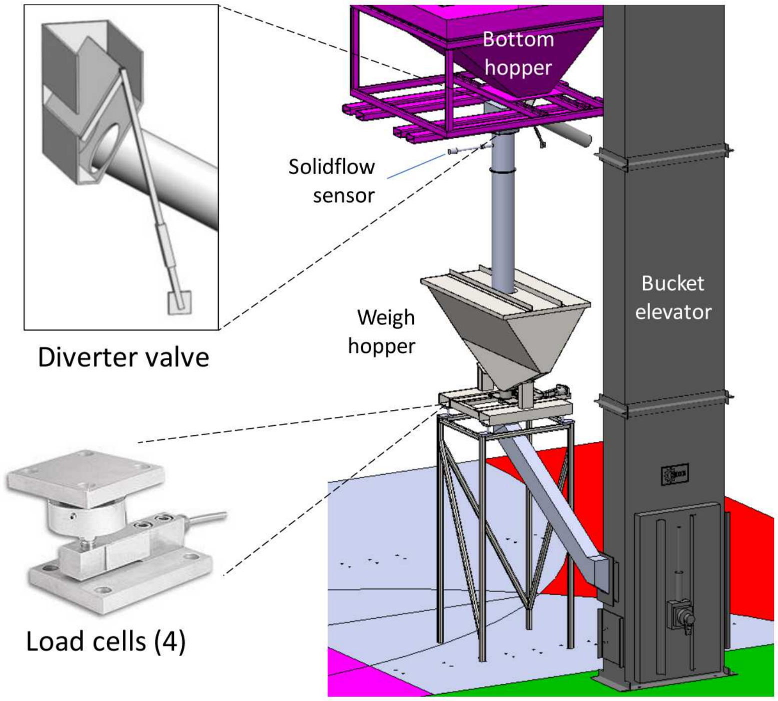

Figure 46. Assembled particle mass-flow measurement system.

Figure 47 shows the particle mass flow rate vs. aperture opening of the slide gate for two different particle inlet temperatures using the in-situ weigh hopper. The higher particle temperature results in a lower mass flow rate, which was expected due to increased particle/wall friction at higher temperatures (as verified by Jenike & Johanson). A modified Beverloo-Ho equation was developed to accommodate the effects of the slide gate and elevated temperatures (Eq. (7)). The constants and exponents in Eq. (7) were fit to available data at 10 °C and 300 °C.

Beverloo-Ho Equation:

$$W = \left[C_1 \rho_b \sqrt{g} \left(D - C_2 d \right)^{n+1/2} + C_3 D^x \right] \left(C_4 D \left(T_{amb} / T \right) \right)^y \quad (7)$$

where

W = particle mass flow rate (kg/min for 3D or kg/min/m for 2D)
C_1 = dimensionless constant related to material properties (38.8)

C_2 = geometrical factor accounting for the effective outpouring section being smaller than the aperture (8.9)
ρ_b = bulk density of the particles (2000 kg/m^3)
g = gravitational constant (9.81 m/s^2)
D = aperture size (m)
d = particle size (3.5e-4 m)
N = 1 for 2D or 2 for 3D
C_3 = factor to account for flow around the edge of the slide gate (0.012)
x = exponent to account for exponential growth as the slide gate opens (3.4)
C_4 = factor to account for elevated temperatures and greater particle/wall friction (0.002)
T_{amb} = reference temperature (283 K)
T = particle temperature (K)
y = exponent to account for elevated temperatures and greater particle/wall friction (0.4)

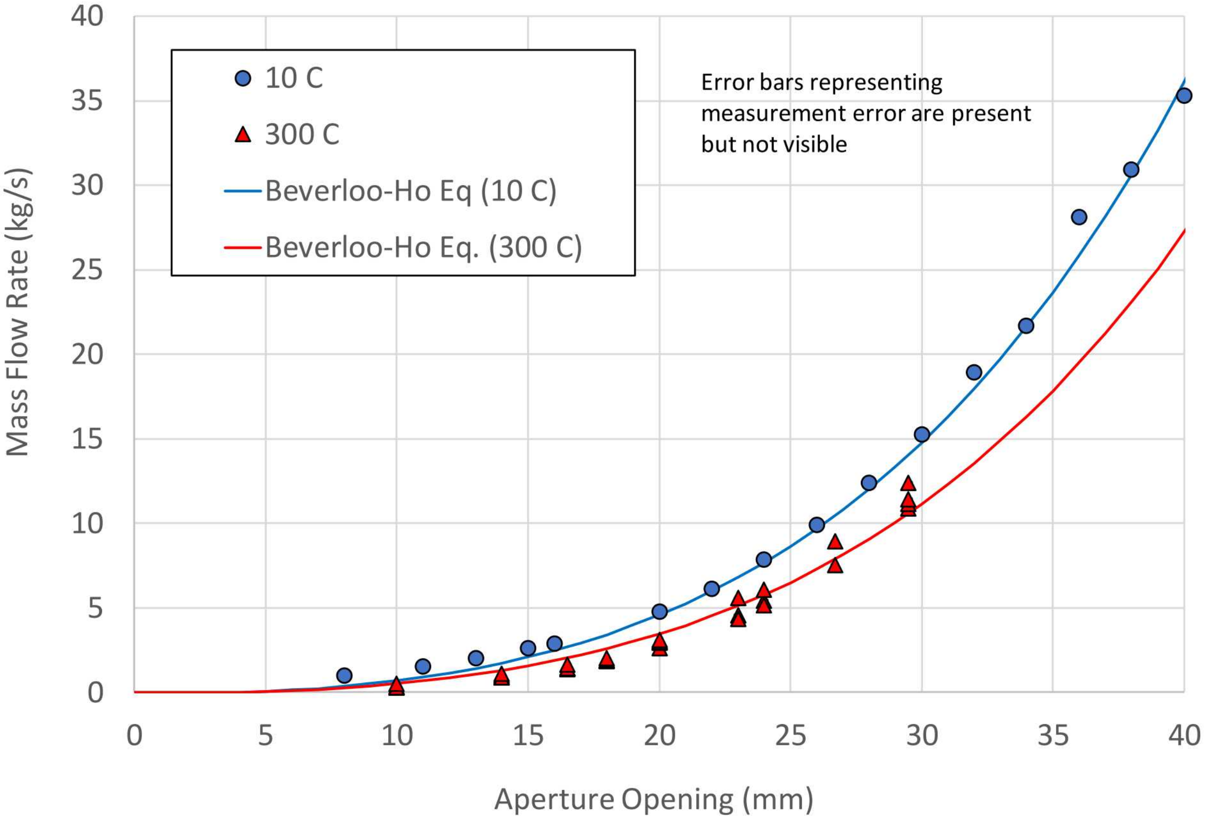

Figure 47. Particle mass flow rate vs. aperture opening for different particle inlet temperatures. Symbols denote measured values using in-situ weigh hopper. Lines denote predictions using modified Beverloo-Ho equation.

4.1.3. Test Procedure

Detailed test procedures are provided in Appendix B. In brief, the following procedure was follows during on-sun testing:

- All equipment was turned on according to the startup checklist
- Heliostats were brought online to a standby position next to the receiver
- The slide gate was set to a desired aperture and the mass flow rate was measured using the weigh hopper
- The heliostats were aimed at the flux target next to the receiver aperture and photos were taken to obtain an irradiance distribution using the Kendall radiometer at the center of the flux target to scale the pixel values (see Figure 48)
- The heliostat beam was moved to the receiver aperture to heat the particles
- As the particle outlet temperatures were recorded, periodic mass-flow measurements were taken
- This process was repeated at different particle temperatures, particle mass flow rates, and irradiances
- For particle mass flow control tests, the control system was allowed to automatically adjust the slide gate and slot aperture to increase or decrease the particle flow according to the particle outlet temperature. Heliostats were added or removed to simulate perturbances in the solar irradiance and/or the particle setpoint temperature was adjusted periodically to accommodate the increasing temperatures.

Figure 48 provides an example of the measured irradiance distribution on the flux target and aperture during a high-irradiance scenario. The average irradiance on the aperture in Figure 48 was ~900 kW/m^2. During the on-sun tests, the peak flux was typically varied between ~500 kW/m^2 and 1000 kW/m^2 (see Table 19). In theory, greater irradiances (concentration ratios) yield higher receiver thermal efficiencies [20]. Achieving peak fluxes up to 1000 kW/m^2 is possible with current state-of-the-art commercial CSP plants.

The particle absorptivity also plays a role in the thermal efficiency of the receiver. The absorptivity of the CARBO ceramic beads is ~0.9, and the thermal emissivity is ~0.8 – 0.9 [21]. Because the particles are falling through a cavity receiver, a reduced particle intrinsic absorptivity can be offset by the blackbody effect of the cavity receiver.

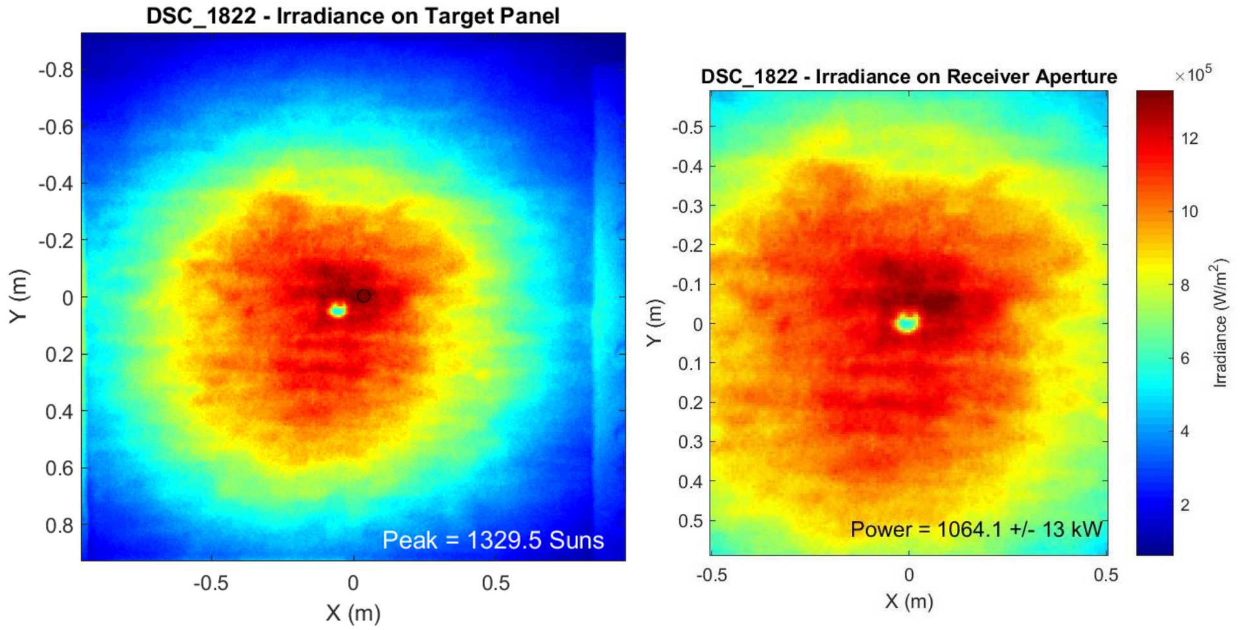

Figure 48. Example of measured irradiance distribution on the target panel (left) and receiver aperture (right) during on-sun tests.

4.1.4. Test Results

A total of 26 on-sun tests were performed with different particle mass flow rates, irradiances, and particle temperatures using the in-situ weigh hopper to measure the particle mass flow rate during each test. The particle inlet and outlet temperatures, input power, ambient temperature, wind speed, and wind direction were recorded for each test. The thermal efficiency was calculated using Eq. (1), and the results are summarized in Table 19.

Table 19. Summary of on-sun tests performed to determine particle heating and thermal efficiency.

Event Number	Peak Irradiance (kW/m^2)	Mass Flow Rate (kg/s)	Average Particle Inlet Temp (C)	STD Inlet T (C)	Outlet Average Temp (C)	STD Outlet T (C)	Aperture Input Power (W)	STD Input Power (W)	Thermal Efficiency	Efficiency Propagated Error	Ambient Temp (C, Min - Max)	Wind Speed (mph)	Wind Direction (deg, North=0, East=90)
January 23, 2018													
10	1060	5.54	334.14	1.7	436.4	5.6	950600	7000	0.63	0.04	4.05 - 8.06	4-8	360
13	660	8.58	505.79	5.1	537.3	5.8	592800	3000	0.51	0.08	4.05 - 8.06	5-6	360
14	1057	8.02	570.80	5.2	629.5	5.6	948500	7000	0.57	0.02	4.05 - 8.06	3-12	320
15	1052	7.48	605.86	18.0	667.9	8.1	950200	8000	0.57	0.17	4.05 - 8.06	3-12	320

Event Number	Peak Irradiance (kW/m^2)	Mass Flow Rate (kg/s)	Average Particle Inlet Temp (C)	STD Inlet T (C)	Outlet Average Temp (C)	STD Outlet T (C)	Aperture Input Power (W)	STD Input Power (W)	Thermal Efficiency	Efficiency Propagated Error	Ambient Temp (C, Min - Max)	Wind Speed (mph)	Wind Direction (deg, North=0, East=90)
16	557	6.02	542.82	6.9	594.9	7.2	509500	8000	0.70	0.06	4.05 - 8.06	-	-
17	549	6.21	549.98	4.3	598.8	5.1	502600	4000	0.69	0.06	4.05 - 8.06	-	-
18	537	10.61	532.41	6.1	552.1	6.7	492100	7000	0.48	0.05	4.05 - 8.06	10-19	330
February 2, 2018													
1	516	7.53	318.30	5.3	356.7	6.4	484600	3000	0.62	0.05	8.34 - 13.14	3-7	200
2	560	5.60	551.75	3.2	609.8	2.7	518400	5000	0.72	0.04	8.34 - 13.14	10-13	200
3	561	9.24	564.88	1.0	602.1	1.4	514700	6000	0.77	0.07	8.34 - 13.14	10-12	200
4	585	8.77	566.19	0.5	608.0	0.6	533000	7000	0.77	0.03	8.34 - 13.14	11-17	200
5	590	11.18	573.06	0.4	611.9	0.6	537200	5000	0.93	0.03	8.34 - 13.14	-	-
6	1093	10.83	571.63	6.5	644.2	6.0	978600	10000	0.91	0.04	8.34 - 13.14	11-17	180
February 8, 2018													
1	1036	10.29	271.90	1.8	321.8	2.6	928300	8000	0.56	0.04	8.58 - 13.98	4-8	270
2	252	6.90	261.15	15.0	283.4	13.5	236100	2000	0.65	0.09	8.58 - 13.98	6-7	300
3	1074	6.50	607.57	14.6	679.1	12.4	963000	12000	0.56	0.05	8.58 - 13.98	-	-
4	994	7.06	553.47	0.9	619.5	1.5	889400	12000	0.60	0.02	8.58 - 13.98	3-9	300
February 26, 2018													
1	670	11.52	320.0	7.1	360.0	6.7	579200	6000	0.83	0.16	5.31 - 11.47	15-16	180
2	686	5.05	310.7	21.8	387.9	20.0	588400	7000	0.69	0.05	5.31 - 11.47	17-20	180
3	1278	10.44	362.2	26.2	457.8	26.3	1125600	16000	0.96	0.08	5.31 - 11.47	11-13	180
4	1225	4.87	332.3	41.8	484.5	38.1	1105000	11000	0.72	0.05	5.31 - 11.47	17-20	180
5	1185	8.22	493.2	46.4	581.9	45.9	1064000	13000	0.78	0.12	5.31 - 11.47	12-14	180
6	1173	9.76	531.5	5.7	613.3	5.7	1053500	11000	0.87	0.06	5.31 - 11.47	15-22	200
7	1160	7.30	641.4	18.6	747.7	21.0	1040100	13000	0.88	0.07	5.31 - 11.47	13-22	180
February 27, 2018													
1	520	9.94	295.8	11.6	332.9	11.7	475100	5000	0.80	0.07	7.79 - 12.01	12-6	0
4	1750	8.39	406.3	9.6	551.8	9.8	1582900	13000	0.85	0.08	7.79 - 12.01	22-16	0

The relative errors within the calculated thermal efficiency were propagated from the individual measurements as follows:

$$\sigma_{total} = \sqrt{\sigma^2_{load,flat} + \sigma^2_{load,inclined} + 2\sigma^2_{TC} + \sigma^2_{TC,transient} + \sigma^2_{Kendall} + \sigma^2_{flux\,image} + \sigma^2_{transients}} \qquad (8)$$

Table 20 summarizes the relative error sources and the propagated relative and absolute error in the thermal efficiency calculation.

Table 20. Summary of relative error sources in efficiency calculation for on-sun tests.

Relative Error Source	Description	Value (%)	Basis
$\sigma_{load,flat}$	Relative error in the load cells when perfectly flat	0.13	Based on multiple measurements with prescribed weights (1 s.d.)
$\sigma_{load,inclined}$	Relative error in the load cells when inclined by ~2 degrees	0.21	Based on multiple measurements with prescribed weights (1 s.d.)
σ_{TC}	Measurement error of Type-K thermocouples	0.75	From manufacturer (Thermometrics)
$\sigma_{TC,transient}$	Transient readings in the measured ΔT	1.3 – 21	Measured data during each test (1 s.d.). Transients are largely caused by wind.
$\sigma_{Kendall}$	Measurement error of Kendall radiometer	2.2	From calibration measurements
$\sigma_{flux\ image}$	Measurement error in irradiance distribution using camera images	0.7 – 1.6	Digital image of heliostat beams on flux target was translated 10 cm up, down, right, and left to get average and standard deviation of total power entering aperture
σ_{total}	Total propagated relative error in the thermal efficiency calculation	6.9 – 21	Errors are assumed to be independent (Eq. (8))
η_{error}	Total propagated error in the thermal efficiency	1.6 - 12	$\eta_{error} = \sigma_{total} \cdot \eta_{th}$, where η_{th} is calculated by Eq. (1)

Figure 49 shows the measured particle temperature rise as a function input power, particle mass flow rate, and average particle inlet temperature. Results show that the input power is strongly correlated to the particle temperature rise, as expected. The particle mass flow rate and temperature show less of a correlation; we suspect that the impact of wind on various test days may be confounding the results.

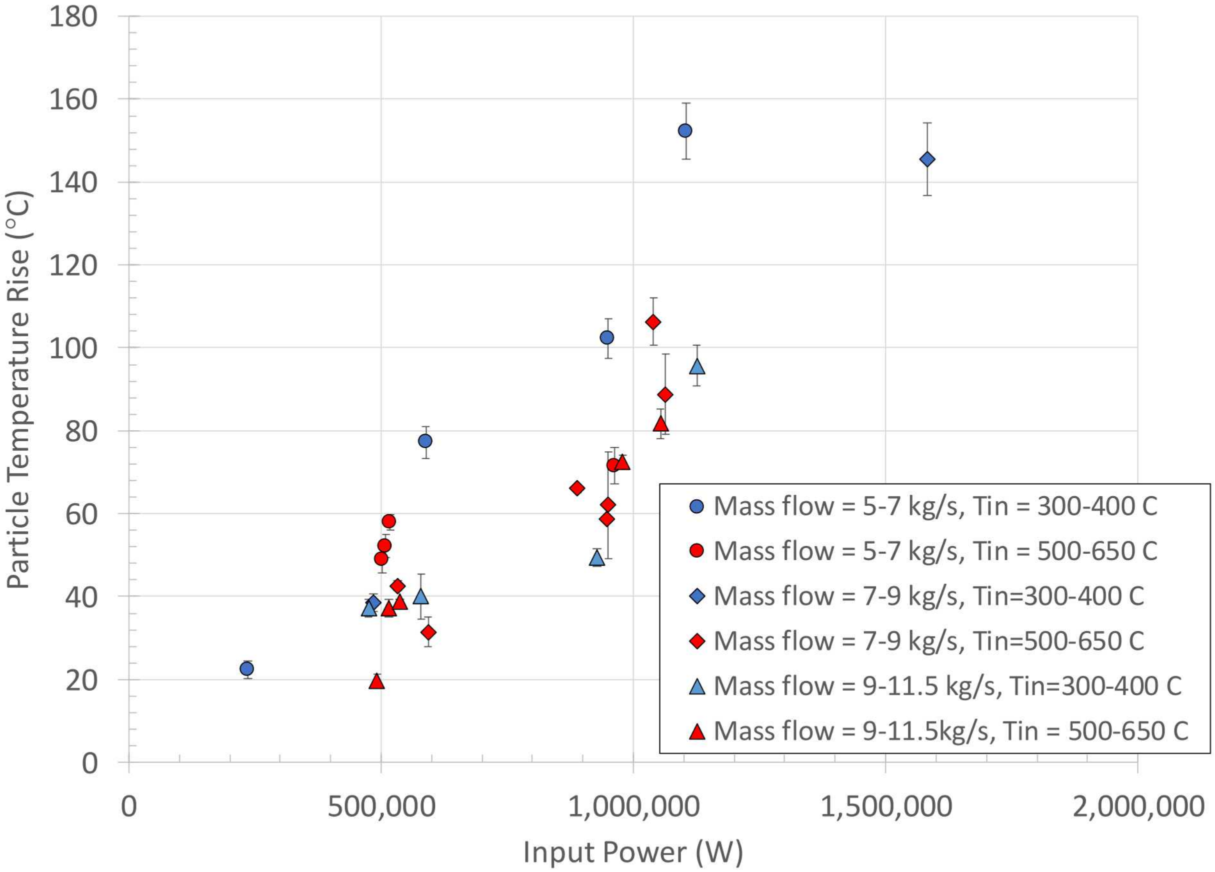

Figure 49. Measured particle temperature rise as a function of input power, particle mass flow rate, and average particle inlet temperature (Tin) during on-sun tests. Error bars represent one standard deviation.

Figure 50, Figure 51, and Figure 52 show the measured thermal efficiency as a function particle mass flow rate, input power, and particle inlet temperature, respectively. The plots do not show a clear correlation since the mass flow rate, input power, and particle inlet temperature can have competing effects. In addition, the wind speed and direction during each test can also have an impact on the measured thermal efficiency. Figure 53 shows the measured thermal efficiencies as a function of wind speed and wind direction. It appears that the higher efficiencies are associated with higher wind speeds, but confounding effects of particle mass flow rate, temperature, and irradiance exist. Additional analyses of the particle temperature rise, thermal efficiency, and parametric correlations are presented in Section 4.2. Analyses of the automated particle mass flow control to maintain a constant particle outlet temperature are presented in Section 4.3.

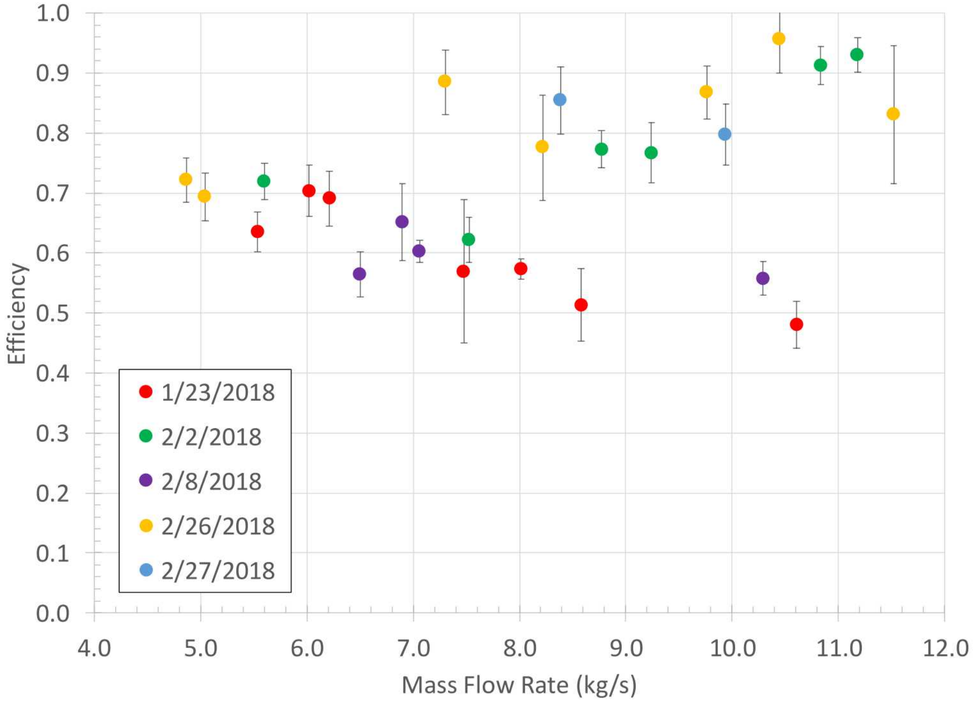

Figure 50. Measured thermal efficiency as a function of mass flow rate during 26 on-sun tests over 5 dates.

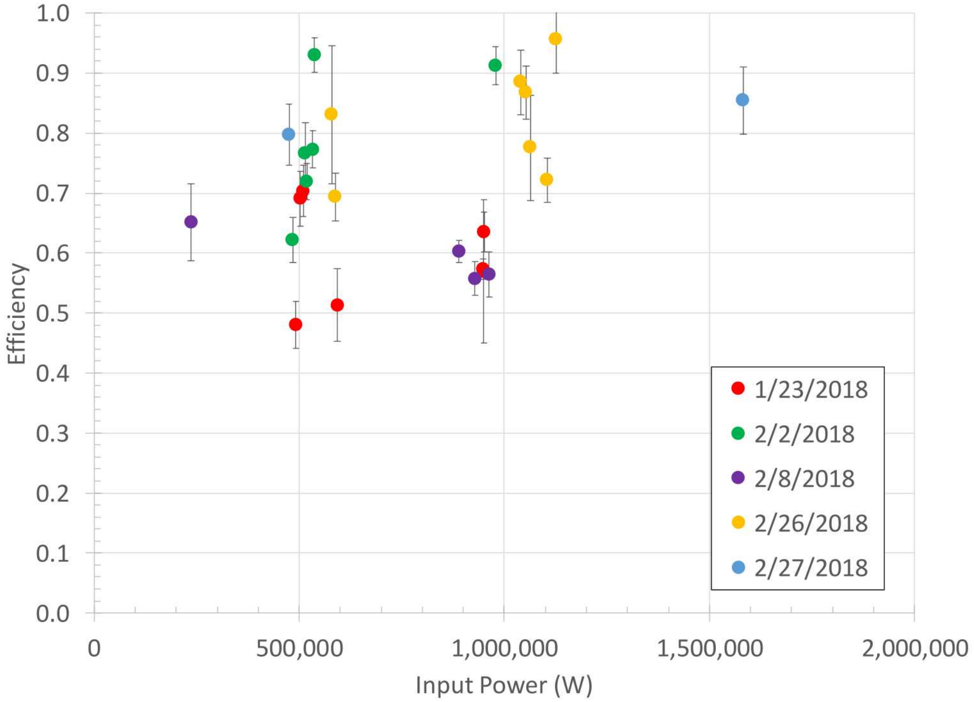

Figure 51. Measured thermal efficiency as a function of input power during 26 on-sun tests over 5 dates.

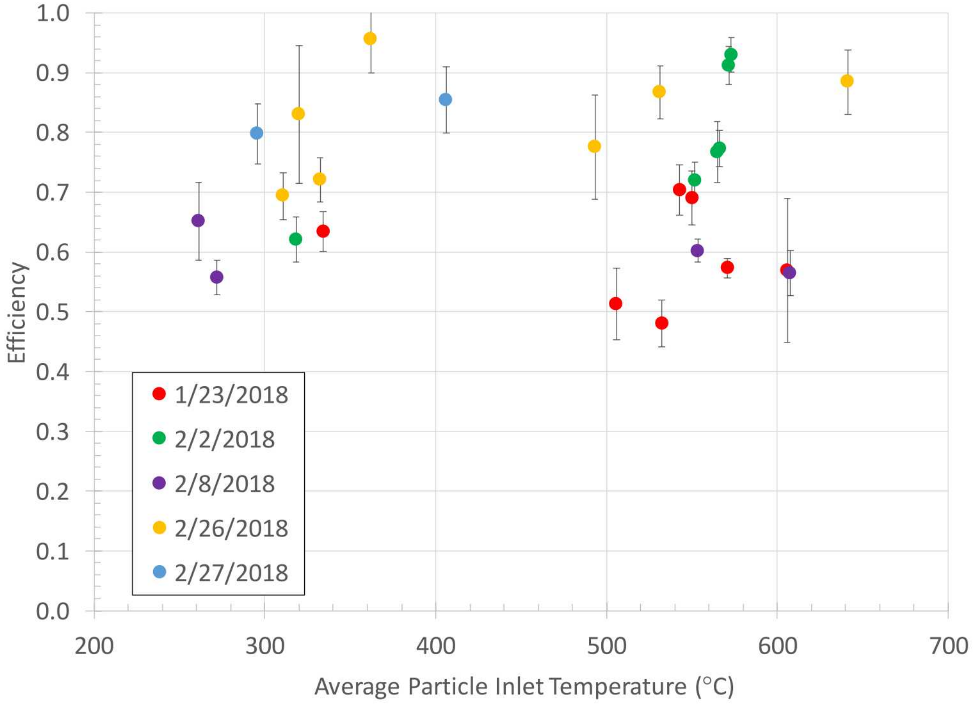

Figure 52. Measured thermal efficiency as a function of average particle inlet temperature during 26 on-sun tests over 5 dates.

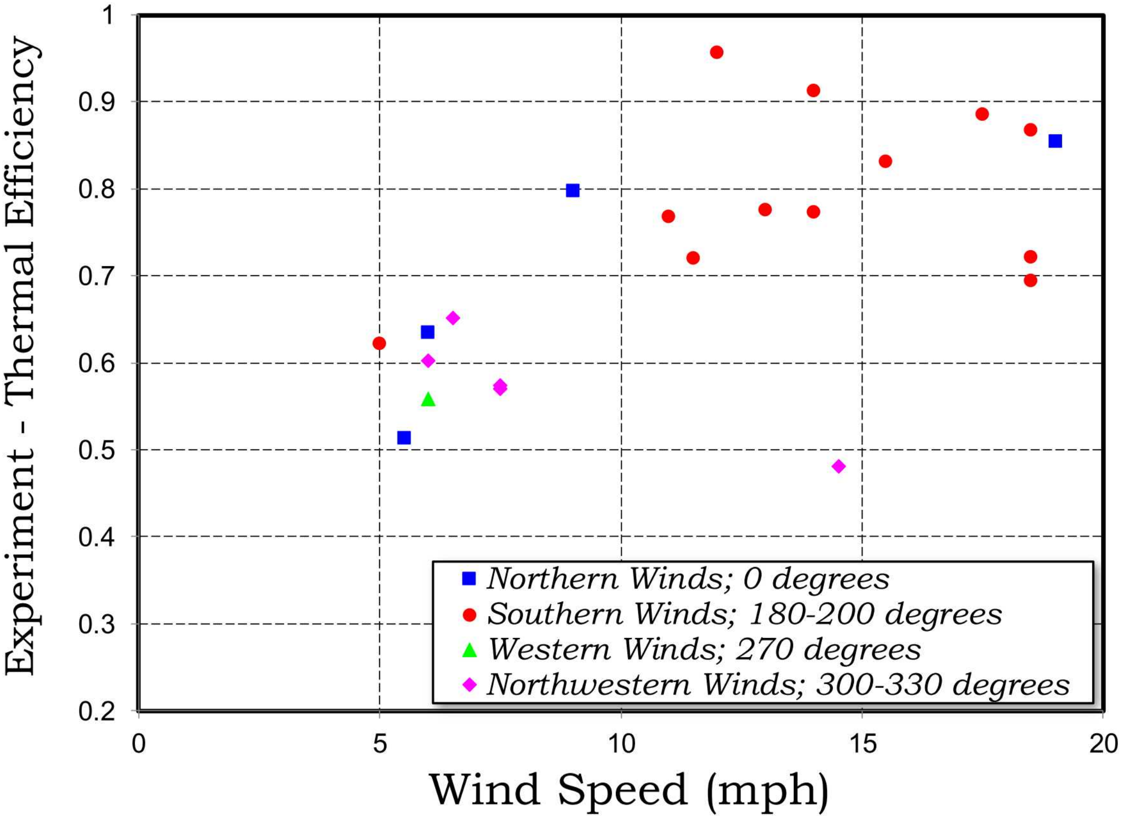

Figure 53. Measured thermal efficiency as a function of average wind speed and direction during on-sun tests.

4.2. Modeling

A thermal model of the existing particle receiver was developed in ANSYS Fluent® 17.1 to compare with the experimental data. The purpose of this modeling effort was to characterize the thermal loss mechanisms from the receiver that could inform future receiver development and to demonstrate a predictive capability in the modeling approach using experimental data. This modeling approach follows a strategy outlined in previous reports and also appears in the literature. A description of the model used here is provided for reference.

The geometry of the receiver model is depicted below in Figure 54 (similar to Figure 15 but with an external air region outside the receiver aperture). The receiver itself is comprised of 406,072 hexahedral cells. A mesh of the air immediately outside of the receiver aperture has been included to capture air flow in and out of the receiver. The external air volume consisted of 37,620 hexahedral cells. Previous simulations described in Mills and Ho [10] for similar receiver sizes have demonstrated that this mesh resolution was sufficient to assure that the spatial discretization error was negligible.

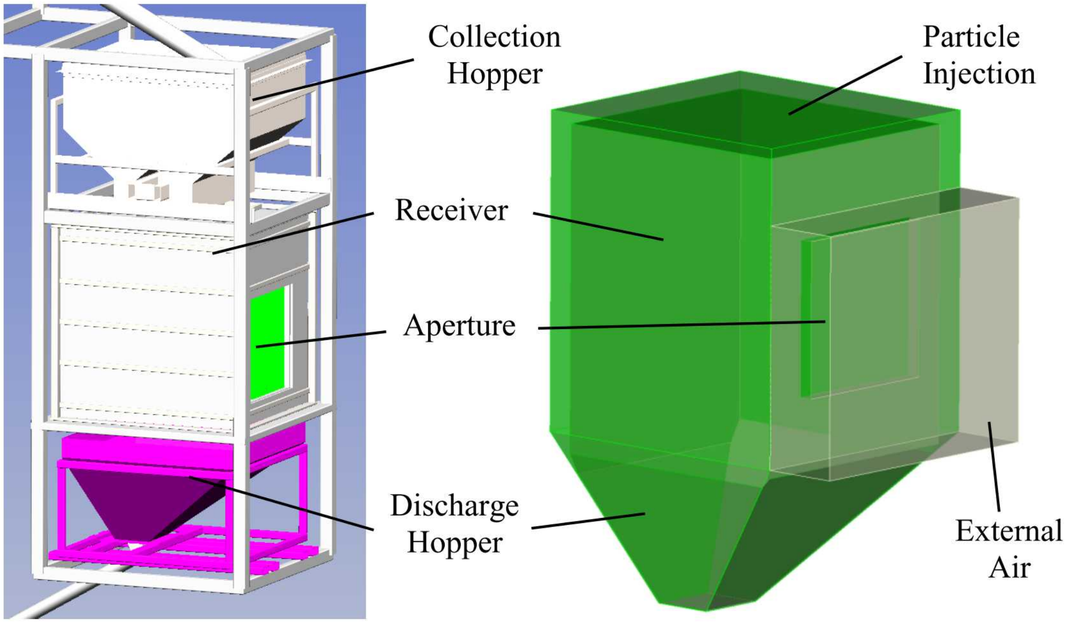

Figure 54. Solid model of the existing receiver (left) and the simplified solid model of the geometry used for the thermal model (right)

A coupled Lagrangian-Eulerian model was developed to model the particles as they fell through the air in the receiver cavity and were heated by the incident solar radiation from the heliostats. The particles were coupled to the air through drag forces and heat transfer occurring between the particles and the air as they fell. Air was allowed to enter or exit the receiver through the aperture. Turbulent flow inside the receiver was modeled using the realizable k-ε turbulence model and Fluent's scalable wall functions for a degree of mesh independence near the walls. Boundary conditions for the air were modeled as fixed pressure boundary conditions at ambient pressure and temperature.

Particles were released from 600 injection sites near the top of the receiver cavity and tracked through the domain before exiting out the hopper. These injections sites correspond to the location and size of the adjustable slot in the receiver. Particle to particle interaction was not included under the assumption that the volume fraction of particles in the air volume was sufficiently small. This assumption was valid for volume fractions less than 10%. Previous tests on falling particle receivers have indicated that the volume fraction of particles was less than several percent [4, 8]. For the simulations described here, particles were defined as CARBO HSP 20/40 (82% Al2O3, 5% SiO2, 3.5% TiO2) with ~7% iron oxide with a particle diameter of 350 microns.

A non-grey, discrete-ordinates (DO) radiation model was used to simulate radiation transport inside the domain. Both angular dimensions were discretized into eleven divisions per octant. The wavelength spectrum was divided into three spectral bands, 0.1–2.5 µm, 2.5–4.5 µm and 4.5–100 µm. All incident solar radiation was defined to enter the domain entirely in the smallest wavelength band (0.1–2.5 µm). The two higher wavelength bands were representative of emission of thermal radiation, and the delineation accounted for different emissive properties of the alumina silica ceramic fiberboard walls. Incident solar radiation to the domain was applied as a radiative boundary condition on the aperture. The entire aperture is defined to emit the concentrated solar radiation with a representative flux profile determined from measurements taken during the experiments. The incident beam direction emitted from a cell face on the aperture was determined using the method described by Khalsa and Ho [14] for the heliostats used in a particular experiment.

Conduction through the walls of the receiver was also included in addition to convection and radiation on the exterior walls to the surrounding environment. A value of 5.0 W/m^{2}K was used based on an empirical heat transfer coefficient correlations and appreciation for structural obstructions around the exterior of the experiment. It is important to emphasize that the effect of external winds on the particle curtains themselves was not considered in these simulations due to the added computational expense with the inclusion of a significantly larger exterior air domain and supporting nearby structures.

A series of experiments was performed with the falling particle receiver varying the mean particle inlet temperature, particle mass flow rate, and radiative flux from the heliostats. Each of these experiments was simulated with the model assuming steady-state conditions and the increase in particle temperature (ΔT) and the thermal efficiency of the receiver was calculated. These values were then compared with corresponding experimentally calculated value for each case to evaluate the model. The thermal efficiency is given by Eq. (1).

The change in mean particle temperature and the thermal efficiency of the receiver for the model and the experiment are plotted below in Figure 55.

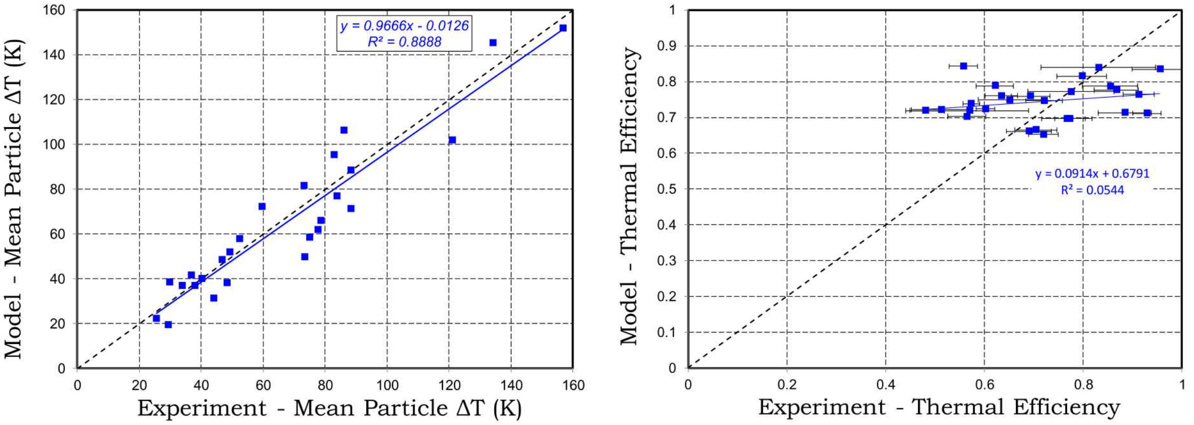

Figure 55. Comparison of the mean particle temperature increase (left) and the thermal efficiency (right) between the model and the experiment for on-sun tests.

Despite seeing good overall agreement in the particle temperatures, the scatter in the data results in large discrepancies in the thermal efficiency that can't be explained by the experimental uncertainty alone. A similar result was also observed in previous simulations of on-sun tests prior to implementation of the weigh hopper for real-time in-situ particle mass flow measurements [22]. While the uncertainty in the mass flow rate has been reduced, additional physics are likely contributing to the large disagreement that the model is presently unable to capture. Through examination of all the recorded experimental data, the direction and speed of external winds were found to be highly correlated with the discrepancy between the experimental efficiency and the model efficiency. For northwesterly or westerly winds, thermal efficiencies were typically lower than predicted in the model. However, for days with southern winds, thermal efficiencies were closer to the model's predictions. There was also a strong correlation between the wind speed and the direction since only a limited number of test days were available, and the winds varied little for each respective day. These relationships are depicted in the Figure 56. It is currently unclear why tests with higher measured wind speeds yielded higher thermal efficiencies than the simulated results, which did not include the effects of wind, and vice-versa.

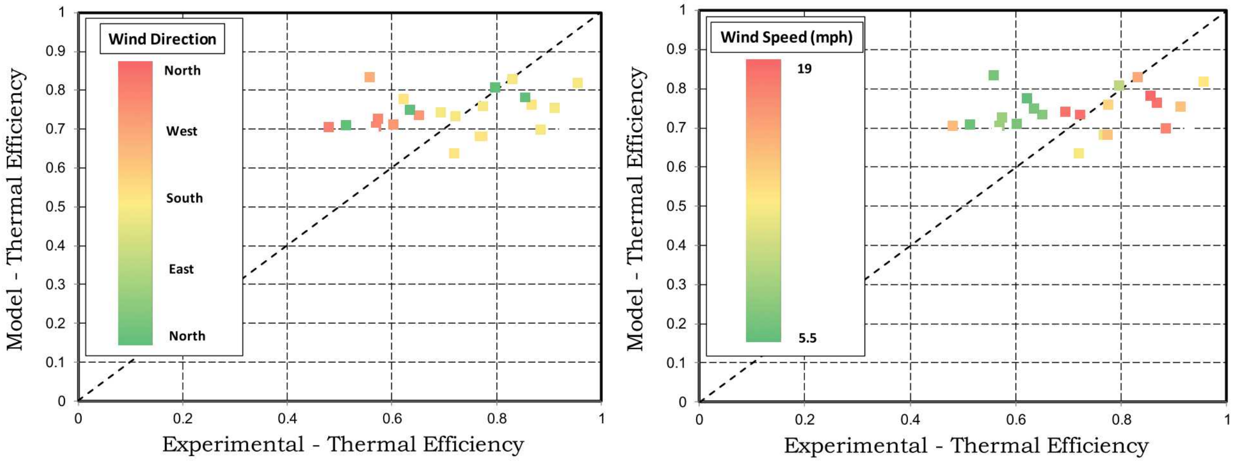

Figure 56. Experimental and numerical thermal efficiency of the receiver colored by the wind direction (left) and speed (right) for on-sun tests.

As discussed above, the model in its current form is presently unable to account for the effect of external winds on the receiver. Such effects should realistically influence the particle curtain, the advective losses from the receiver aperture, and the convection from the receiver walls. However, the computational expense required to model external winds on the receiver would increase significantly with the addition of properly modeling all structural elements on the tower and a significantly larger computational domain. In addition, the ability to properly measure the wind speed variation and direction on the boundaries would need to be done with confidence. Without such detail, the additional computational expense and uncertainty would likely not add accuracy to the model. Going forward, a better approach would be to use various strategies to minimize the effect of wind on the receiver and particle curtain.

To more effectively evaluate the model, only cases from a single day were selected to minimize the effect of wind variability on the receiver's efficiency (and the particle curtain). Seven experiments were performed on February 26, 2018, where predominately southern winds were observed during the tests. When comparing only these seven cases against the model, three of the seven compared well with the model within experimental uncertainty, but three cases were still outside of the model's predictions suggesting that southern winds still affected the thermal efficiency. The results are shown in Figure 57.

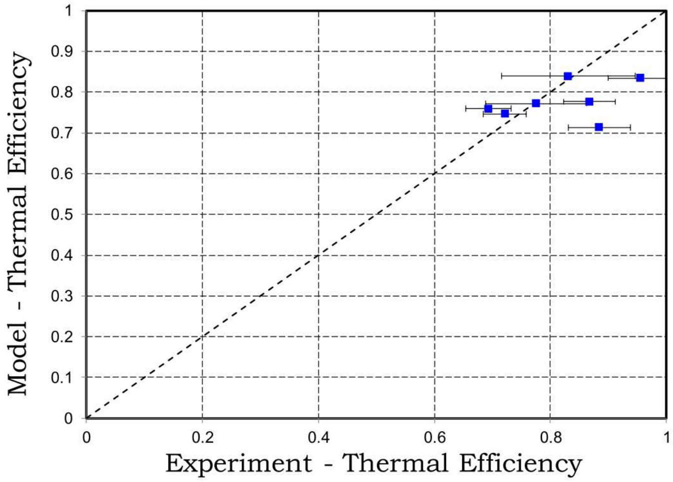

Figure 57. Experimental and numerical thermal efficiency of the receiver for on-sun experiments performed on 2/26/18.

An empirical correlation was also developed from the experimental data to help in evaluating the model and attempt to statistically account for the effect of external winds. Using Minitab, a general regression fit for the thermal efficiency was created using five input variables: the input radiative power Q (W), the particle mass flow rate $\dot{m}$ (kg/s), the inlet particle temperature $\overline{T}_i$ (in Kelvin), the wind direction θ, and the mean wind speed $\bar{v}$ (mph). Although the physical meaning of terms in a correlation of this form often cannot be justified from first principles, a properly created model can retain some predictive capability if all of the relevant variables are identified and shown to be statistically significant. It should be emphasized that the correlation is valid for the conditions under which it was created, but some minor extrapolation will be used here to attempt to remove the effect of winds from the experimental data to compare with model. That is, the correlation was evaluated using the experimentally measured parameters for the input radiative power, particle mass flow rate, and inlet particle temperature with a wind speed of zero.

Minitab's backward elimination method was applied to derive the regression model from the experimental data with some logical consideration to the variables that were available for use. For example, the wind direction (specified as the cosine of the angle where 0° is a north wind and 90° was an east wind) was not allowed to appear in the model separately from the wind speed since the effect of the wind direction would be negligible if the wind speed was zero. Likewise, the particle mass flow rate was known to be a critical term to the thermal efficiency from previous analysis and was kept in the correlation. Terms were eliminated from the correlation based on their probability value (p-value) or their variance inflation factors and engineering judgement. The resulting correlation for the thermal efficiency η was determined as follows in Eq. (9):

$$\eta = 0.63 + 0.0331\dot{m} - 4.43 \times 10^{-5}\dot{m}\overline{T}_i + 1.946 \times 10^{-5}\dot{m}\overline{T}_i Q + 0.0216\bar{v} - 0.00362\,\bar{v}\cos\theta - 3.62 \times 10^{-5}\overline{T}_i\,\bar{v}\cos\theta + 0.03024\,\bar{v}\cos^2\theta \tag{9}$$

The experimentally derived correlation is compared with the experimental data in Figure 58 (where wind data was available). As observed in the figure, the correlation predicts the experimental thermal efficiency well ($R^2 = 0.79$). The correlation is also plotted in Figure 58 against the model assuming the same experimental parameters, but for a wind speed of zero. The correlation without wind is shown to agree very favorably with the model and a linear fit of the resulting data gives a slope of 0.93 and an $R^2 = 0.81$. Though this analysis does not confirm that in the absence of wind the model can predict the thermal efficiency, this analysis does support the applicability of the physical heat transfer models (i.e. radiation, conduction, etc.) used to model the receiver.

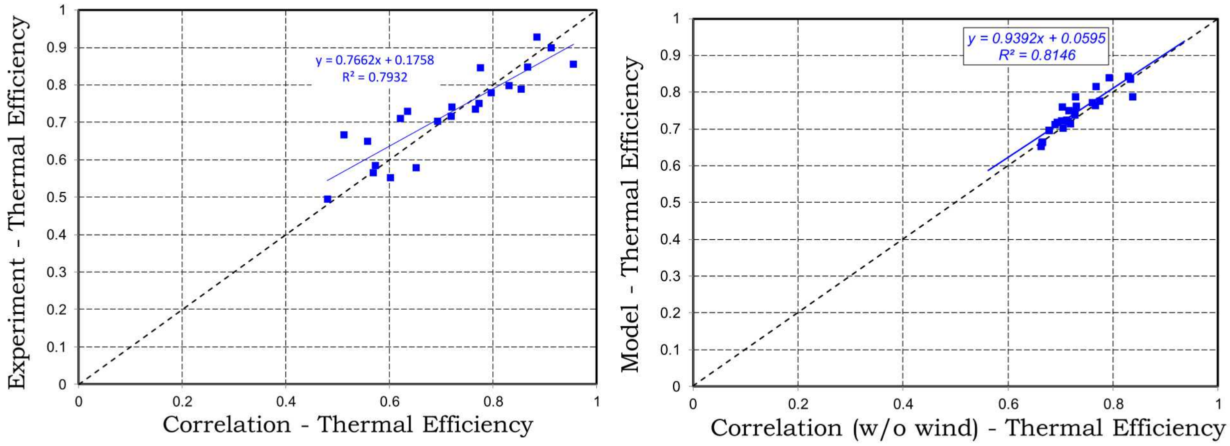

Figure 58. The correlation compared to the experimental thermal efficiency (left) and the correlation compared to the CFD model thermal efficiency with $\bar{v} = 0$ (right).

Based on these simulated results, neither the CFD simulations nor the empirical correlations meet the performance evaluation criterion in Table 21 for the measured vs. predicted thermal efficiency of the receiver. Although the particle mass flow rate was well characterized, additional uncertainties from wind that were not well characterized in the models caused discrepancies between the model predictions and experimental results.

Table 21. Performance evaluation criterion for on-sun modeling and testing of thermal efficiency.

	Metric Definition (From Measurement)	***Success Value***	***Assessment Tool (Quality Assurance)***	***Goal Met (Y/N)***	***Supporting Data***
Project Evaluation Criteria 2.4.1	Measured vs. predicted thermal efficiency	$R^2 > 0.95$ $0.95 \leq \text{Slope} \leq 1.05$ Constraint: Modeled boundary conditions should match the experimental conditions for each test.	R^2 and slope of linear curve fit of measured vs. predicted thermal efficiency	N	Figure 55, Figure 58

The temperature of the back wall behind the particle curtain was also measured in the experiment at a single location. This temperature location was evaluated against the model and the comparison is shown in Figure 59. Three outliers were removed for being significantly different than other points in the data set and were assumed to be inaccurate readings. Overall, while having similar trend, the model tended to under predict the backwall temperature. The incident radiative power was also plotted on this figure, and temperatures on the backwall agreed much more closely to the model for the higher heat fluxes (the highest heat flux was removed as an outlier). Likely, the largest reason for the differences in temperature is the uncertainty in the thermal conductivity of alumina silica ceramic fiberboard at elevated temperatures. Also, the impact of wind on the measured backwall temperatures may have been more significant at lower incident power levels.

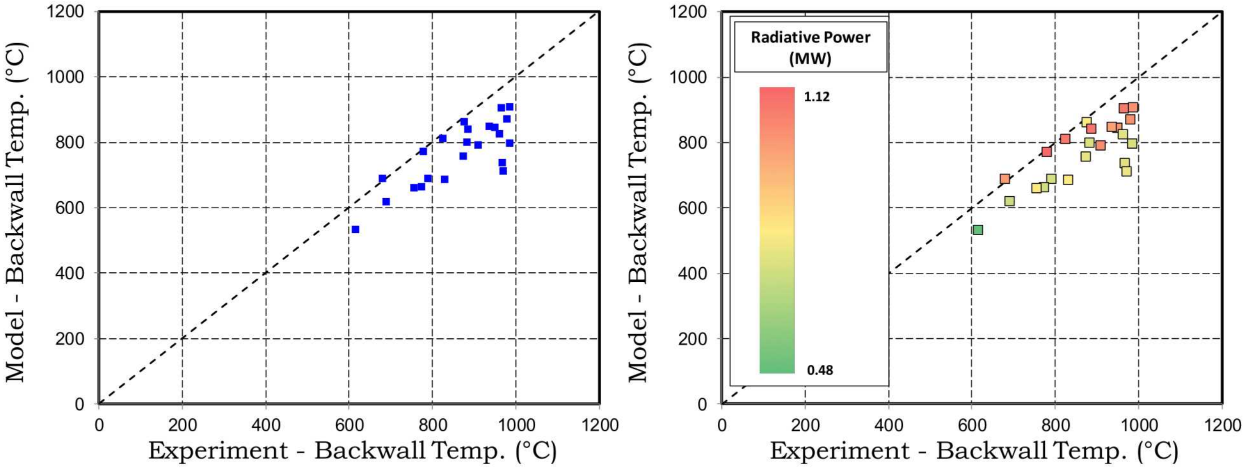

Figure 59. Backwall temperature between the experiment and the model (left) and colored by the incident radiative power (right)

The thermal efficiency in the model is also plotted against the particle mass flow rate and the incident radiative power in Figure 60 for the available test cases. When fit, both dataset showed positive slopes indicating that increasing the particle mass flow rate or the power to the receiver increased the thermal efficiency of the receiver. This proves advantageous as both of these parameters would increase as a particle receiver is scaled up. The simulated thermal efficiency is also plotted against the particle inlet temperature in Figure 60. As expected, there is a negative correlation between thermal efficiency and particle temperature since greater heat losses occur at higher temperatures. The “one-off” regressions do not show high R^2 values because of the confounding effects of the particle mass flow rate, particle temperature, and irradiance on the thermal efficiency for the different test cases.

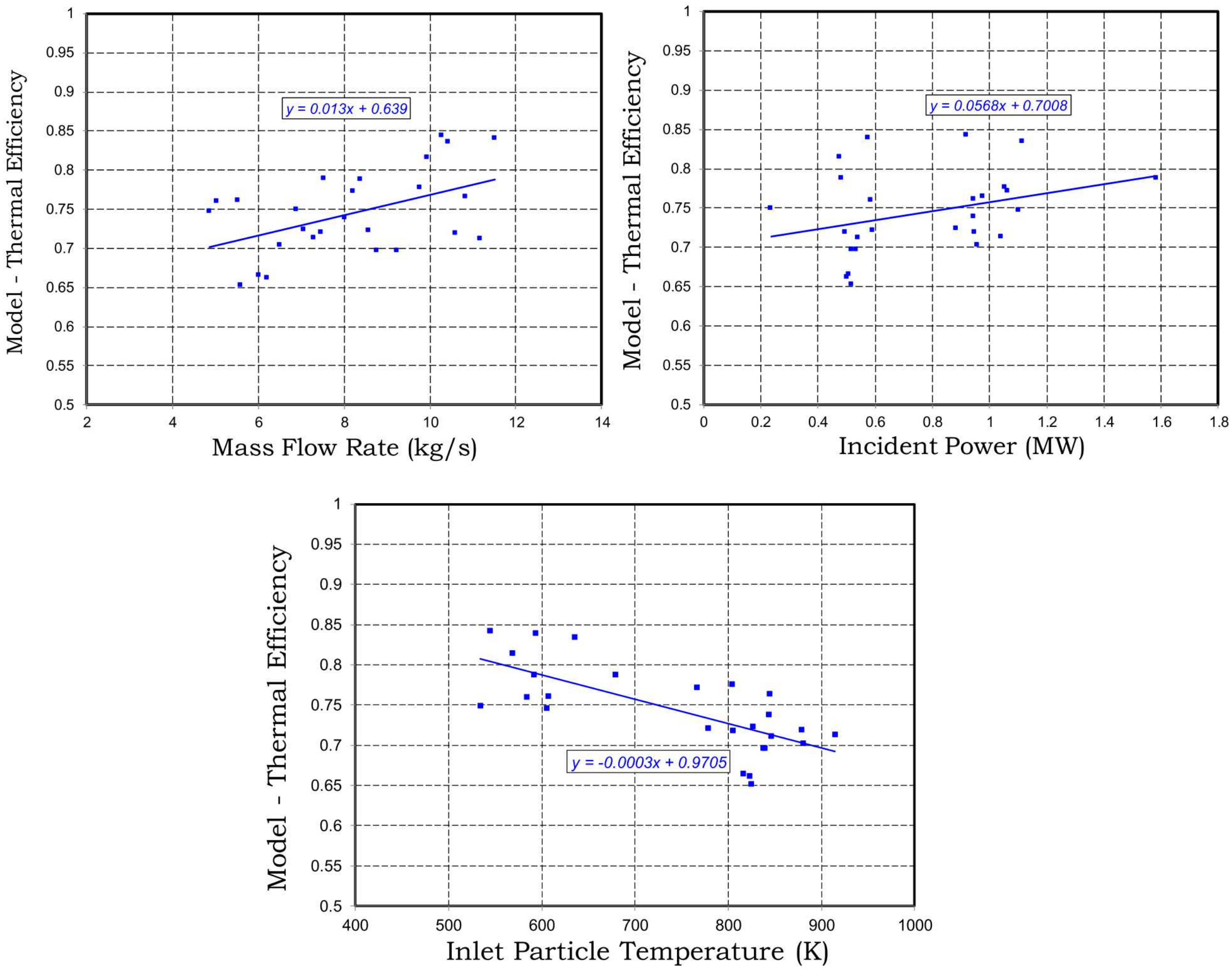

Figure 60. Thermal efficiency of the model plotted against the particle mass flow rate (top left), incident radiative power (top right), and particle inlet temperature (bottom).

The various heat loss mechanisms in the model are delineated for several cases and plotted in Figure 61. Thermal losses from the receiver included radiative losses from each wavelength band, convective losses to the air that were advected away from the domain, and thermal losses through the receiver walls that are ultimately convected or radiated away to the environment. The thermal losses from each mechanism are normalized to the total incident thermal power to define a percentage of incident thermal energy lost in the figure below. The cases that are plotted include different mass flow rates, incident powers, and inlet particle temperatures and are summarized in Table 22.

Table 22. Sample Cases Selected for Figure 61

#	Date of Test	Incident Power (MW)	Inlet Particle Temp. (°C)	Particle Mass Flow Rate (kg/s)
1	23-Jan	0.95	605.9	7.48
2	23-Jan	0.49	532.4	10.61
3	2-Feb	0.52	551.7	5.60
4	26-Feb	1.10	332.3	4.86

#	Date of Test	Incident Power (MW)	Inlet Particle Temp. (°C)	Particle Mass Flow Rate (kg/s)
5	26-Feb	1.04	641.4	7.30
6	27-Feb	0.48	295.8	9.94
7	27-Feb	1.58	406.3	8.39

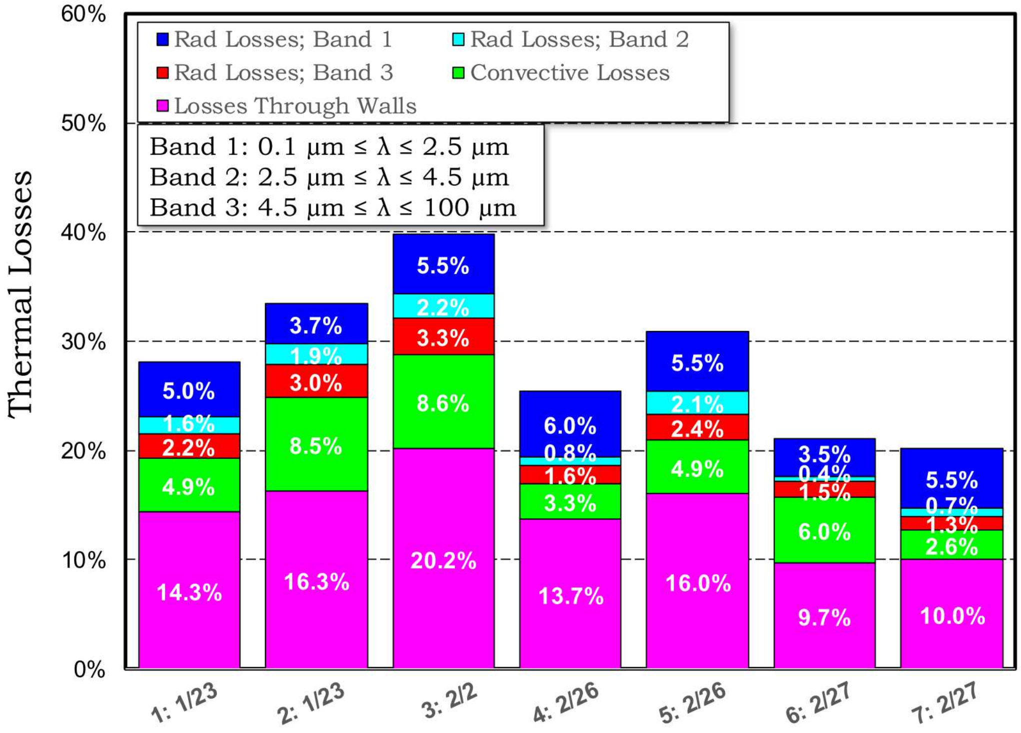

Figure 61. Simulated losses from the receiver for sample cases in Table 22.

According to the model, the most significant losses from the receiver are through the walls with values ranging from ~10 – 20%. Fortunately, these losses are the most simple and cost-effective to reduce and can be mitigated by adding additional insulation to the receiver in future designs. Radiative losses from the smaller wavelength band (Band 1) are associated with reflected losses from the domain. Losses in this band made up the highest quantity of radiative losses, but were observed to decrease with increasing particle mass flow rate (greater opacity in the particle curtain intercepted more of the incident solar radiation). Likewise, the convective losses from hot air escaping the domain (and replaced by cooler air) tended to decrease for higher incident radiative powers. These mechanisms describe some of the means by which increases in efficiency are gained in Figure 60.

4.3. Automated Particle Mass-Flow and Temperature Control

A total of 15 on-sun tests were performed to evaluate the automated particle mass-flow control system to maintain a desired particle outlet temperature. The test protocol for these tests is detailed in Appendix B. A set number of heliostats was used to heat the particles. To simulate a solar flux perturbation, one of several methods was implemented: (1) several heliostats were added or removed, (2) the test was performed during a partly cloudy day, or (3) the long-term continuous heating of the particles in the recirculation loop was used to represent gradual changes in irradiance. A desired setpoint temperature was entered into the Labview data acquisition system interface, and the system automatically adjusted the position of the slide gate and resulting particle mass flow through the aperture in an attempt to maintain the desired particle outlet temperature. Figure 62 shows the dynamic positioning and resulting particle outlet temperature during a test with a particle outlet setpoint temperature of 380 °C.

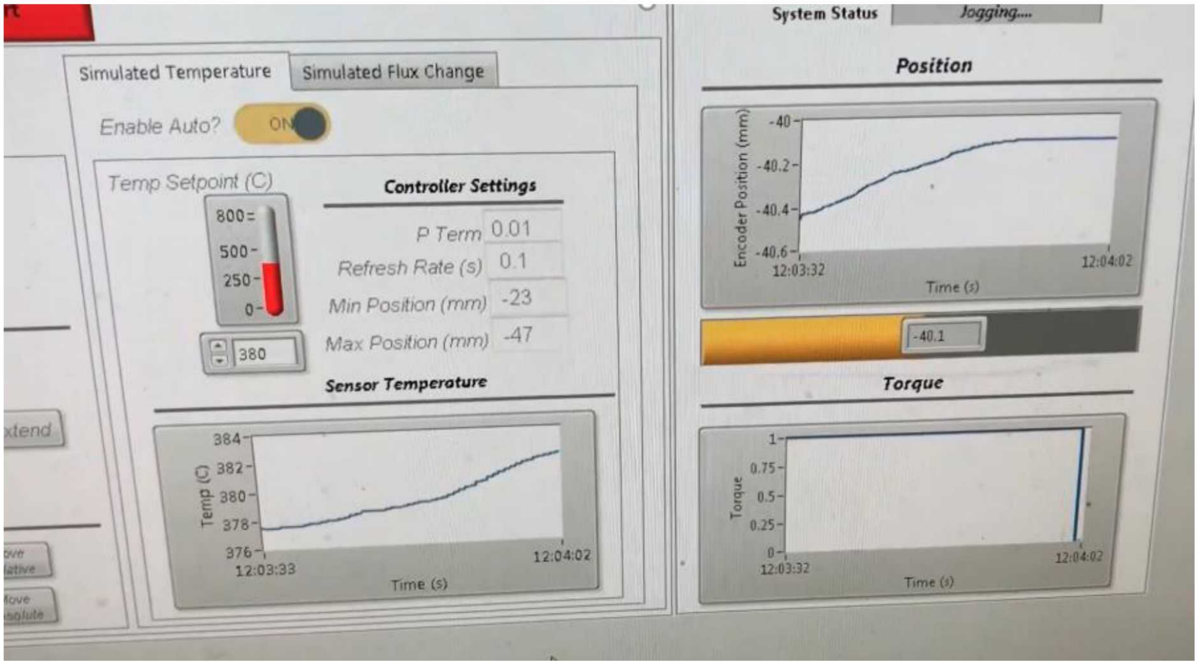

System Status: Jogging....

Enable Auto? ON

Temp Setpoint (C): 380

Controller Settings

P Term: 0.01

Refresh Rate (s): 0.1

Min Position (mm): -23

Max Position (mm): -47

Figure 62. Screen capture of the Labview control system and interface used during the automated particle mass-flow and temperature control tests.

Table 23 presents a summary of the on-sun tests and the ability to meet the performance evaluation criteria shown in Table 24. For most of the tests, the control system was able to maintain the particle outlet temperature to within ±25 °C and during steady-state conditions as indicated by a Student's t-test with a 95% confidence interval of two sample means. Figure 63 shows some example results during a test on February 8, 2018, that spans a large temperature range. At the lower temperatures, the automated control system maintains a tight tolerance on the prescribed particle outlet temperature. At higher temperatures and incident irradiances, the particle outlet temperature oscillates about the setpoint temperature. This can be remedied by implementing a proportional-integral-derivative (PID) control solution rather than the simple proportional control system implemented during these initial tests. Future work should design and test PID-based control methods to demonstrate the automated particle mass-flow and temperature control system under a variety of conditions (temperature, irradiance, mass flow rate). It should be noted that the control system is more responsive at higher irradiances due to the higher heating rates and sensitivity of the particle outlet temperature to mass flow rates when a larger irradiance is applied.

Table 23. Summary of on-sun tests with automated particle mass-flow control to obtain a desired particle outlet temperature.

Date	Prescribed Temperature Setpoint	Length of Time used for t-Test. (mm:ss)	Average Temp During Interval, °C	Number of Heliostats	($T_{outlet} - T_{setpoint}$) $< 25°C$?	Steady State Conditions have been met by t-test of 2 sample means?
12/19/2017	350	02:14.4	352.3	52	Yes	Yes
12/19/2017	375	00:33.6	376.2	46	Yes	Yes
12/19/2017	400	02:14.4	401.6	34	Yes	Yes
12/22/2017	480	02:14.4	479.7	16	Yes	Yes
2/8/2018	330	04:57.9	333.7	24	Yes	No
2/8/2018	340	02:14.4	342.0	24	Yes	No
2/8/2018	350	02:03.2	350.7	24	Yes	No
2/8/2018	360	02:25.6	361.2	22	Yes	Yes
2/8/2018	370	01:52.0	371.1	24	Yes	Yes
2/8/2018	380	03:44.0	379.6	22	Yes	Yes
2/8/2018	390	03:44.0	390.8	28	Yes	Yes
2/8/2018	450	00:33.6	452.5	52	Yes	Yes
2/8/2018	550	02:14.4	552.4	90	No	Yes
2/8/2018	600	01:40.8	616.8	89 to 79	No	No
2/8/2018	650	01:12.8	652.6	79	Yes	No

Table 24. Performance evaluation criteria for particle mass-flow and temperature control.

	Metric Definition (From Measurement)	*Success Value*	*Assessment Tool (Quality Assurance)*	*Goal Met (Y/N)*	*Supporting Data*

Project Evaluation Criteria 2.3.1	ΔT outlet: deviation in outlet temperature from set point Measured particle temperatures achieve steady state within 1 minute of a controlled transient event Note: Particle mass flow rate will be varied by control system to accommodate variations in DNI and other transients.	ΔT outlet < 25°C Sample means are the same for two different sets of data at different times to indicate steady-state conditions Constraint: evaluated at 2 or more unique particle inlet temperatures including 550°C each with 3 or more unique flux perturbation events	Regression fit of 2 minutes of data indicating steady state particle outlet temperature has been achieved And Range: maximum measured excursion no greater than success value at any point during steady state particle-outlet temperature	Y (majority of tests)	Figure 22

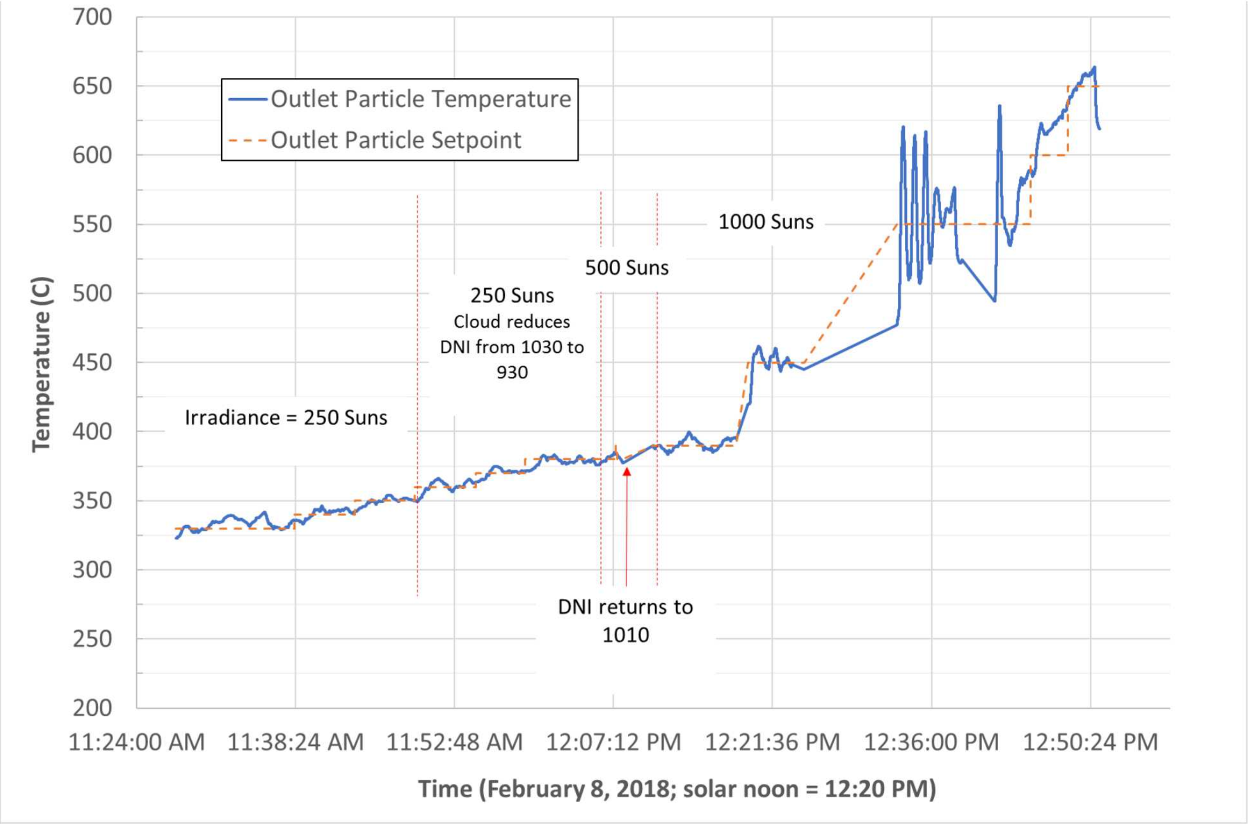

Figure 63. Results during automated particle mass-flow and temperature control on-sun testing.

5. CONCLUSIONS

This report presented studies to investigate particle mass flow control and release configurations through the receiver to enhance light trapping, increase thermal efficiencies, and accommodate transients in the solar irradiance and environmental conditions.

In the first year, novel particle release patterns were designed and tested to increase the effective solar absorptance of the particle curtain. Modeling results showed that increasing the magnitude and frequency of different wave-like patterns increased the effective absorptance and thermal efficiency by several percentage points, depending on the mass flow rate. Tests showed that triangular-wave, square-wave, and parallel-curtain particle release patterns could be implemented and maintained at flow rates of ~10 kg/s/m. At higher particle mass flow rates, the positive impact of non-planar (volumetric) particle release patterns was diminished. However, a 2 – 3% increase in thermal efficiency at desired operating temperatures between ~600 – 750 °C could still be achieved with non-planar particle release patterns.

The second year of the project focused on the development and testing of particle mass-flow control and measurement methods. An automated slide gate controlled by the outlet temperature of the particles was designed and tested. Testing demonstrated that the resolution accuracy of the slide-gate positioning was less than ~1 mm, and the speed of the slide gate enabled rapid adjustments to accommodate changes in the irradiance to maintain a desired outlet temperature range. At lower temperatures (<500 °C) and irradiances (~500 suns), the control system maintained good control of the particle outlet temperatures (within ±25 °C of the setpoint temperature). At higher temperature (>500 °C) and irradiances (~1000 suns), the control system showed more significant oscillations about the setpoint temperature due to the simple nature of the proportional control algorithm.

Different in-situ particle mass-flow measurement techniques were investigated, and two were tested. The in-situ microwave sensor was found to be unreliable and sensitive to variations in particle flow patterns. However, the in-situ weigh hopper using load cells was found to provide reliable and repeatable measurements of real-time in-situ particle mass flow.

On-sun tests were performed to determine the thermal efficiency of the receiver as a function of mass flow rate, particle temperature, and irradiance. Models of the tests were also developed and compared to the tests. The particle temperature rise was well correlated between experimental and simulated results, but external wind was found to impact the thermal efficiencies measured during the tests, leading to poor correlations between simulated and measured results. The measured data were used to derive an empirical correlation that could be used to predict the thermal efficiency as a function of particle mass flow rate, irradiance, particle temperature, and wind speed and direction. By setting the wind speed to zero in the empirical correlation, parity plots showed that the empirical correlation matched the CFD simulations, which did not include impacts of external wind.

Based on these findings, recommendations for future work include the following:

Particle Mass Flow Control and Measurement

- Develop PID methods for particle mass flow control to smooth out oscillations in particle outlet temperatures during large fluctuations in irradiance or wind

- Demonstrate high-temperature particle slide-gate operation for thousands of hours of operation to identify potential failure points and mitigation measures
- Implement weigh-hoppers (demonstrated in this work) to obtain accurate, real-time, in-situ measurements of particle mass flows
    - In between receiver and storage
    - In between heat exchanger and bottom storage bin

Thermal Efficiency

- Evaluate mitigation measures to reduce impacts of wind on convective and particle losses in a free-falling particle curtain
- Develop CFD models with the capability to simulate external wind from varying directions
    - Simulate the impacts of scale-up and larger receiver sizes on heat losses, particle losses, and thermal efficiency

REFERENCES

[1] Ho, C.K., 2016, A Review of High-Temperature Particle Receivers for Concentrating Solar Power, *Applied Thermal Engineering*, **109**(Part B), p. 958-969.

[2] Ho, C.K., United States Patent Provisional Application 62/145136, Falling Particle Solar Receivers, Sandia Corporation, April 9, 2015.

[3] Ho, C.K., J.M. Christian, J. Yellowhair, K. Armijo, and S. Jeter, 2016, *Performance Evaluation of a High-Temperature Falling Particle Receiver*, in *ASME Power & Energy Conference*, Charlotte, NC, June 26-30, 2016.

[4] Siegel, N., G. Kolb, K. Kim, V. Rangaswamy, and S. Moujaes, 2007, Solid particle receiver flow characterization studies, *Proceedings of the Energy Sustainability Conference 2007*, p. 877-883.

[5] Kim, K., N. Siegel, G. Kolb, V. Rangaswamy, and S.F. Moujaes, 2009, A study of solid particle flow characterization in solar particle receiver, *Solar Energy*, **83**(10), p. 1784-1793.

[6] Siegel, N.P., C.K. Ho, S.S. Khalsa, and G.J. Kolb, 2010, Development and Evaluation of a Prototype Solid Particle Receiver: On-Sun Testing and Model Validation, *Journal of Solar Energy Engineering-Transactions of the Asme*, **132**(2).

[7] Ho, C.K., J.M. Christian, J. Yellowhair, N. Siegel, S. Jeter, M. Golob, S.I. Abdel-Khalik, C. Nguyen, and H. Al-Ansary, 2016, On-Sun Testing of an Advanced Falling Particle Receiver System, *Solarpaces 2015: International Conference on Concentrating Solar Power and Chemical Energy Systems*, **1734**.

[8] Ho, C.K., J.M. Christian, D. Romano, J. Yellowhair, N. Siegel, L. Savoldi, and R. Zanino, 2017, Characterization of Particle Flow in a Free-Falling Solar Particle Receiver, *Journal of Solar Energy Engineering-Transactions of the Asme*, **139**(2).

[9] Ho, C.K., B. Mills, and J.M. Christian, 2016, *Volumetric Particle Receivers for Increased Light Trapping and Heating*, in *ASME Power & Energy Conference*, Charlotte, NC, June 26-30, 2016.

[10] Mills, B. and C.K. Ho, 2017, *Numerical Evaluation of Novel Particle Release Patterns in High-temperature Falling Particle Receivers*, in *ASME Power & Energy Conference*, Charlotte, NC, June 26-30, 2017.

[11] Mills, B., C.K. Ho, J.M. Christian, and G. Peacock, 2016, *Novel Particle Release Patterns for Increased Receiver Thermal Efficiency*, in *SolarPACES 2016*, Abu Dhabi, UAE,

[12] Ho, C.K., S.S. Khalsa, and N.P. Siegel, 2009, *Modeling on-Sun Tests of a Prototype Solid Particle Receiver for Concentrating Solar Power Processes and Storage*, in *ES2009: Proceedings of the ASME 3rd International Conference on Energy Sustainability, Vol 2*, San Francisco, CA,

[13] Christian, J.M. and C.K. Ho, 2013, *Alternative Designs of a High Efficiency, North-Facing, Solid Particle Receiver*, in *SolarPACES 2013*, Las Vegas, NV, September 17 - 20, 2013.

[14] Khalsa, S.S.S. and C.K. Ho, 2011, Radiation Boundary Conditions for Computational Fluid Dynamics Models of High-Temperature Cavity Receivers, *Journal of Solar Energy Engineering-Transactions of the Asme*, **133**(3).

[15] Ho, C.K. and J.M. Christian, 2013, *Evaluation of Air Recirculation for Falling Particle Receivers*, in *Proceedings of ASME 2013 7th International Conference on Energy Sustainability*, ES-FuelCell2013-18236, Minneapolis, MN, July 14 - 19, 2013.

[16] Ho, C.K., J.M. Christian, A.C. Moya, J. Taylor, D. Ray, and J. Kelton, 2014, *Experimental and Numerical Studies of Air Curtains for Falling Particle Receivers*, in *Proceedings of ASME 2014 8th International Conference on Energy Sustainability*, ES-FuelCell2014-6632, Minneapolis, MN, June 29 - July 2, 2014.

[17] Ho, C.K., J.M. Christian, D. Romano, J. Yellowhair, and N. Siegel, 2015, *Characterization of Particle Flow in a Free-Falling Solar Particle Receiver*, in *Proceedings of the ASME 2015 Power and Energy Conversion Conference*, PowerEnergy2015-49421, San Diego, CA, June 28 - July 2, 2015.

[18] Peacock, G., C.K. Ho, J.M. Christian, and D. Ray, 2017, *Automated Particle Mass-Flow Control System for High-Temperature Falling Particle Receivers*, in *SolarPACES 2017: International Conference on Concentrating Solar Power and Chemical Energy Systems*, 1734, Santiago, Chile, September 26 - 29, 2017.

[19] Albrecht, K.J. and C.K. Ho, 2017, *High-Temperature Flow Testing and Heat Transfer for a Moving Packed-Bed Particle/sCO2 Heat Exchanger*, in *SolarPACES 2017*, Santiago, Chile, September 26 - 29, 2017.

[20] Ho, C.K. and B.D. Iverson, 2014, Review of high-temperature central receiver designs for concentrating solar power, *Renewable & Sustainable Energy Reviews*, **29**, p. 835-846.

[21] Siegel, N.P., M.D. Gross, and R. Coury, 2015, The Development of Direct Absorption and Storage Media for Falling Particle Solar Central Receivers, *ASME J. Solar Energy Eng.*, **137**(4), p. 041003-041003-7.

[22] Ho, C.K., J.M. Christian, J. Yellowhair, S. Jeter, M. Golob, C. Nguyen, K. Repole, S.I. Abdel-Khalik, N. Siegel, H. Al-Ansary, A. El-Leathy, and B. Gobereit, 2017, *Highlights of the High-Temperature Falling Particle Receiver Project: 2012 - 2016*, in *SolarPaces 2016: International Conference on Concentrating Solar Power and Chemical Energy Systems*, Abu Dhabi, UAE, October 11 - 14, 2016.

APPENDIX A: DOE SOLAR ENERGY TECHNOLOGIES OFFICE PROJECT INFORMATION

Project Title: Particle Mass Flow Control and Measurement for High-Temperature Particle Receivers
(formerly “Fractal-Like Receiver Designs for High-Temperature High-Efficiency Operation”)

Project Period: 10/1/15 – 09/30/17 (no-cost time extension to 1/31/18)

Submission Date:

Budget Period: Phase 2: 10/01/16 – 1/31/18

Reporting Frequency: Quarterly

Submission Date: March 23, 2018

Recipient: Sandia National Laboratories

Address: P.O. Box 5800, MS-1127
Albuquerque, NM 87185-1127

Website: www.sandia.gov/csp

Award Number: SuNLaMP-0000000-1506 (CSP.Topic2.SNL.Ho)

Project Team: Sandia National Laboratories

Principal Investigator: Clifford K. Ho, Distinguished Member of the Technical Staff
Phone: (505) 844-2384
Email: ckho@sandia.gov

Business Contact: Scott Newberry
Phone: (505) 379-1341
Email: jnewber@sandia.gov

HQ Tech Manager: Matthew Bauer

HQ Project Officer: Christine Bing

APPENDIX B: TEST PLANS

Falling Particle Receiver Test Procedure for Efficiency Measurements

Cliff Ho, July 17, 2015
Modified: Greg Peacock, December 11, 2017

1. Initiate procedure for testing (e.g., apply power to field, wake up heliostats, 1 MW pump on, check SCRAM, etc.)
    - Confirm startup checklist is finished
2. Turn on particle elevator (40 Hz)
3. Turn on Bucket Elevator
4. Plug in Load Cells, SolidFlow Sensor, and Actuators within the PXIE housing
5. Turn on water to SolidFlow Sensor
    - Observe that water is flowing out of the SolidFlow's water discharge tube located on the east side of the test platform
6. See the "Falling Particle Program Initialization" procedure for information on how to access the control program
7. Home the slide gate by pressing the Home button
    - The system controls will be unresponsive for 20 seconds while the Labview program operates
8. Following the heliostat operation startup OP (black binder next to control computer), bring designated heliostats to face south, line bottom, and then standby position 20 m east of receiver ("20, 2.083, 68.81")
9. Ensure data is logging properly
    - Check data file to make sure file size is growing periodically throughout test and consider saving new data files after each major event (e.g., "FPR_15-07-16_1419.txt")
10. Set the slide gate to a desired aperture (currently, a slide-gate location of -15 mm corresponds to the onset of particle flow)
    - Observe that particle flow is fully developed across the entire width of the discharge chute
    - Close weigh hopper slide gate and then divert particles to the weigh hopper for 30 seconds (or an appropriate duration) to measure the mass flow rate
    - After 30 seconds, open the weigh hopper slide gate and divert particles back to the Olds elevator
    - Record particle mass flow rate, aperture setting, and particle inlet temperature
    - Repeat at several different aperture settings and flow rates (we also want to do this at different temperatures)
11. Bring beams onto flux target ("1.25, 2.083, 68.81")
    - Take PHLUX image and record Kendall reading, in addition to time, DNI, etc.
    - For 500 suns, filters 8A and 8B were required
    - At >500 suns, take the beam off the flux target as soon as possible; watch the Kendall outlet flow temperature (WCP-003)

12. Put beams in standby position and wait for particle outlet (thermocouple funnel) temperatures (BH-005 – BH-009) to “flatline”
13. Bring beams onto receiver (“-0.85, 2.083, 68.31”)
    - Take PHLUX image and record particle temperatures entering and leaving the receiver, in addition to time, DNI, etc.
    - Use no filters; the RSLE will be saturated, but the inside of the cavity will be okay
14. Wait for particle outlet (BH-005 – BH-009) temperatures to stabilize (5 - 10 minutes)
    - Periodically, close weigh hopper slide gate and then divert particles to the weigh hopper for 30 seconds (or an appropriate duration) to measure the mass flow rate
    - Record particle mass flow rate, aperture setting, and particle inlet temperature
    - After 30 seconds, open the weigh hopper slide gate and divert particles back to the Olds elevator
15. Bring beams onto flux target (“1.25, 2.083, 68.81”)
    - Take PHLUX image and record Kendall reading, in addition to time, DNI, etc.
    - For 500 suns, filters 8A and 8B were required
    - At >500 suns, take the beam off the flux target as soon as possible; watch the Kendall outlet flow temperature (WCP-003)
16. If <u>peak</u> particle outlet (funnel thermocouple) temperatures are less than ~750 – 800 °C, bring beam back onto receiver (“-0.85, 2.083, 68.31”)
    - Allow top hopper temperatures to increase to desired temperature for efficiency calculations (i.e.,, 300°C, 500°C)
        - TC-TH-16, 17, 49, 50, and 52 are located in the release slot
        - When max top hopper temperatures reach ~20 – 30 °C above desired temperature, **repeat steps 10 – 16**
17. When <u>peak</u> particle outlet (funnel thermocouple) temperatures reach ~750 – 800 °C, remove beams from system and allow to cool*
    - When receiver/particle temperatures are less than ~350°C, turn off particle elevator
        - Wait several minutes for particles to completely discharge from top hopper
        - Replace aperture cover with two people; raise scissor lift slowly and use aperture plate as heat shield
18. Shut down heliostat field and testing (turn 1 MW pump off)
    - Maintain water flow through the Solidflow sensor until it has cooled to ambient.
19. Blow out all the water lines to prevent freezing overnight.

*Alternatively, we can apply the minimum number of heliostats to maintain a constant particle inlet temperature while the system is flowing particles. The irradiance from these heliostats (as determined from the flux target) will be an estimation of the total heat loss from the system (receiver, hoppers, elevators, etc.) at a given temperature and particle mass flow rate. Together with the receiver efficiency calculations, which will provide the receiver heat loss as a function of irradiance and absorbed heat by the particles, we can estimate the heat loss from the rest of the infrastructure.

Falling Particle Receiver Test Procedure for Automatic Mass Flow Control

Cliff Ho, July 17, 2015
Modified: Greg Peacock, December 19, 2017

1. Initiate procedure for testing (e.g., apply power to field, wake up heliostats, 1 MW pump on, check SCRAM, etc.)
    - Confirm startup checklist is finished
2. Turn on particle elevator (40 Hz)
3. Turn on Bucket Elevator
4. Plug in Load Cells, SolidFlow Sensor, and Actuators within the PXIE housing
5. Turn on water to SolidFlow Sensor
    - Observe that water is flowing out of the SolidFlow's water discharge tube located on the east side of the test platform
6. See the "Falling Particle Program Initialization" procedure for information on how to access the control program
7. Home the slide gate by pressing the Home button
    - The system controls will be unresponsive for 20 seconds while the Labview program operates
8. Following the heliostat operation startup OP (black binder next to control computer), bring designated heliostats to face south, line bottom, and then standby position 20 m east of receiver ("20, 2.083, 68.81")
9. Ensure data is logging properly
    - Check data file to make sure file size is growing periodically throughout test and consider saving new data files after each major event (e.g., "FPR_15-07-16_1419.txt")
10. From the DAQ program, select TC-TH-16, 17, 49, 50, and 52 for monitoring
    - These TCs are located in the top hopper release slot and are the best indication of particle inlet temperature
11. From the DAQ program, select and add PXISlot5/a13-a17 for monitoring
    - Select 'Enable' for each TC to include it in the average particle outlet temperature
    - These TCs are located in the particle funnels at the bottom of the receiver and measure the particle outlet temperature
12. Set the diverter valve to circulate particles through the Olds Elevator
13. Enable automatic control from the LabVIEW Controller window and set the desired particle outlet temperature to $100°C$
    - The P-term is initially set at 0.01 $\frac{mm}{s*°C}$. Increasing this term will induce the slide gate to move faster at larger temperature errors.
    - When automatic control is enabled, the minimum slot aperture is 8 mm (~1 kg/s when cold), maximum slot aperture is 25 mm (~9.8 kg/s when cold)
    - Observe that particle flow is fully developed across the entire width of the discharge chute
14. Bring beams onto flux target ("1.25, 2.083, 68.81")
    - Record the number of heliostats applied
    - Take PHLUX image and record Kendall reading, in addition to time, DNI, etc.

    - For 500 suns, filters 8A and 8B were required
    - At >500 suns, take the beam off the flux target as soon as possible; watch the Kendall outlet flow temperature (WCP-003)

15. Wait for particle outlet (thermocouple funnel) temperatures (BH-005 – BH-009) to “flatline”
    - Close weigh hopper slide gate and then divert particles to the weigh hopper for 30 seconds (or an appropriate duration) to measure the mass flow rate
    - Record particle mass flow rate, aperture setting, and particle inlet temperature
    - After 30 seconds, open the weigh hopper slide gate and divert particles back to the Olds elevator
16. Remove a pre-determined number of heliostats from the particle curtain
17. Wait for particle outlet (thermocouple funnel) temperatures (BH-005 – BH-009) to “flatline”
    - Close weigh hopper slide gate and then divert particles to the weigh hopper for 30 seconds (or an appropriate duration) to measure the mass flow rate
    - Record particle mass flow rate, aperture setting, and particle inlet temperature
    - After 30 seconds, open the weigh hopper slide gate and divert particles back to the Olds elevator
18. Put the original number of heliostats from step 14 back onto the curtain
19. Wait for particle outlet (thermocouple funnel) temperatures (BH-005 – BH-009) to “flatline”
    - Close weigh hopper slide gate and then divert particles to the weigh hopper for 30 seconds (or an appropriate duration) to measure the mass flow rate
    - Record particle mass flow rate, aperture setting, and particle inlet temperature
    - After 30 seconds, open the weigh hopper slide gate and divert particles back to the Olds elevator
20. Add a predetermined number of heliostats to the particle curtain
21. Wait for particle outlet (thermocouple funnel) temperatures (BH-005 – BH-009) to “flatline”
    - Close weigh hopper slide gate and then divert particles to the weigh hopper for 30 seconds (or an appropriate duration) to measure the mass flow rate
    - Record particle mass flow rate, aperture setting, and particle inlet temperature
    - After 30 seconds, open the weigh hopper slide gate and divert particles back to the Olds elevator
22. Remove the added heliostats so that the original number of heliostats from step 14 are on the curtain
23. Wait for particle outlet (thermocouple funnel) temperatures (BH-005 – BH-009) to “flatline”
    - Close weigh hopper slide gate and then divert particles to the weigh hopper for 30 seconds (or an appropriate duration) to measure the mass flow rate
    - Record particle mass flow rate, aperture setting, and particle inlet temperature
    - After 30 seconds, open the weigh hopper slide gate and divert particles back to the Olds elevator
24. Repeat **steps 13 through 23** for $300°C$ and $550°C$ particle outlet temperatures
25. When <u>peak</u> particle outlet (funnel thermocouple) temperatures reach ~750 – 800 °C, remove beams from system and allow to cool*
    - When receiver/particle temperatures are less than ~350°C, turn off particle elevator
        - Wait several minutes for particles to completely discharge from top hopper
        - Replace aperture cover with two people; raise scissor lift slowly and use aperture plate as heat shield

26. Shut down heliostat field and testing (turn 1 MW pump off)
    - Maintain water flow through the Solidflow sensor until it has cooled to ambient.
27. Blow out all the water lines to prevent freezing overnight.

DISTRIBUTION

All Electronic

1	Clifford Ho, 8823	ckho@sandia.gov
1	Joshua Christian, 8823	jmchris@sandia.gov
1	Julius Yellowhair, 8823	jeyello@sandia.gov
1	Kevin Albrecht, 8823	kalbrec@sandia.gov
1	Daniel Ray, 8823	dray@sandia.gov
1	Paul Gauche, 8823	pgauche@sandia.gov
1	Brantley Mills, 1514	bramill@sandia.gov
1	Greg Peacock, 2547	gpeacoc@sandia.gov

1	Matthew Bauer, DOE	matthew.bauer@ee.doe.gov
1	Vijay Rajgopal, DOE	Rajgopal.Vijaykumar@EE.Doe.Gov
1	Christine Bing, DOE	Christine.Bing@ee.doe.gov
1	CSP Solar	cspsolar@ee.doe.gov

1	Technical Library, 9536	sanddocs@sandia.gov

Sandia National Laboratories